Dissertations   Theses and Dissertations

Spring 2018

Numerical simulations of thin viscoelastic films

Valeria Barra
New Jersey Institute of Technology

ABSTRACT

NUMERICAL SIMULATIONS OF THIN VISCOELASTIC FILMS

by
Valeria Barra

This dissertation is developed in the field of Computational Fluid Dynamics (CFD) and it focuses on numerical simulations of the dynamics of thin viscoelastic films in different settings. The first part of this dissertation presents a novel computational investigation of thin viscoelastic films and drops, that are subject to the van der Waals interaction force, in two spatial dimensions. The liquid films are deposited on a flat solid substrate, that can have a zero or nonzero inclination with respect to the base. The equation that governs the interfacial dynamics of the thin films and drops is obtained within the long-wave approximation of the Navier-Stokes equations, with the Jeffreys model for viscoelastic stresses. The effects of viscoelasticity and the substrate slippage on the dynamics of thin viscoelastic films are investigated. Moreover, the effects of viscoelasticity on drops that spread or recede on a prewetted flat substrate are analyzed. For dewetting films, the numerical results show the presence of multiple secondary droplets for higher values of the relaxation time, consistently with experimental findings. These secondary length scales are found to be suppressed by gravitational effects when the case of dewetting films on inverted planes is analyzed. For spreading and receding drops on flat, prewetted substrates, viscoelastic effects are found to lead to deviations from the Cox-Voinov law for partially wetting fluids. In general, viscoelasticity enhances the spreading and suppresses the retraction of viscoelastic drops, compared to Newtonian ones.

The second part of this dissertation presents a novel numerical investigation of the dynamics of free-boundary flows of viscoelastic liquid membranes, not necessarily deposited on solid substrates. The governing equation describes the balance of linear momentum, in which the stresses include the viscoelastic response to deformations of

Maxwell type. A penalty method is utilized to enforce near incompressibility of the viscoelastic media, in which the penalty constant is proportional to the viscosity of the fluid. A finite element method is used, in which the slender geometry representing the liquid membrane is discretized by linear three-node triangular elements under plane stress conditions. Two applications of interest are considered for the numerical framework provided: shear flow, and extensional flow in drawing processes. Finally, the last part of this dissertation considers the expansion of the study of the dynamics of viscoelastic membranes by applying the general theory of shells, in which any application of loading or external forces causes both bending and stretching, so that buckling or wrinkling phenomena can be investigated as future work.

NUMERICAL SIMULATIONS OF THIN VISCOELASTIC FILMS

by
Valeria Barra

A Dissertation
Submitted to the Faculty of
New Jersey Institute of Technology
and Rutgers, The State University of New Jersey–Newark
in Partial Fulfillment of the Requirements for the Degree of
Doctor of Philosophy in Mathematical Sciences

Department of Mathematical Sciences, NJIT
Department of Mathematics and Computer Science, Rutgers–Newark

May 2018

NUMERICAL SIMULATIONS OF THIN VISCOELASTIC FILMS

Valeria Barra

Dr. Shahriar Afkhami, Dissertation Co-Advisor   Date
Associate Professor of Mathematical Sciences, New Jersey Institute of Technology

Dr. Lou Kondic, Dissertation Co-Advisor   Date
Professor of Mathematical Sciences, New Jersey Institute of Technology

Dr. Shawn A. Chester, Dissertation Co-Advisor   Date
Assistant Professor of Mechanical Engineering, New Jersey Institute of Technology

Dr. Denis L. Blackmore, Committee Member   Date
Professor of Mathematical Sciences, New Jersey Institute of Technology

Dr. Christopher Batty, Committee Member   Date
Assistant Professor of Computer Science, University of Waterloo

BIOGRAPHICAL SKETCH

Author: Valeria Barra

Degree: Doctor of Philosophy

Date: May 2018

Undergraduate and Graduate Education:

- Doctor of Philosophy in Mathematical Sciences,
  New Jersey Institute of Technology, Newark, NJ, USA, 2018

- Master of Science in Mathematical Sciences,
  University of Siena, Siena, Italy, 2011

- Bachelor of Science in Mathematical Sciences,
  University of Siena, Siena, Italy, 2008

Major: Applied Mathematics

Publications:

V. Barra, S. Afkhami, and L. Kondic, Thin viscoelastic dewetting films of Jeffreys
     type subject to gravity and substrate interactions, submitted to *The European
     Physical Journal E*, (2018).

V. Barra, S. A. Chester, and S. Afkhami, Numerical simulations of nearly incompress-
     ible viscoelastic membranes, in revision for *Computers and Fluids*, (2018).

V. Barra, S. Afkhami, and L. Kondic, Interfacial dynamics of thin viscoelastic films
     and drops, *Journal of Non-Newtonian Fluid Mechanics*, 237:26-38 (2016).

Presentations:

Numerical simulations of thin viscoelastic films. *American Mathematical Society Joint
     Mathematics Meeting*, San Diego, CA, January 12, 2018.

Simulations of viscous fluids on curved surfaces. *Fluid Mechanics and Waves Seminar*,
     New Jersey Institute of Technology, Newark, NJ, January 30, 2017.

Simulations of fluids on surfaces. *Research Seminar*, Pixar Animation Studios,
     Emeryville, CA, December 13, 2017.

Wetting and dewetting of thin viscoelastic drops. *Society for Industrial and Applied Mathematics Annual Meeting*, Boston, MA, July 15, 2016.

Interfacial dynamics of thin viscoelastic films and drops. *The Dana Knox Research Showcase*, New Jersey Institute of Technology, Newark, NJ, April 20, 2016.

Interfacial dynamics of thin viscoelastic films and drops. *The Fifth Annual Northeast Complex Fluids and Soft Matter Workshop*, New York University Tandon School of Engineering, New York, NY, January 15, 2016.

Analysis and simulations for interfacial instability of thin viscoelastic liquid films. *The Third Annual Northeast Complex Fluids and Soft Matter Workshop*, New Jersey Institute of Technology, Newark, NJ, January 16, 2015.

Posters:

Gravity-driven instabilities of thin viscoelastic films on an inverted plane. *Frontiers in Applied and Computational Mathematics*, New Jersey Institute of Technology, Newark, NJ, June 24-25, 2017.

Surface instabilities and droplets formation in thin viscoelastic films. *Graduate Student Research Day*, New Jersey Institute of Technology, Newark, NJ, October 28, 2015.

Numerical study of thin layers of viscoelastic fluids. *Scientista Symposium*, Microsoft, New York, NY, October 16-18, 2015.

Numerical study of thin viscoelastic films on substrates. *Frontiers in Applied and Computational Mathematics*, New Jersey Institute of Technology, Newark, NJ, June 5-6, 2015.

Numerical study of thin viscoelastic films on substrates. *Society for Industrial and Applied Mathematics Conference on Computational Science and Engineering*, Salt Lake City, UT, March 14-18, 2015.

Interfacial instability of thin viscoelastic liquid films. *Graduate Student Research Day*, New Jersey Institute of Technology, Newark, NJ, October 30, 2014.

Linear stability analysis of thin viscoelastic liquid of Jeffreys type with van der Waals interaction. *Frontiers in Applied and Computational Mathematics*, New Jersey Institute of Technology, Newark, NJ, May 22-23, 2014.

To my husband, Matteo,
always with me,
even when an ocean was between us

ACKNOWLEDGMENT

First and foremost, I would like to thank my advisor, Prof. Shahriar Afkhami, and my co-advisors, Prof. Lou Kondic and Prof. Shawn Chetser, for their valuable guidance and support. I am especially thankful to them because they have helped me develop critical thinking and rigor in the scientific method, by asking the types of questions that a young researcher should learn to raise autonomously. In particular, I would like to thank Prof. Afkhami for introducing me to the challenging world of CFD and for being supportive in my pursuit of an internship at Pixar Animation Studios, Prof. Kondic for his expert guidance and advice, and Prof. Chester for his amazing help and support. I would also like to thank my committee members: Prof. Denis Blackmore for his endless wisdom tips, and Prof. Christopher Batty, for his kind availability in sharing his work with us.

I would like to thank the Department of Mathematical Sciences of NJIT, whose people have always been very understanding towards the needs of its graduate students. In particular, I would like to thank the Chairperson of the Department, Prof. Jonathan Luke, for providing career advice and support, and all of the administrative staff members, who, during the years, have done an amazing work and become more than friendly faces in the office. I would also like to mention some of the Professors that I met at NJIT during my journey as a graduate student and have made an enormous impact on me: Prof. Victor Matveev, Prof. Richard Moore, and Prof. Linda Cummings. I would also like to acknowledge partial support by the NSF grants No. DMS-1320037, CBET-1604351, and CBET-1235710.

There are many people without whom I could have not done all of this. The most indispensable one, the one that has always provided his constant moral and technical support, ever since my undergraduate studies, is my beloved husband, Matteo Vigni. Without his infinite patience I could have not endured the four and a half years of

LIST OF FIGURES

Figure   **Page**

LIST OF SYMBOLS

$\mathbf{A}$	matrix or vector
a_{ij}	matrix in tensor form
$tr(\mathbf{A}) = a_{ii}$	trace of a matrix a_{ij} in indicial (or summation) convention
$\mathbf{u}$	vector displacement field
$\dot{\mathbf{u}} = \mathbf{v}$	vector velocity field
$\ddot{\mathbf{u}} = \mathbf{a}$	vector acceleration field
$\boldsymbol{\epsilon}$	(infinitesimal) strain tensor
$\dot{\boldsymbol{\epsilon}}$	(infinitesimal) strain rate tensor
$\boldsymbol{\sigma}$	Cauchy stress tensor
λ_1	relaxation time
λ_2	retardation time
η	dynamic (shear) viscosity coefficient
γ	surface tension coefficient

CHAPTER 1

INTRODUCTION

Thin liquid films play a central role in many real life applications and therefore are widely studied theoretically, numerically, and experimentally. The interface between the liquid and the surrounding fluid (usually a gaseous phase) is a free and deformable boundary, and therefore thin liquid films can display a variety of dynamics and interfacial instabilities. As broadly presented in the literature, (see, for instance, [1, 2, 3]), instability can lead to the film breakup, so that the liquid separates in drops, exposing or *dewetting* the substrate. On the contrary, stability occurs when a thin film, whose interface is perturbed, returns to its initial configuration. In this dissertation, we are interested in numerically investigating the dynamics and the interface instabilities of thin layers of fluids that can arise in different settings and therefore can be described by different physical and computational models.

Multi-phase flows describe some of the most common forms of gas/liquid or solid/liquid interactions that we can observe in Nature and recreate in industrial processes. Perhaps the simplest natural examples of such interactions are provided by rain, bubbles, and water splashes; while for applications of industrial relevance, one can be interested in the study and control of droplets bursting in fuel combustion, and wetting or dewetting phenomena in painting, coating or printing processes. Due to this large applicability, free-boundary or interfacial flows have been intensively studied (see, for instance, the reviews [4, 5]). To capture the interface instabilities, the position of the interface, or boundary between the different phases, needs to be modeled and found as a part of the solution of the equations governing the fluid flow [6]. The goal of this dissertation is to provide a novel numerical investigation of the free-boundary flows of thin layers of fluids, in the particular case in which the liquid of interest is a viscoelastic fluid.

1.1 Linear Viscoelasticity

Among the broad spectrum of natural or synthetic thin layers of liquids, viscoelastic films are ubiquitous; in fact, they can be found in a large variety of settings, from typical life situations to sophisticated manufacturing processes. In our everyday life, we may encounter sheets or thin layers of liquids that show a viscoelastic behavior, such as custard, shampoo, shaving cream, wax, glue, and paint; or similarly, soft solids with the same characteristics, such as gels.

Viscoelastic materials exhibit features that are typical of both fluids (viscosity) and solids (elasticity). This hybrid nature allows them to characterize a broad variety of materials, with limiting cases that fall under a liquid state, or a solid state, and intermediate regimes that constitute soft materials, such as gels [7]. The evolution of their complex internal microstructures can affect their dynamics and the overall macroscopic rheology [8]. Polymeric liquids, in particular, are one example of a wider class of viscoelastic liquids, constituted by a Newtonian (viscous) solvent and a non-Newtonian (polymeric) solute, and, as other suspensions or emulsions, are considered one type of complex fluids. Viscoelastic liquids are, in turn, part of the wider class of non-Newtonian fluids, that show, in general, a variety of different behaviors. They are characterized by the fact that the stress tensor is not related via a simple linear relationship to the strain rate. In fact, the relationship between these two quantities can be nonlinear or differential.

The Maxwell model [9], and its extension, the Jeffreys model [10], considered in this dissertation, belong to a class of linear differential models for viscoelastic fluids and describe mechanical properties such as "fading memory" and stress relaxation [11]. These features become remarkable, especially when compared to constitutive models that describe a linear relationship between the stress and the strain (for linear elastic solids) or strain rate (for Newtonian fluids). The Maxwell constitutive model, in the same fashion as Hooke's law, was proposed empirically [9]. Although it has

been applied to and proven to be useful for the analysis of a broad range of materials, this model is limited to cases in which the deformation gradients are infinitesimally small [11]. To overcome this limitation, variations of the Maxwell model have been proposed, such as the Oldroyd-B model [11], in which convective derivatives are introduced to describe nonlinearities in the stress tensor. Despite the limitations of a linear viscoelastic model, such as the Maxwell or the Jeffreys model, we believe that a comprehensive analysis as well as a detailed numerical framework for the dynamics of thin viscoelastic films, can serve as a benchmark for future analyses that include nonlinear features, such as the convective/corotational variations of the stress.

1.2 Wetting and Dewetting Processes in the Lubrication Theory

In the first half of this dissertation (involving Chapters 2 and 3), we present a detailed description of the numerical solutions of the nonlinear governing equation based on the long-wave (lubrication) model for incompressible, thin viscoelastic films deposited on a flat substrate, with the Jeffreys constitutive model for viscoelastic stresses [10, 11]. Historically, the foundations of the long-wave theory have been laid in a pioneering work by Reynolds [12], that analyzes the behavior of a viscous liquid confined between a solid substrate and a fluid-lubricated slipper bearing [1]. The key point of this theory is to utilize the nondimensionalization and asymptotic expansion techniques to reduce the Navier-Stokes equations to one sole partial differential equation (PDE), governing the evolution of the interface of the fluid, characterized by small interfacial slopes, to satisfy the asymptotic assumptions. For the case in which the gravitational body force is neglected, the long-wave formulation for thin viscoelastic films of Jeffreys type considered in this work was developed by Rauscher et al. [13], and solved numerically in Chapter 2. By contrast, in Chapter 3, we present a novel derivation of the equation governing the dynamics of thin viscoelastic films of Jeffreys type flowing down an inclined plane, for which gravitational effects are taken into consideration.

The understanding of the instability mechanisms relevant to thin polymeric films, in particular, has motivated many theoretical and experimental studies, see, e.g., [11, 14, 15, 16]. Perhaps one of the first experimental works on this matter has been carried out by Reiter [17]. In that investigation, Reiter examines the influence of the film thickness on the interfacial instability of polymer films of nanometer size. We refer to the rupture of a thin liquid film deposited on a substrate, and the consequent formation of a hole in the interface of the fluid that exposes the substrate, leading to separate drops of liquid, as *dewetting* process. Contrastingly, the spreading of a thin layer of fluid on a surface is called *wetting* process. Reiter's study [17] shows that, when dewetting occurs, a rim can form ahead of the dewetting edge and subsequently decay into drops on the substrate. Since his work, the investigation of thin polymer film morphologies at the nanoscale has been a major focus of many studies, see, e.g., [18, 19, 20, 21, 22, 23]. Additional works focus on the stability, the dynamics, and the morphology of the fluid interface due to rheological properties [24, 25, 26, 27, 28, 29]; these investigations are carried out with the goal of understanding whether the effects related to viscoelasticity, slippage, surface heterogeneities, or forces of electrohydrodynamic origin play a key role in the development of surface instabilities.

To model the film breakup and the consequent dewetting process, as well as to impose the contact angle with the solid substrate, we include the van der Waals attraction/repulsion interaction force. This force introduces an equilibrium film on the solid substrate, leading to a prewetted (often called precursor) layer in nominally dry regions. We notice that in the absence of other forces, such as the gravitational force, the van der Waals attraction force is the only driving mechanism of interfacial instabilities. The dynamics of dewetting processes can be divided in two regimes: the initial stage of the evolution, characterized by amplitudes in the interface function that are small relative to the initial height of the film and whose growth is analytically predicted by a linear asymptotic analysis, called linear stability analysis (LSA); and

the development phase of the interface evolution, characterized by amplitudes that are no longer small and therefore cannot be described in terms of linear asymptotic approximations but require a fully nonlinear dynamic description. In Chapter 2, in particular, we focus on the emerging length scales due to the instability of a viscoelastic film in the nonlinear stage, that, prior to our study [30], had not been reported in the literature.

In addition the few numerical studies available in the literature that use the Jeffreys model for the viscoelastic stresses, [31, 32], we introduce a novel investigation of the effect of transitioning from no-slip to weak slip on the initial instability development and the dewetting dynamics. A surprising finding is that the resulting morphologies are influenced by viscoelasticity and slippage. In fact, we show the formation of not only main drops, as previously demonstrated in [32], but also of multiple satellite droplets that are completely absent for Newtonian films. These secondary droplets are comparable with those found experimentally (see, e.g., [17, 21] or [19], where they are called "nanodroplets"), but, to the best of our knowledge, had not been found in previous computational studies of the evolution of viscoelastic films, prior to our study [30].

It is appropriate to make a remark about the choice of the constitutive model. Although linear viscoelastic models, such as the Jeffreys model, are known to be valid only for flows with small displacement gradients [11, 13, 32], we expect a linear constitutive model to be adequate to describe the viscoelastic behavior in the context of spontaneous wetting/dewetting processes. For more complex flows, one should incorporate more general viscoelastic models, such as the Oldroyd-B model [11]. However, as noted also by Tomar et al. [32], the nonlinear convective terms of the stress tensor in an Oldroyd-B model would not change the linear stability analysis, and therefore our results for the linear regime are valid for both linear and nonlinear viscoelastic models. Furthermore, our numerical simulations show how, in

the final stage of the nonlinear evolution, dewetting viscoelastic films display a slow, viscous dynamics, for which a linear viscoelastic model is considered to be appropriate. Additionally, we have verified that displacement gradients (hence, the shear rate) are not large even in the intermediate time of the dewetting process, in which viscoelastic fluids exhibit a non-Newtonian response to deformations. In summary, in the context of spontaneous wetting/dewetting processes driven by the van der Waals interaction or the gravitational force, the assumption of small displacement gradients is not violated, and a linear viscoelastic model suffices to describe the effects of viscoelasticity.

1.3   Free-boundary Flows of Membranes and Shells

In the second half of this dissertation (involving Chapters 4 and 5), we aim to simulate the dynamics of sheets of viscoelastic fluids, not necessarily deposited on a substrate, in three spatial dimensions. For biomedical engineering applications, thin viscoelastic sheets can represent biopolymers [33], or biological tissues constituting blood cells [34, 35]. In some manufacturing processes, thin layers of elastic or viscoelastic materials, for instance, in the form of liquid crystal polymers, are largely employed [36]. Hence, the prediction of the behavior of viscoelastic sheets through mathematical and numerical modeling becomes a cost-effective manufacturing practice, as well as an important tool to better understand some physical effects, that are difficult or too expensive to reproduce experimentally. The mathematical and numerical framework developed in Chapter 4 aims at providing insight to the understanding of the dynamics and physical behavior of thin layers of viscoelastic media, modeled as membranes, and in Chapter 5, modeled as sheets.

Thin, curved bodies are commonly modeled as shells or membranes [37, 38]. The slender geometry of thin films or sheets of various materials can be described through an idealized mid-surface, that sits at half thickness between the top and bottom surfaces of the sheet. For the general theory of shells, the mid-surface has a non zero

curvature, and any application of loading or external forces causes both bending and stretching [39, 40]. A particular case of this general theory is the membrane theory of shells, that concerns the study of the in-plane stretching deformations, dominant with respect to transversal deflections, and in which bending stiffness is neglected. In Chapter 4, we utilize the membrane theory of shells, in which the in-plane stresses are included to model the viscoelastic response to deformations, and, in Chapter 5, we refer to the theory of shells to include bending effects.

1.4   Summary and Overview

The remainder of this dissertation is organized as follows: in Chapter 2, we present our numerical investigation of the dynamics of dewetting and wetting thin viscoelastic films and drops on a flat, solid substrate, in the absence of gravitational effects. In Section 2.2, we introduce the governing equations and the linear viscoelastic constitutive models. In Section 2.3, we outline the nondimensional analysis and long-wave (lubrication) approximation of the governing equations. In Section 2.4, we outline the numerical methods used to solve the equation governing the dynamics of the interface. In Section 2.5, we present the linear stability analysis, and discuss the numerical results for both dewetting and wetting studies; In Section 2.6, we draw our conclusions for Chapter 2.

In Chapter 3, we expand the investigation carried out in Chapter 2, to include gravitational effects. In Section 3.2, we give a brief description of the governing equations, and in Section 3.3, we derive the corresponding long-wave approximation. In Section 3.4, we summarize the numerical discretization of the governing equation. In Section 3.5, we present the LSA and the numerical results of dewetting viscoelastic films on inverted planes. In Section 3.6, we summarize our conclusions for Chapter 3.

In Chapter 4, we present our numerical investigation of the dynamics of viscoelastic membranes. In Section 4.2, we outline the mathematical formulation

and the finite element analysis of the governing equation (whose detailed derivation is given in Appendix A), and, in Section 4.3, we describe the constitutive model considered. In Section 4.4, we discuss our numerical results, and in Section 4.5, we draw our conclusions for Chapter 4.

In Chapter 5, we propose an expansion of the analysis presented in Chapter 4, by considering the dynamics of thin viscoelastic shells. In Section 5.2, we provide the mathematical formulation of the general theory of shells, and in Section 5.3, the equations governing the dynamics of viscous sheets, whose detailed description is outlined in Appendix B. In Section 5.4, we describe the constitutive law of linear elasticity and introduce the Stokes-Rayleigh analogy, and in Section 5.5, we show how this can be applied to study the behavior of elastic shells (and, analogously, viscous shells) undergoing stretching or bending deformations. The finite element numerical discretization of the terms introduced in this section is given in Appendix C. In Section 5.6, we extend the Stokes-Rayleigh analogy to the case of linear differential viscoelastic models. In Section 5.7, we provide two examples of applications of the framework provided, and in Section 5.8, we draw our conclusions for this study.

Finally, in Chapter 6, we summarize our overall conclusions of the work presented in this dissertation, and outline the possible future research directions.

CHAPTER 2

THIN VISCOELASTIC FILMS ON SOLID SUBSTRATES

2.1 Introduction

Despite the numerous works focusing on polymeric films mentioned in the Introduction, very few studies consider numerical simulations of the interface of thin layers of viscoelastic fluids dewetting a solid substrate, see, e.g., [31, 32]. In particular, Vilmin and Raphaël develop a model based on a simplified dewetting geometry of the film, neglecting the surface tension [31]. They demonstrate that the friction force and the residual stresses, due to the film viscoelasticity, can have an opposing influence on the dewetting dynamics. They show that these residual stresses can accelerate the onset of the dewetting, followed by a slow, quasi-exponential, growth of the hole. Although their model is useful to explain the main features of the dynamics of the evolving rim, it is unable to provide a detailed description of the dewetting process and a quantitative investigation of the final morphological structures. An earlier study of Tomar et al. [32] uses the lubrication model derived by Rauscher et al. [13] for thin viscoelastic films of Jeffreys type, although without including the substrate slippage. Using both linear stability analysis and nonlinear simulations, they show that viscoelasticity does not have a major influence on the dewetting dynamics. Their numerical solutions suggest that the length scale of instability in the nonlinear regime is unaltered by the viscoelasticity.

In this chapter, we present a detailed description of numerical solutions of the nonlinear governing equation based on the long-wave (lubrication) model developed by Rauscher et al. [13] for thin viscoelastic films, with the Jeffreys constitutive model for viscoelastic stresses [11, 10]. In this model, viscoelastic stresses are described with a Newtonian contribution (due to the solvent) plus a polymer contribution that is governed by the linear Maxwell model [15].

The first part of our investigations concerns the spontaneous dewetting of a thin viscoelastic film, initially at rest, due to van der Waals interactions, in two spatial dimensions. Consistent with [41], we find that, in the linear regime, the critical and most unstable wavenumbers are neither dependent on the viscoelastic parameters, nor on the slip length, but only on the van der Waals interactions with the substrate. We then provide numerical simulations of the evolution of the interface in the nonlinear regime. In this regime, we find that the instability and the final configuration of the fluid in primary and secondary droplets are affected by the viscoelastic parameters and the slippage of the substrate. We show how viscoelasticity induces the formation of secondary droplets, and how the slip at the substrate prevents them from forming. We thus provide, for the first time, numerical simulations leading to novel morphologies for thin viscoelastic dewetting films.

Finally, we focus on the spreading/receding of viscoelastic planar drops on a solid substrate. We study viscoelastic drops that spread/recede spontaneously due to the imbalance between the initial and the equilibrium contact angles. The theoretical and experimental studies of spreading or retracting drops, both for Newtonian and viscoelastic fluids, are numerous (see, e.g., [4, 42, 43, 44, 45, 46, 47, 48]). Surprisingly, only a few studies report computational results for viscoelastic dynamic contact lines, see [49, 50, 51]. Yue and Feng [49] use a phase-field model to simulate the displacement flow of Oldroyd-B fluids in a channel formed by parallel plates. They show that viscoelastic stresses close to the contact line region affect the bending of the interface. Also, Wang et al. [50] use an axisymmetric formulation to describe the spreading of viscoelastic drops, comparing the Giesekus (shear-thinning) and the Oldroyd-B models. They show that the spreading speed depends on the viscoelastic relaxation time. Most recently, Izbassarov and Muradoglu [51] study the effects of viscoelasticity on drop impact and spreading on a solid substrate. They investigate

the spreading rate of viscoelastic drops, using the FENE-CR model, and find that viscoelastic effects enhance the spreading speed.

We consider partial wetting by accounting for van der Waals interactions between the solid and the fluid. Although our approach is developed strictly for configurations characterized by small interfacial slopes, we expect that it still provides reasonably accurate results for the situations such that the contact angle is not small (see, e.g., [43] for a discussion of this topic). Our numerical results show that viscoelasticity enhances the spreading in the early stage of wetting by smoothing the interface in the contact line region. Similar considerations are drawn by Wang et al. [50], and Izbassarov and Muradoglu [51]. Finally, the study of the advancing dynamic contact angle allows us to determine that the Cox-Voinov law [52, 53] holds for the viscous Newtonian fluid, but not for the viscoelastic counterpart. For retracting drops, we find that the interface of a viscoelastic drop provides more resistance to the motion, causing the drop to retract slower, consistent with the experimental study [48]. Our results regarding receding viscoelastic drops show a deviation from the Cox-Voinov law as well.

2.2   Mathematical Formulation

In this section, we introduce the mathematical model used to describe thin viscoelastic films flowing on solid substrates, in two spatial dimensions. We consider an incompressible liquid, with constant density ρ, surrounded by a gas phase assumed to be inviscid, dynamically passive, and of constant pressure. The equations of conservation of momentum and mass, respectively, for the liquid phase are

$$\rho \left(\partial_t \mathbf{v} + \mathbf{v} \cdot \nabla \mathbf{v} \right) = -\nabla (p + \Pi) + \nabla \cdot \boldsymbol{\sigma} + \mathbf{F_b} \,, \tag{2.1a}$$

$$\nabla \cdot \mathbf{v} = 0 \,, \tag{2.1b}$$

where $\mathbf{v} = (v_1(x, y, t), v_2(x, y, t))$ is the velocity field in the Cartesian xy-plane (as by convention, the x-axis is horizontal, and the y-axis is vertical), and $\nabla = (\partial_x, \partial_y)$; $\boldsymbol{\sigma}$ is the stress tensor, p is the pressure, and Π is the disjoining pressure induced by the van der Waals solid-liquid interaction force (we note that $\nabla\Pi = 0$ except at the liquid-gas interface). This force is attractive (destabilizing) for thicker films and repulsive (stabilizing) for thin ones, leading naturally to the concept of equilibrium film thickness, defined below as $h_\star$, at which repulsive and attractive forces balance each other [54]. The form of the disjoining pressure used in the present work is given in the following section, where the thin film approximation of the system (2.1) is described in detail. The body force field in equation (2.1a) is given by $\mathbf{F_b} = (\rho g \sin\alpha, -\rho g \cos\alpha)$, where g is the gravitational acceleration constant, and α the angle that the inclined plane forms with respect to the positive x-axis. We consider $g = 0$ in this chapter, and $g > 0$ in the following one.

To model the stresses, we use a generalization of the Maxwell model for viscoelastic liquids: the Jeffreys model. The Jeffreys model, together with the Maxwell model, belongs to a class of linear viscoelastic differential models. Viscoelastic materials can be described as mechanical systems where material points are connected by dashpots (representing energy dissipating devices), springs (representing energy storing devices), or any combination of the two devices. We provide here a short overview of the different possible linear viscoelastic models present in the literature. Following [55, 56], we can represent linear viscoelastic constitutive laws in a canonical linear differential equation that binds the stress tensor, $\boldsymbol{\sigma}$ (without the pressure contribution), and the strain tensor, denoted by $\boldsymbol{\epsilon}$, or the strain rate tensor, denoted by $\dot{\boldsymbol{\epsilon}}$. If we denote the displacement field, in two dimensions, by $\mathbf{u} = (u_1(x, y, t), u_2(x, y, t))$, we can define the infinitesimal strain tensor by $\epsilon_{12} = (\partial_x u_2 + \partial_y u_1)/2$, and the infinitesimal strain rate tensor by $\dot{\epsilon}_{12} = (\partial_x v_2 + \partial_y v_1)/2$

(other components of $\boldsymbol{\epsilon}$ and $\dot{\boldsymbol{\epsilon}}$, are similarly expressed in terms of derivatives of $\mathbf{u}$ and $\mathbf{v}$, respectively). Hence, we can express the family of linear constitutive laws as

$$\left(1 + \sum_{n=1}^{\widehat{N}} \bar{a}_n \frac{\partial^n}{\partial t^n}\right) \boldsymbol{\sigma} = \sum_{m=0}^{\widehat{M}} \bar{b}_m \frac{\partial^m}{\partial t^m} \boldsymbol{\epsilon} \,. \tag{2.2}$$

For $\widehat{N} = \widehat{M} = 1$, we can distinguish the following four different constitutive laws.

1. Considering one non-zero parameter, and two parameters equal to zero, we can recover the following constitutive laws:

    (i) Linear Hookean elastic solids, with $\bar{a}_1 = \bar{b}_1 = 0$ and $\bar{b}_0 \neq 0$

    $$\boldsymbol{\sigma} = \bar{b}_0 \boldsymbol{\epsilon} \tag{2.3}$$

    where $\bar{b}_0 = 2G$, with G the shear modulus, in the case of shear deformation (or, equivalently, $\bar{b}_0 = 2Y$, with Y the Young's modulus, in the case of uniaxial extension). This system is composed of a single spring.

    (ii) Viscous Newtonian fluids, with $\bar{a}_1 = \bar{b}_0 = 0$ and $\bar{b}_1 \neq 0$

    $$\boldsymbol{\sigma} = \bar{b}_1 \dot{\boldsymbol{\epsilon}} \,, \tag{2.4}$$

    where $\bar{b}_1 = 2\eta$, with η the dynamic (shear) viscosity coefficient. This system is composed of a single dashpot.

2. If instead, we consider two non-zero parameters, and one parameter equal to zero, we can recover:

    (i) Kelvin-Voigt elastic solids, with $\bar{a}_1 = 0$ and $\bar{b}_0 \neq \bar{b}_1 \neq 0$

$$\boldsymbol{\sigma} = \bar{b}_0 \boldsymbol{\epsilon} + \bar{b}_1 \dot{\boldsymbol{\epsilon}} \,, \tag{2.5}$$

where $\bar{b}_0 = 2Y, \bar{b}_1 = 2\eta$. This system corresponds to a spring and a dashpot in parallel.

(ii) Maxwell viscoelastic fluids, with $\bar{b}_0 = 0$ and $\bar{a}_1 \neq \bar{b}_1 \neq 0$

$$\boldsymbol{\sigma} + \bar{a}_1 \partial_t \boldsymbol{\sigma} = \bar{b}_1 \dot{\boldsymbol{\epsilon}} \,, \tag{2.6}$$

where $\bar{a}_1 = \lambda_1$, with λ_1 the *relaxation* time, and $\bar{b}_1 = 2\eta$. This system consists of a spring and a dashpot in series. We observe that this model can be derived by considering a system with constant total stress and variable strain rate given by two different contributions: the elastic one, obtained by taking the time derivative of the constitutive laws for Hookean solids, equation (2.3), and the viscous one, solving for the strain rate in equation (2.4). This way, we identify the relationship $\lambda_1 = \eta/G$, that will be discussed more thoroughly in Chapter 5. Moreover, following [11], we can solve for the first order linear ordinary differential equation for the stress as a function of time and obtain

$$\boldsymbol{\sigma}(t) = \frac{2\eta}{\lambda_1} e^{-\frac{t}{\lambda_1}} \int_0^t \dot{\boldsymbol{\epsilon}}(\hat{t}) e^{\frac{\hat{t}}{\lambda_1}} \, d\hat{t} \,, \tag{2.7}$$

where we have assumed both the stress and the strain to be finite at $t = 0$ to eliminate the integration constant. When written this way, we note that, in the Maxwell model, the stress at a given time t depends on the strain rate at time t, as well as the history of the strain rate at all past times,
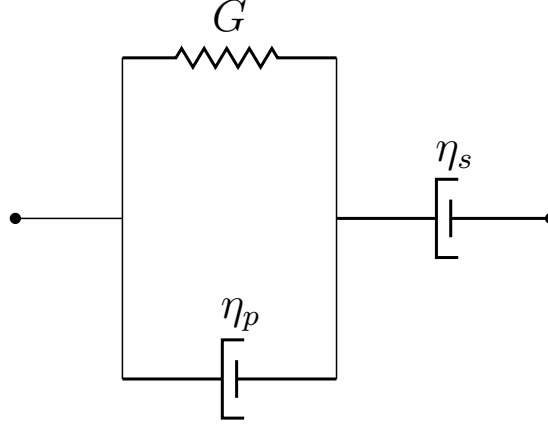
Figure 2.1 Jeffreys model represented as a mechanical system.

with a weighting factor that decays exponentially going backward in time [11]. This feature, typical of the Maxwell model and its extensions, has been called "fading memory".

Since it is quite restrictive to expect a polymeric liquid of a broad molecular weight distribution to be characterized in terms of a single relaxation time [56], we can increase the number of time constants. For $\widehat{N} = 1, \widehat{M} = 2$ and $\bar{b}_0 = 0$, we find the Jeffreys model

$$\boldsymbol{\sigma} + \bar{a}_1 \partial_t \boldsymbol{\sigma} = \bar{b}_1 \partial_t \boldsymbol{\epsilon} + \bar{b}_2 \partial_t \dot{\boldsymbol{\epsilon}} \,, \tag{2.8}$$

where $\bar{a}_1 = \lambda_1$, $\bar{b}_2/\bar{b}_1 = \lambda_2$, with λ_2 the *retardation* time, and $\bar{b}_1 = 2\eta$. In terms of the mechanical system representation, the Jeffreys model corresponds to a dashpot (with viscosity coefficient η_s) attached in series to a Kelvin-Voigt system (with viscosity coefficient η_p and shear modulus G), or, equivalently, a dashpot connected in parallel to a Maxwell system (see Figure 2.1, where we represent the former description).

Hence, we can rewrite the Jeffreys constitutive model as

$$\boldsymbol{\sigma} + \lambda_1 \partial_t \boldsymbol{\sigma} = 2\eta(\dot{\boldsymbol{\epsilon}} + \lambda_2 \partial_t \dot{\boldsymbol{\epsilon}}) \,. \tag{2.9}$$
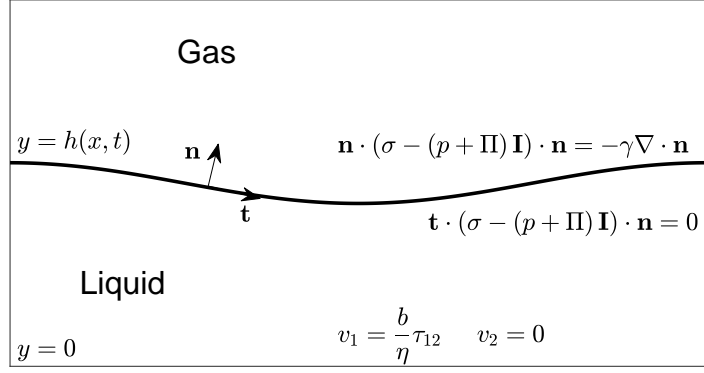
Figure 2.2 Schematic of the fluid interface and boundary conditions. Fluid 1 is the viscoelastic liquid and fluid 2 is the ambient (passive) gas.

In the Jeffreys model, the response to the deformation of a viscoelastic liquid is characterized by two time constants, λ_1 and λ_2, related by

$$\lambda_2 = \lambda_1 \frac{\eta_s}{\eta_s + \eta_p} \, . \tag{2.10}$$

Here, $\eta_s \geq 0$ and $\eta_p \geq 0$ are the viscosity coefficients of the Newtonian solvent and the polymeric solute, respectively, such that $\eta = \eta_s + \eta_p$. Noting that the ratio $\eta_r = \eta_s/(\eta_s + \eta_p) \leq 1$, we have that $\lambda_1 \geq \lambda_2$ [11, 13, 32]. We also observe that, within the Jeffreys model, we recover the Maxwell viscoelastic model when $\lambda_2 = 0$, and a Newtonian fluid when $\lambda_1 = \lambda_2$. Following [11], we can solve for the viscoelastic stress tensor in equation (2.9) as a function of time, obtaining

$$\boldsymbol{\sigma}(t) = \frac{2\eta\lambda_2}{\lambda_1}\dot{\boldsymbol{\epsilon}}(t) + \frac{2\eta}{\lambda_1}\left(1 - \frac{\lambda_2}{\lambda_1}\right)e^{-\frac{t}{\lambda_1}}\int_0^t \dot{\boldsymbol{\epsilon}}(\hat{t})e^{\frac{\hat{t}}{\lambda_1}}\,d\hat{t}, \tag{2.11}$$

where, as in the Maxwell model, we can distinguish the feature of "fading memory".

Figure 2.2 shows a schematic of the fluid interface, represented parametrically by the function $f(x, y, t) = y - h(x, t) = 0$, and the boundary conditions at the free surface $(y = h(x, t))$ and at the x-axis $(y = 0)$. At the latter, we apply the non-penetration

and the Navier slip boundary conditions, with the slip length coefficient denoted by $b \geq 0$. As discussed in [57, 58], long-wave models for thin films can be derived in different slip regimes. In the present work, we will focus on the weak slip regime; for strong slip, a different system of governing equations is derived in [41].

The stress balance at the interface (where the top fluid is passive, as in our study) is expressed as

$$(\boldsymbol{\sigma} - (p + \Pi)\mathbf{I}) \cdot \mathbf{n} = \gamma 2\kappa_m \mathbf{n} \,, \tag{2.12}$$

where $\mathbf{I}$ denotes the identity matrix. In the absence of motion, this condition describes the jump in the pressure across the interface with outward unit normal $\mathbf{n}$, and a local mean curvature κ_m, such that $2\kappa_m = \kappa = -\nabla \cdot \mathbf{n}$, due to the surface tension γ. We define the two mutually orthogonal vectors, $\mathbf{n}$ and $\mathbf{t}$, as

$$\mathbf{n} = \frac{1}{\left(\left(\frac{\partial h}{\partial x} \right)^2 + 1 \right)^{1/2}} \left(-\frac{\partial h}{\partial x}, 1 \right) , \qquad \mathbf{t} = \frac{1}{\left(\left(\frac{\partial h}{\partial x} \right)^2 + 1 \right)^{1/2}} \left(1, \frac{\partial h}{\partial x} \right) . \tag{2.13}$$

The kinematic boundary condition is given by $Df/Dt = f_t + \mathbf{v} \cdot \nabla f = 0$, where substituting $f(x, y, t) = y - h(x, t)$ gives

$$h_t(x, t) = -\frac{\partial}{\partial x} \int_0^{h(x,t)} v_1(x, y) dy \,, \tag{2.14}$$

where to avoid cumbersome notation, we have denoted the first order time derivative of the interface function, $\partial h/\partial t$, by h_t. Similarly, we will denote the second order time derivative, $\partial^2 h/\partial t^2$, by h_{tt}, later on in the text. As anticipated, the boundary conditions at the solid substrate are described by the non-penetration condition for the normal component of the velocity and the Navier slip boundary condition for the tangential one, respectively

$$v_2 = 0, \quad v_1 = \frac{b}{\eta}\sigma_{12}. \tag{2.15}$$

We observe that $b = 0$ implies a no-slip boundary condition with the substrate.

2.3 Thin Film Approximation

We nondimensionalize the system of governing equations using commonly implemented scaling appropriate for the long-wave formulation

$$x = Lx^*, \; (y, h, h_\star, b) = H(y^*, h^*, h_\star^*, b^*), \; (p, \Pi) = P(p^*, \Pi^*), \tag{2.16}$$

$$v_1 = Vv_1^*, \; v_2 = \varepsilon Vv_2^*, \; (t, \lambda_1, \lambda_2) = T(t^*, \lambda_1^*, \lambda_2^*), \; \gamma = \Gamma\gamma^*, \tag{2.17}$$

$$\begin{pmatrix} \sigma_{11} & \sigma_{12} \\ \sigma_{21} & \sigma_{22} \end{pmatrix} = \frac{\eta}{T} \begin{pmatrix} \sigma_{11}^* & \frac{\sigma_{12}^*}{\varepsilon} \\ \frac{\sigma_{21}^*}{\varepsilon} & \sigma_{22}^* \end{pmatrix}, \tag{2.18}$$

where $H/L = \varepsilon \ll 1$ is the small parameter. To balance pressure, viscous and capillary forces, the pressure is scaled with $P = \eta/(T\varepsilon^2)$, the surface tension with $\Gamma = V\eta/\varepsilon^3$, and the time with $T = L/V$. Following the derivation in [13], we can consider the scaled surface tension, γ^*, to be equal to one, by an *ad hoc* choice of the length scale. We note that the Weissenberg number [59], denoted by Wi, given the choice for scales, is $Wi = \lambda_1 V/L = \lambda_1/T = \lambda_1^*$. To avoid cumbersome notation, we drop the superscript '*' and we consider for the rest of this chapter all quantities to be dimensionless.

The incompressibility condition, equation (5.2b), is invariant under rescalings, while the dimensionless forms of equation (2.1a) for the x and y components, respectively, are

$$\varepsilon^2 Re \frac{dv_1}{dt} = \varepsilon^2 \frac{\partial \sigma_{11}}{\partial x} + \frac{\partial \sigma_{21}}{\partial y} - \frac{\partial p}{\partial x}, \tag{2.19a}$$

$$\varepsilon^4 Re \frac{dv_2}{dt} = \varepsilon^2 \left(\frac{\partial \sigma_{12}}{\partial x} + \frac{\partial \sigma_{22}}{\partial y} \right) - \frac{\partial p}{\partial y}, \tag{2.19b}$$

where $Re = \rho U L / \eta$ is the Reynolds number, assumed to be of order $1/\varepsilon$ or smaller. The dimensionless components of the stress tensor given by the Jeffreys model, equation (2.9), satisfy

$$\sigma_{11} + \lambda_1 \frac{\partial \sigma_{11}}{\partial t} = 2 \left(\frac{\partial v_1}{\partial x} + \lambda_2 \frac{\partial}{\partial t} \left(\frac{\partial v_1}{\partial x} \right) \right), \tag{2.20a}$$

$$\sigma_{22} + \lambda_1 \frac{\partial \sigma_{22}}{\partial t} = 2 \left(\frac{\partial v_2}{\partial y} + \lambda_2 \frac{\partial}{\partial t} \left(\frac{\partial v_2}{\partial y} \right) \right), \tag{2.20b}$$

$$\sigma_{12} + \lambda_1 \frac{\partial \sigma_{12}}{\partial t} = \frac{\partial v_1}{\partial y} + \lambda_2 \frac{\partial}{\partial t} \left(\frac{\partial v_1}{\partial y} \right) + \varepsilon^2 \left(\frac{\partial v_2}{\partial x} + \lambda_2 \frac{\partial}{\partial t} \left(\frac{\partial v_2}{\partial x} \right) \right). \tag{2.20c}$$

The kinematic boundary condition, equation (2.14), is invariant under rescaling, while the non-penetration condition and the Navier slip boundary condition for the velocity components parallel to the substrate, given in equation (2.15), in dimensionless form are

$$v_2 = 0, \quad v_1 = b \sigma_{12}, \tag{2.21}$$

where in the weak slip regime $b = O(1)$. The leading-order terms in the governing equations (2.19a) and (2.19b), respectively, are

$$\frac{\partial \sigma_{21}}{\partial y} = \frac{\partial p}{\partial x}, \tag{2.22a}$$

$$\frac{\partial p}{\partial y} = 0. \tag{2.22b}$$

19

The leading-order terms of the normal and tangential components of the stress balance at the free surface, equation (2.12), respectively are

$$p = -\frac{\partial^2 h}{\partial x^2} - \Pi(h) \,, \tag{2.23}$$

and

$$\frac{\partial h}{\partial x}\sigma_{12} = 0 \,, \tag{2.24}$$

where the form of $\Pi(h)$ in equation (2.23) is given by

$$\Pi(h) = \frac{\gamma(1 - \cos\theta_e)}{M h_\star}\left[\left(\frac{h_\star}{h}\right)^{m_1} - \left(\frac{h_\star}{h}\right)^{m_2}\right] \,, \tag{2.25}$$

with $M = (m_1 - m_2)/[(m_2 - 1)(m_1 - 1)]$, where m_1 and m_2 are constants such that $m_1 > m_2 > 1$. In this work, we choose $m_1 = 3$ and $m_2 = 2$, as also widely used in the literature, for instance by the authors in [60, 61, 62], but other values can be modeled as verified in [63]. In equation (2.25), θ_e represents the equilibrium contact angle, formed between the fluid interface $y = h(x,t)$ and the solid substrate. We remark that in equation (2.25) all the quantities are considered nondimensional.

Considering, in general, $\partial h/\partial x \neq 0$, from equation (2.24) follows that $\sigma_{12} = 0$, at the interface. Integrating equation (2.22a) from y to $h(x,t)$, we obtain

$$\sigma_{21} = (y - h)\frac{\partial p}{\partial x} \,. \tag{2.26}$$

Noting that the stress tensor is symmetric, and substituting σ_{21} into equation (2.20c), we obtain (up to the leading-order)

$$\frac{\partial p}{\partial x}(y - h) + \lambda_1 \frac{\partial}{\partial t}\left(\frac{\partial p}{\partial x}(y - h)\right) = \frac{\partial v_1}{\partial y} + \lambda_2 \frac{\partial}{\partial t}\left(\frac{\partial v_1}{\partial y}\right). \tag{2.27}$$

Integrating equation (2.27) from 0 to $y = h(x, t)$ and using the corresponding boundary conditions at the substrate $y = 0$, we obtain

$$\left(1 + \lambda_2 \frac{\partial}{\partial t}\right)\left(v_1 + bh\frac{\partial p}{\partial x}\right) = \left(1 + \lambda_1 \frac{\partial}{\partial t}\right)\left(\left(\frac{y^2}{2} - yh\right)\frac{\partial p}{\partial x}\right). \tag{2.28}$$

Integrating equation (2.28) again from $y = 0$ to $y = h(x, t)$ gives

$$\int_0^{h(x,t)} v_1 dy + bh^2\frac{\partial p}{\partial x} + \lambda_2 \frac{\partial}{\partial t}\int_0^{h(x,t)} v_1 dy + \lambda_2 b\frac{\partial h^2}{\partial t}\frac{\partial p}{\partial x} - \lambda_2 h_t v_1(y = h(x,t)) -$$
$$\lambda_2 h_t bh\frac{\partial p}{\partial x} = -\frac{h^3}{3}\frac{\partial p}{\partial x} - \lambda_1 h^2 h_t \frac{\partial p}{\partial x} + \lambda_1 \frac{h^2}{2}h_t\frac{\partial p}{\partial x}. \tag{2.29}$$

Taking the spatial derivative of the latter equation and substituting it into the kinematic boundary condition, equation (2.14), we obtain a long-wave approximation in terms of v_1 and $h(x, t)$

$$h_t + \lambda_2 \left[h_{tt} + \frac{\partial}{\partial x}(v_1(y = h(x,t))h_t)\right] = \frac{\partial}{\partial x}\left[(1 + \lambda_1 \partial_t)\left(\frac{h^3}{3}\frac{\partial p}{\partial x}\right)\right] +$$
$$(1 + \lambda_2 \partial_t)\left(bh^2\frac{\partial p}{\partial x}\right) - \frac{\partial}{\partial x}\left[\left(\lambda_1 \frac{h^2}{2}\frac{\partial p}{\partial x} + \lambda_2 bh\frac{\partial p}{\partial x}\right)h_t\right]. \tag{2.30}$$

To write this in a closed form relation for $h(x, t)$, we note that equation (2.28) can be written in a more compact form as a linear ordinary differential equation (ODE) for v_1, assuming all other quantities known at a given time, as

$$v_1 + \lambda_2 \frac{\partial v_1}{\partial t} = -(1 + \lambda_2 \partial_t)bh\frac{\partial p}{\partial x} + (1 + \lambda_1 \partial_t)\left[\left(\frac{y^2}{2} - hy\right)\frac{\partial p}{\partial x}\right]. \tag{2.31}$$

One can simply solve this linear ODE, obtaining

$$v_1 = \frac{1}{\lambda_2} \int_{-\infty}^t e^{-\frac{t-t'}{\lambda_2}} \bar{f}(x, y, t') dt' , \qquad (2.32)$$

with $\bar{f}$ equal to the right-hand side of equation (2.31). Integration by parts can be performed to recast equation (2.32) at $y = h(x, t)$, and one finally obtains equations

$$(1 + \lambda_2 \partial_t)h_t + \frac{\partial}{\partial x} \left\{ (\lambda_2 - \lambda_1) \left(\frac{h^2}{2} Q - hR \right) h_t + \right.$$
$$\left. \left[(1 + \lambda_1 \partial_t) \frac{h^3}{3} + (1 + \lambda_2 \partial_t) bh^2 \right] \frac{\partial}{\partial x} \left(\frac{\partial^2 h}{\partial x^2} + \Pi(h) \right) \right\} = 0 , \qquad (2.33)$$

where $Q = Q(h)$ and $R = R(h)$ satisfy, respectively,

$$(1 + \lambda_2 \partial_t)Q = -\frac{\partial}{\partial x} \left(\frac{\partial^2 h}{\partial x^2} + \Pi(h) \right) , \qquad (2.34a)$$

$$(1 + \lambda_2 \partial_t)R = -h\frac{\partial}{\partial x} \left(\frac{\partial^2 h}{\partial x^2} + \Pi(h) \right) . \qquad (2.34b)$$

We note that in the absence of viscoelasticity (i.e., with $\lambda_1 = \lambda_2$), equations (2.33) and (2.34) reduce to the well-known long-wave formulation for viscous Newtonian films (see, e.g., [2]).

2.4   Numerical Methods

2.4.1   Discretization of the Domain

To numerically solve equations (2.33) and (2.34), we use the finite differences technique in an Eulerian framework. The spatial domain $[0, \Lambda]$ is discretized by uniformly spaced grid points, that constitute a vertex-centered (structured) grid (see Figure 2.3). Following the natural order from left to right, adjacent vertices are associated to the indices $i - 1, i, i + 1$, respectively. Thus, we let $x_i = x_0 + i\Delta x, \ i = 1, 2, \ldots, N$ (where
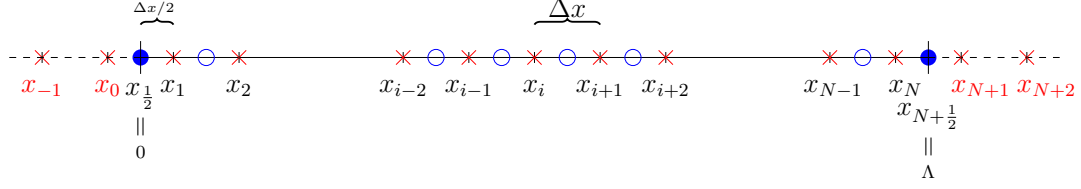
Figure 2.3 Discretization of the spatial domain.

$N = \Lambda/\Delta x$, and Δx is the grid size), so that the endpoints of the physical domain, 0 and Λ, correspond to the $x_1 - \frac{\Delta x}{2}$ and $x_N + \frac{\Delta x}{2}$ cell-centers, respectively (denoted by blue solid discs in Figure 2.3). Similarly, we discretize the time domain and denote by h_i^n the approximation to the solution at the point $(x_i, n\Delta t)$, where $n = 0, 1, \ldots$ indicates the number of time steps, and Δt is the temporal step size.

In order to approximate the fourth order spatial derivative in equation (2.33), we need at least a 5-point stencil to obtain second order accuracy [64]. We define the first and third derivatives at the cell-centers of the domain, indicated by blue circles in Figure 2.3, so that the second and fourth order derivatives are centered at the grid points, marked with red crosses, (see [65] for a detailed description).

2.4.2 Discretization of the Governing Equations and Boundary Conditions

To simplify, we first consider a viscoelastic liquid of Maxwell type, that is, with $\lambda_2 = 0$. Thus, the governing equations (2.33) and (2.34) reduce to a first order in time formulation given by

$$
\begin{aligned}
h_t - \frac{\partial}{\partial x} \Bigg\{ &\lambda_1 \frac{h^2}{2} \left(\frac{\partial^3 h}{\partial x^3} + \Pi'(h)\frac{\partial h}{\partial x} \right) h_t - \\
&\left[\frac{h^3}{3} + bh^2 + \lambda_1 \frac{\partial}{\partial t}\left(\frac{h^3}{3} \right) \right] \left(\frac{\partial^3 h}{\partial x^3} + \Pi'(h)\frac{\partial h}{\partial x} \right) \Bigg\} = 0 \,.
\end{aligned}
\tag{2.35}
$$

We recall that the class of θ-schemes for the finite difference discretization of the time derivative, can be written as

$$\frac{h_i^{n+1} - h_i^n}{\triangle t} = - \left[\theta F_i^n + (1-\theta) F_i^{n+1} \right], \quad i = 1, 2, \ldots, N, \quad (2.36)$$

where $0 \leq \theta \leq 1$ and the nonlinear function F_i is related to the spatial discretization of equations (2.33) and (2.34). Here, $\theta = 0$ leads to the implicit (backward) Euler scheme, $\theta = 1$ to the explicit (forward) Euler scheme, and $\theta = 1/2$ to the implicit second order Crank-Nicolson scheme [64]. We will use the last, similarly to [61, 66], leading to a system of N nonlinear algebraic equations for h_i^{n+1}, $i = 1, 2, \ldots, N$. Following the procedure outlined in [65], we linearize the nonlinear terms with Newton's method by expanding $h_i^{n+1} = h_i^{\dagger} + \xi_i$, and $F_i^{n+1} = F_i^{\dagger} + (\partial F_i^{\dagger}/\partial \xi_j)\xi_j$, for $i = 1, 2 \ldots, N$, $j = 1, 2 \ldots, N$; where $h^{\dagger}$ is a guess for the solution (commonly the previous time step solution h^n), ξ is the correction term, and the notation $F_i^{\dagger}$ indicates that F_i is calculated using $h_i^{\dagger}$. Once the linearized system is solved for the correction term, the guess for the solution is updated, and this iterative scheme is repeated until the convergence criterion is met (up to a desired tolerance).

To solve the discrete equations efficiently, we use an adaptive time step Δt. In fact, Δt is increased to accelerate the time integration at stages where the solution does not vary rapidly. On the other hand, Δt is decreased when the solution shows a high variation, where the Newton's method requires more than a few steps to converge. The behavior of the solution is discussed in more detail in Section 2.5, where we present our numerical results.

To discretize equation (2.35), we isolate the time derivatives from the spatial ones, so that we can apply an iterative scheme to find the approximation to the solution at the new time step. We do so by differentiating the spatial derivatives and, assuming the partial derivatives of $h(x,t)$ to be continuous, we obtain

$$\underbrace{\frac{\partial}{\partial x}\left[\left(\frac{h^3}{3}+bh^2\right)\left(\frac{\partial^3 h}{\partial x^3}+\Pi'(h)\frac{\partial h}{\partial x}\right)\right]}_{f(h)}+$$

$$\underbrace{\left[1-\frac{1}{2}\lambda_1\frac{\partial}{\partial x}\left[h^2\left(\frac{\partial^3 h}{\partial x^3}+\Pi'(h)\frac{\partial h}{\partial x}\right)\right]\right]}_{g(h)}h_t+$$

$$\frac{\partial}{\partial t}\underbrace{\left(\frac{\partial h}{\partial x}\right)}_{l(h)}\underbrace{\left\{-\frac{1}{2}\lambda_1\left[h^2\left(\frac{\partial^3 h}{\partial x^3}+\Pi'(h)\frac{\partial h}{\partial x}\right)\right]\right\}}_{m(h)}+$$

$$\lambda_1\frac{\partial}{\partial t}\underbrace{\left[\frac{\partial}{\partial x}\left(\frac{h^3}{3}\left(\frac{\partial^3 h}{\partial x^3}+\Pi'(h)\frac{\partial h}{\partial x}\right)\right)\right]}_{p(h)}=0\,. \tag{2.37}$$

We can now differentiate the time derivatives and use the Crank-Nicolson scheme on the term $f(h)$ as

$$g(h)_i^n\frac{h_i^{n+1}-h_i^n}{\Delta t}+m(h)_i^n\frac{l(h)_i^{n+1}-l(h)_i^n}{\Delta t}+\lambda_1\frac{p(h)_i^{n+1}-p(h)_i^n}{\Delta t}=$$
$$-\frac{1}{2}\left[f(h)_i^n+f(h)_i^{n+1}\right]\,. \tag{2.38}$$

The nonlinear terms h^2 and h^3 are computed at the cell-centers, as outlined in [65, 67]. After the linearization, we obtain a system of equations of the form $A_1\xi=B_1$, that we numerically solve for the correction term, ξ, using a direct method [68]. The initial condition given for $h(x,0)$ is a known function that either describes the initial perturbation of the fluid interface or a circular cap for the drop simulations (see Section 2.5).

For $\lambda_2\neq 0$, the governing equation (2.33), after differentiating the spatial derivative, and isolating the time derivatives, can be recast to a second order in time equation given by

$$\lambda_2 h_{tt} + \underbrace{\frac{\partial}{\partial x}\left[\left(\frac{h^3}{3}+bh^2\right)\left(\frac{\partial^3 h}{\partial x^3}+\Pi'(h)\frac{\partial h}{\partial x}\right)\right]}_{f(h)} +$$

$$\underbrace{\left\{1+(\lambda_2-\lambda_1)\left[\frac{\partial}{\partial x}\left(\frac{h^2}{2}Q-hR\right)\right]\right\}}_{\widehat{g}(h)}h_t + \underbrace{\frac{\partial}{\partial t}\left(\frac{\partial h}{\partial x}\right)}_{l(h)}\underbrace{(\lambda_2-\lambda_1)\left(\frac{h^2}{2}Q-hR\right)}_{\widehat{m}(h)} +$$

$$\lambda_1\underbrace{\frac{\partial}{\partial t}\left[\frac{\partial}{\partial x}\left(\frac{h^3}{3}\left(\frac{\partial^3 h}{\partial x^3}+\Pi'(h)\frac{\partial h}{\partial x}\right)\right)\right]}_{p(h)} + \lambda_2\underbrace{\frac{\partial}{\partial t}\left[\frac{\partial}{\partial x}\left(bh^2\left(\frac{\partial^3 h}{\partial x^3}+\Pi'(h)\frac{\partial h}{\partial x}\right)\right)\right]}_{q(h)} = 0,$$

$$(2.39)$$

where now the discrete versions of the equations (2.34a) and (2.34b) are:

$$\frac{Q_i^{n+1}-Q_i^n}{\Delta t} = -\frac{Q_i^n}{\lambda_2}-\frac{1}{\lambda_2}\left(\frac{\partial^3 h}{\partial x^3}+\Pi'(h)\frac{\partial h}{\partial x}\right)_i^n, \qquad (2.40\text{a})$$

$$\frac{R_i^{n+1}-R_i^n}{\Delta t} = -\frac{R_i^n}{\lambda_2}-\frac{1}{\lambda_2}h_i^n\left(\frac{\partial^3 h}{\partial x^3}+\Pi'(h)\frac{\partial h}{\partial x}\right)_i^n, \qquad (2.40\text{b})$$

that we simply solve by the forward Euler method with initial conditions $Q_i^0 = 0$ and $R_i^0 = 0$. Again, discretizing all terms and applying Crank-Nicolson scheme, we obtain

$$\lambda_2\frac{h_i^{n+1}-2h_i^n+h_i^{n-1}}{\Delta t^2} + \widehat{g}(h)_i^n\frac{h_i^{n+1}-h_i^n}{\Delta t} + \widehat{m}(h)_i^n\frac{l(h)_i^{n+1}-l(h)_i^n}{\Delta t} +$$

$$\lambda_1\frac{p(h)_i^{n+1}-p(h)_i^n}{\Delta t} + \lambda_2\frac{q(h)_i^{n+1}-q(h)_i^n}{\Delta t} = -\frac{1}{2}\left[f(h)_i^n+f(h)_i^{n+1}\right]. \qquad (2.41)$$

Similarly, we proceed by linearizing the nonlinear terms and solving the resulting system $A_2\xi = B_2$. We note that in this case the partial differential equation is second order in time. We therefore need a two-step method with a second initial condition, in addition to the prescribed $h(x,0)$. We use $h_t(x,0) = 0$, resulting from the assumption that the considered films and drops are initially at rest.

At the endpoints of the domain we impose the $\partial h/\partial x = \partial^3 h/\partial x^3 = 0$ boundary conditions. The condition $\partial h/\partial x = 0$ gives the value of h at the two ghost points x_0

and x_{N+1} outside the physical domain, i.e., $h_0 = h_1$ and $h_{N+1} = h_N$; the condition $\partial^3 h / \partial x^3 = 0$ specifies the two ghost points x_{-1} and x_{N+2}, i.e., $h_{-1} = h_2$ and $h_{N+2} = h_{N-1}$.

2.5 Results and Discussion

2.5.1 Linear Stability Analysis

To study the fluid response to a prescribed disturbance, we perform the linear stability analysis (LSA). We perturb a flat film of initial thickness h_0 by a Fourier mode of amplitude δh_0 (such that $\delta \ll 1$), with wavenumber k and growth rate ω. Hence, we let $h(x,t) = h_0 + \delta h_0 e^{ikx+\omega t}$. The dispersion relation $\omega = \omega(k)$ is

$$
\lambda_2 \omega^2 + \left[1 + (k^4 - k^2 \Pi'(h_0)) \left(\lambda_1 \frac{h_0^3}{3} + \lambda_2 b h_0^2 \right) \right] \omega +
$$
$$
(k^4 - k^2 \Pi'(h_0)) \left(\frac{h_0^3}{3} + b h_0^2 \right) = 0 \,. \tag{2.42}
$$

Solving for the two roots of this quadratic equation, we obtain one strictly negative (stable) root, say ω_2, and one root with varying sign, say ω_1. The latter one is positive (unstable) for $k^2 < \Pi'(h_0)$. We note that both the critical wavenumber, k_c, given by $k_c^2 = \Pi'(h_0)$, and the wavenumber of maximum growth, $k_m = k_c/\sqrt{2}$, do not depend on λ_1 and λ_2, nor on the slip length b (as also discussed in [41]). Moreover, we note that in the absence of retardation, i.e., for $\lambda_2 = 0$, the dispersion relation for a film of Maxwell type leads to an unbounded growth rate for $\lambda_1 = -3/h_0^3 (k^4 - k^2 \Pi'(h_0))$. However, for $\lambda_2 \neq 0$, the growth rate ω is always finite. This observation about the unboundedness of the growth rate for Maxwellian films has also been drawn by other authors, see, for instance [28, 32]. We also note that the maximum growth rate, $\omega_m = \omega(k_m)$, is an increasing function of λ_1 and b, while a decreasing function of λ_2.
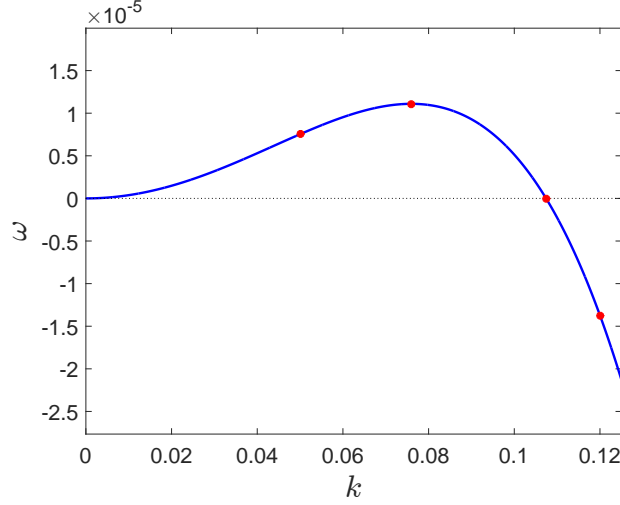
Figure 2.4 The comparison of the computed growth rate (red circles) with the prediction of the LSA (blue solid line) given by equation (2.42), for $h_0 = 1$, $h_\star = 0.01$, $b = 0$, $\lambda_2 = 0$, $\lambda_1 = 5$.

In the following subsection, we will discuss in more details the effects of λ_1, λ_2, and b on the dewetting dynamics.

2.5.2 Dewetting of Thin Viscoelastic Films

In this subsection, we present the results for a dewetting thin film under the influence of the van der Waals interaction force. We perturb the initially flat fluid interface of thickness h_0, as anticipated in the previous subsection, with $k = k_m$ and $\delta = 0.01$. We choose the domain size to be equal to the wavelength of maximum growth, that is $\Lambda = 2\pi/k_m$, unless noted otherwise. For unstable perturbations, the van der Waals interaction is attractive, causing the liquid interface to retract towards the substrate. When the fluid interface approaches the substrate, dewetting occurs, i.e., a hole (nominally a dry region) forms, leading to the formation of a rim that retracts and collects the liquid at the edge. The system then gradually evolves toward an equilibrium state, corresponding to separate drops on the substrate characterized by the equilibrium contact angle, θ_e. We are mainly interested in the dynamics of the instabilities and the resulting morphologies, so we will only show results for unstable

28

films. The set of parameters used for all simulations shown hereafter is: an initial normalized height of the fluid $h_0 = 1$, an equilibrium film thickness $h_\star = 0.01$, a constant contact angle $\theta_e = 45°$, a normalized surface tension $\gamma = 1$, and a fixed grid size $\Delta x = 5 \times 10^{-3}$, unless specified differently. All numerical results shown in this work are verified to be mesh-independent. We also validate our numerical investigations by comparing the growth rate for the early times with the LSA (equation (2.42)). Figure 2.4 shows the comparison of the computed growth rates for different wavenumbers (red circles) with the one given by the dispersion relation $\omega_1(k)$ (blue solid curve), for a film with $\lambda_1 = 5$ and $\lambda_2 = 0$, when $b = 0$. For these numerical simulations, we choose the domain size according to the wavelength that corresponds to the specified wavenumber. Although not shown here, comparisons between computed growth rates and the LSA are performed for all following results as well.

We begin our analysis with the simplest case of a viscoelastic fluid of Maxwell type, that is, with $\lambda_2 = 0$, and with no-slip at the substrate, $b = 0$. Figures 2.5(a)– 2.5(c) show the evolution of four distinct films with different values of the relaxation time, $\lambda_1 = 0$ (blue circles), 2 (cyan triangles), 4 (green squares), and 6 (red crosses), at three selected times. The interfacial dynamics can be divided into three phases. The initial regime corresponds to the short-time viscous response of the fluid, until the film separates in two retracting rims (Figure 2.5(a)). During intermediate times, the fastest dynamics occurs, and the liquid responds elastically: in this stage holes and retracting edges form (Figure 2.5(b)). In the last phase, the rims grow further in height, until the interface reaches its final configuration, attaining an equilibrium contact angle with the substrate (Figure 2.5(c)). During this third stage, the fluid shows a long-time Newtonian response again. These observations of the dewetting dynamics are in agreement with results in [31, 32]; moreover, we note that the shape of the dewetting front that forms a retracting rim is consistent with findings in previous experimental [22, 23] or numerical [32] studies. In addition, we observe that non-zero
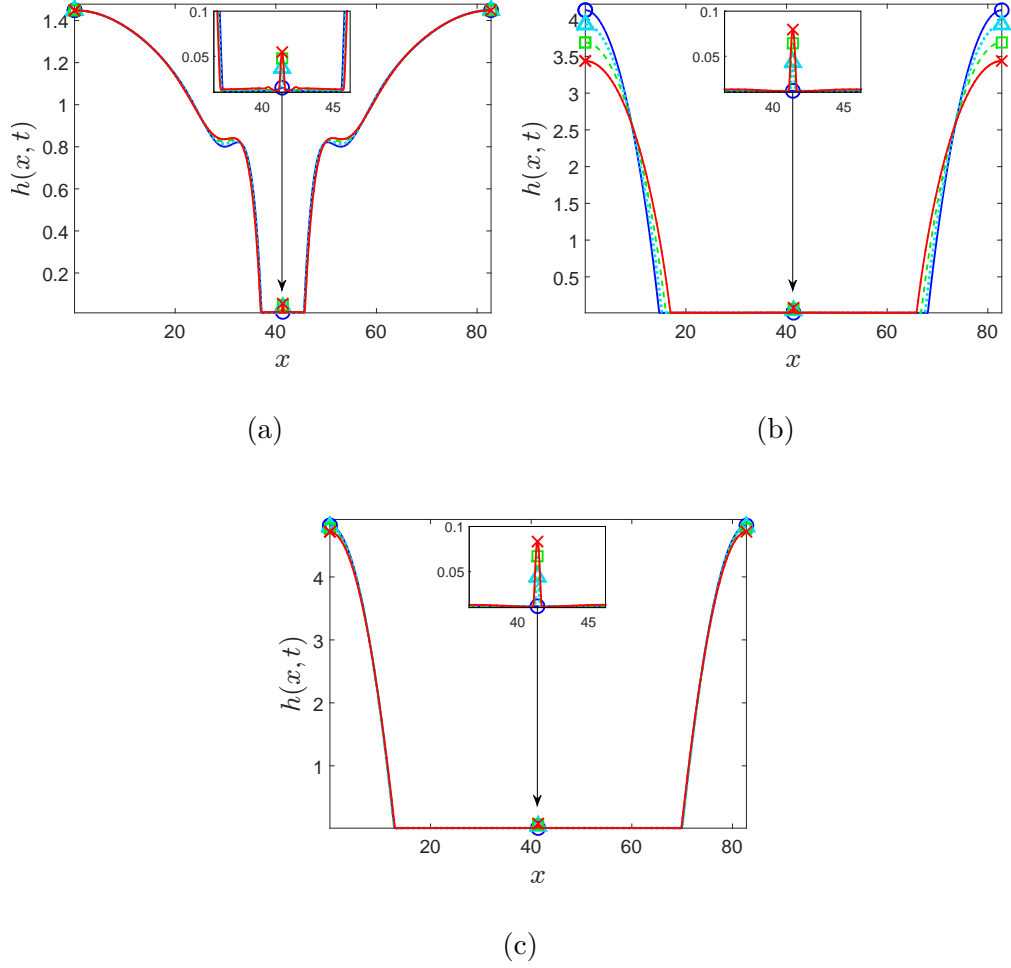
Figure 2.5 (a)-(c) Evolution of four distinct dewetting films with $\lambda_1 = 0$ (blue circles), 2 (cyan triangles), 4 (green squares), 6 (red crosses), at three selected times. At $t = 3.345 \times 10^5$ (a), the separation of the rims and the formation of a secondary droplet for values of $\lambda_1 \neq 0$ are shown. In (b), $t = 3.37 \times 10^5$, and in (c), $t = 3.38 \times 10^5$. The insets show a close-up of the region where a secondary droplet forms.

values of λ_1 not only slightly increase the speed of the breakup, but also allow for the formation of a satellite droplet, in contrast to the Newtonian film (with $\lambda_1 = 0$). In particular, in the inset in Figure 2.5(a), we distinguish the formation of dips on the interface in the vicinity of the secondary droplet formed in the film with the highest value of $\lambda_1 = 6$. These oscillations disappear at a later time, as the interface around the secondary droplet flattens (Figures 2.5(b) and 2.5(c)). To study analytically the observed oscillations, we perform a linear analysis, along the lines of the one presented

in [13, 58], for the inner region of the growing hole. We find that the linearized solution, under quasi steady state conditions, does not depend on the viscoelastic parameters. Therefore the oscillations that the viscoelastic interface exhibits in the inner region of the dewetting hole cannot be analytically described with a linear analysis. In what follows, we also show that increasing the elasticity even further, provided a small retardation time (e.g., $\lambda_2 = 0.01$) is also included, can lead to multiple strongly pronounced dips, and subsequently form numerous secondary droplets.

Next, we take into account the viscosity of the Newtonian solvent by including $\lambda_2 \neq 0$. As anticipated in the previous subsection, λ_2 has the effect of slowing down the growth rate of the instability. We find that a slower dynamics provides a numerical advantage as well: By stabilizing the computations, hence avoiding the high Weissenberg number problem (see [59] and references therein for a discussion on the computational challenges regarding this aspect), which otherwise can destabilize the numerical solutions. In fact, our simulation results show that when $\lambda_2 = 0$, for $\lambda_1 > 6$, unfeasible small time steps would be required to overcome numerical instabilities, due to the rapid growth rate for Maxwellian films. By contrast, when viscoelastic films of Jeffreys type are considered, even a small contribution of the retardation time (e.g., $\lambda_2 = 0.01$) allows simulations of films with a high Weissenberg number, that are yet numerically stable.

Figures 2.6(a)–2.6(c) show the evolution of a viscoelastic dewetting film with $\lambda_1 = 10$ and $\lambda_2 = 0.01$, at three selected times. In particular, in the inset of Figure 2.6(a), we observe the separation of the two rims (at time $t = 3.341 \times 10^5$), and the formation of oscillations on the interface. These oscillations lead to multiple secondary droplets that are shown in Figure 2.6(b) ($t = 3.345 \times 10^5$), and that remain present until the final configuration shown in Figure 2.6(c) ($t = 4 \times 10^5$). To our knowledge, secondary droplets of this nature have not been reported in numerical investigations of thin viscoelastic films, but their observation is consistent with experimental findings
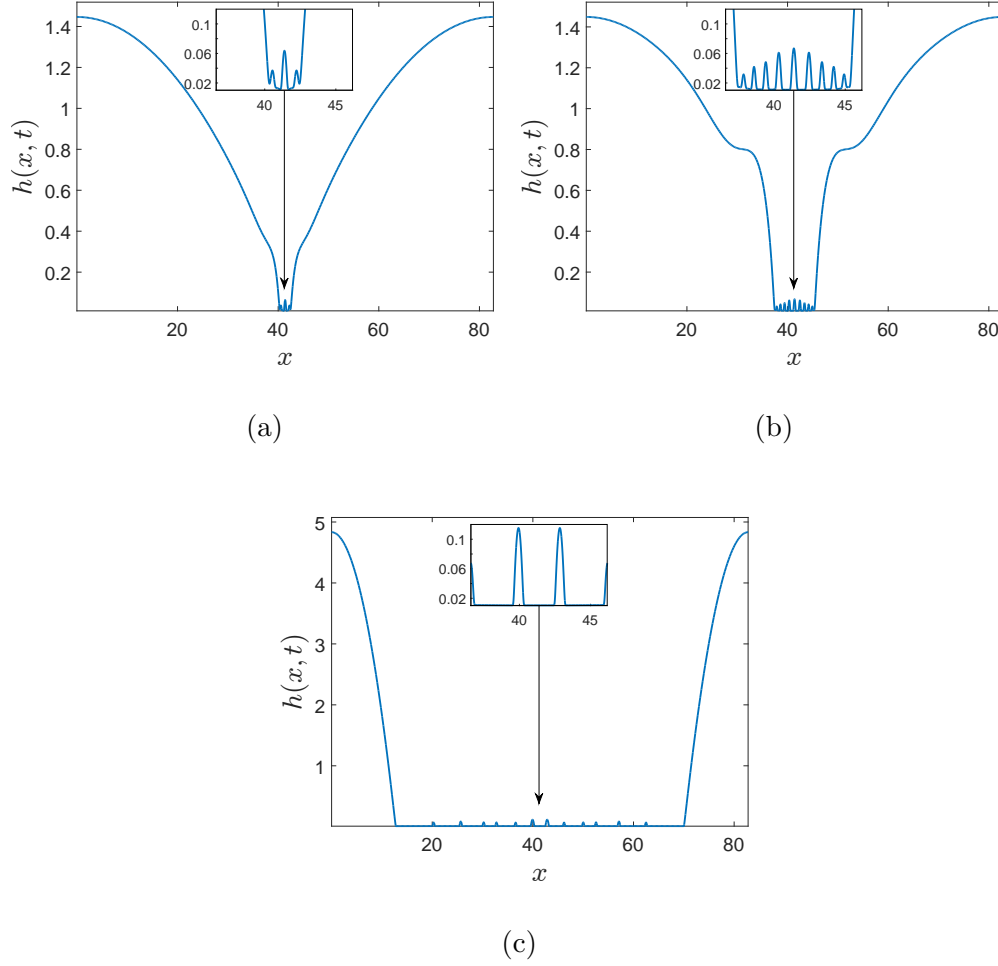
Figure 2.6 Evolution of a viscoelastic film with $h_0 = 1$, $h_\star = 0.01$, $b = 0$, $\lambda_1 = 10$ and $\lambda_2 = 0.01$, at three selected times. (a) The separation of the two rims ($t = 3.341 \times 10^5$). (b) The formation of wrinkles that lead to the formation of secondary droplets ($t = 3.345 \times 10^5$). The secondary droplets remain present until the final configuration shown in (c) ($t = 4 \times 10^5$). In all three Figures, the insets show a detailed close-up of the dewetting region.

(see for instance [17, 19, 21]). We can rheologically explain the presence of the secondary droplets by noting that a higher relaxation time, λ_1, manifests a higher molecular weight of the polymers [69]. Thus, in the presence of an extensional flow, such as the one produced by the two separating rims, the chains of molecules are more stretched, and the elastic response to deformation is more visible. Similar considerations can be found in studies on beads-on-string structures of viscoelastic
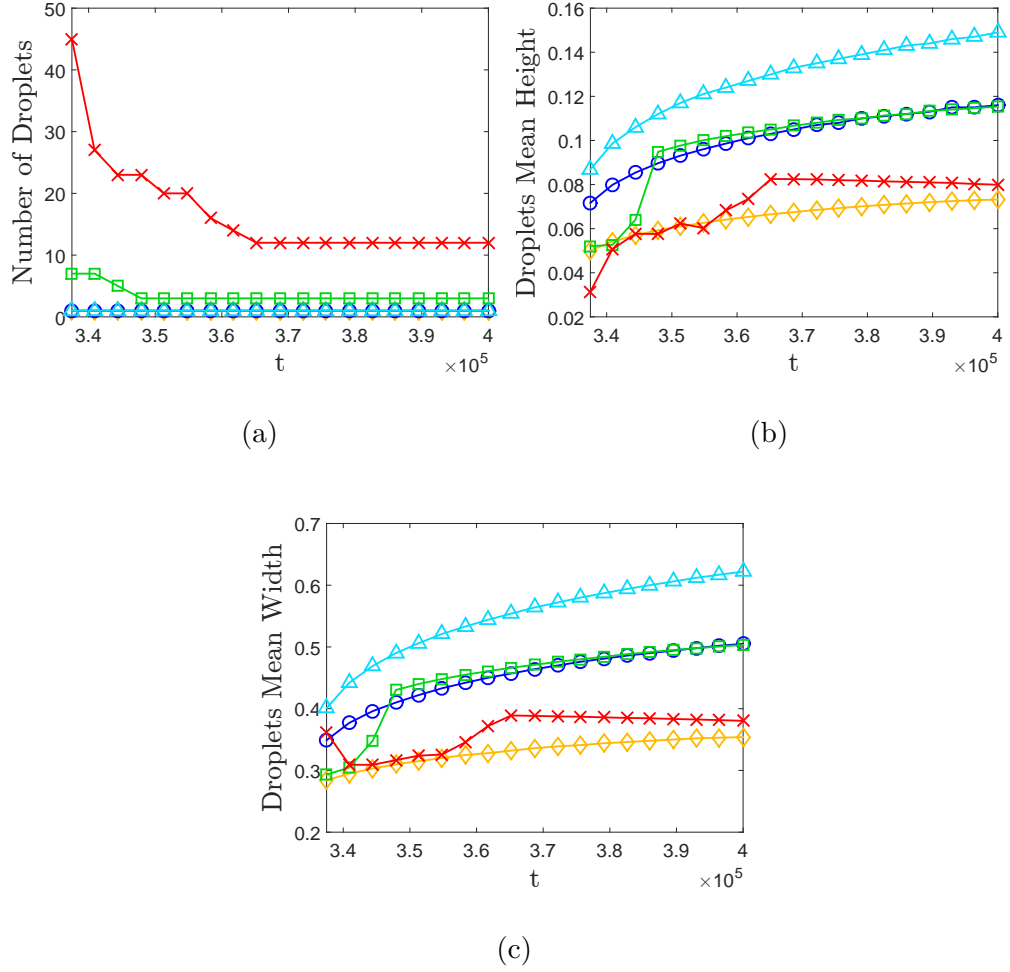
Figure 2.7 Evolution of the secondary droplets with $h_0 = 1$, $h_\star = 0.01$, $b = 0$, $\lambda_2 = 0.01$, and $\lambda_1 = 2$ (yellow diamonds), 4 (blue circles), 6 (cyan triangles), 8 (green squares), and 10 (red crosses). (a) The number of droplets versus time. For $\lambda_1 = 2, 4, 6$, only one secondary droplet is formed, so the lines overlap. For values of $\lambda_1 > 6$, there are multiple secondary droplets; due to coalescence, the number of secondary droplets decrease in time. (b) The mean height of the secondary droplets versus time. (c) The width (at half height) of the secondary droplets versus time.

jets (see, for instance, [70, 71]). We note that both in our study and in the cited works on extensional flows of viscoelastic filaments, there is no strong correlation between the breakup time and the relaxation time. The latter mostly influences the formation of droplets, their migration and coalescence [71]. We also note that additional simulations have shown that λ_2 does not affect significantly the final configurations (results not shown for brevity). Furthermore, we remark that a high Weissenberg number does not

break the assumption of small shear rates, for which linear viscoelastic constitutive models, such as the one that we consider, are valid. This observation is confirmed numerically by analyzing the quantity $|\partial v_1/\partial x| \sim |h_t(x,t)/h(x,t)|$ over the entire time of the evolution. In particular, for the times presented in Figures 2.6(a)–2.6(b), $|\partial v_1/\partial x|$ does not exceed the value of 10^{-2}, and for the final stage of the evolution, shown in Figure 2.6(c), it has an order of magnitude of 10^{-5}. Hence, we can confirm that for the flows considered, even for a high value of the dimensionless relaxation time, $\lambda_1 U/L$, which corresponds to a high Weissenberg number (see Section 2.3), the assumption of small deformation gradients is not violated.

We proceed by analyzing the influence of λ_1 on the characteristic length scales of the secondary droplets. The corresponding results are shown in Figure 2.7, where we keep $\lambda_2 = 0.01$, and study the resulting morphologies for $\lambda_1 = 2, 4, 6, 8, 10$. Figure 2.7(a) shows the number of secondary droplets versus time. For $\lambda_1 = 2, 4, 6$, denoted by yellow diamonds, blue circles, and cyan triangles respectively, only one secondary droplet is formed. Whereas, for values of $\lambda_1 = 8, 10$, denoted by green squares and red crosses respectively, multiple secondary droplets form. At later times and when $\lambda_1 = 8, 10$, the secondary droplets can coalesce, resulting in a sudden change in their numbers, height, and width. From Figure 2.7(a), we also note that the merging of secondary droplets is much more severe for $\lambda_1 = 10$, implying that the elastic force is responsible for the secondary droplets migration and coalescence.

Finally, we focus on the influence of the slip coefficient b. In Figures 2.8(a)–2.8(c), we fix the viscoelastic parameters $\lambda_1 = 10$, $\lambda_2 = 0.01$, and consider $b = 0$ (blue circles), 0.001 (cyan triangles), 0.01 (green squares), and 0.1 (red crosses). The results show that the dynamics with a non-zero slip coefficient is faster. In fact, we can see in Figure 2.8(a), that the film with $b = 0.1$ is already separating at time $t = 2.5 \times 10^5$, whereas the other films are still in the initial phase in which the perturbation has not grown significantly. Moreover, we see in Figure 2.8(b) at time $t = 3.34 \times 10^5$, and in
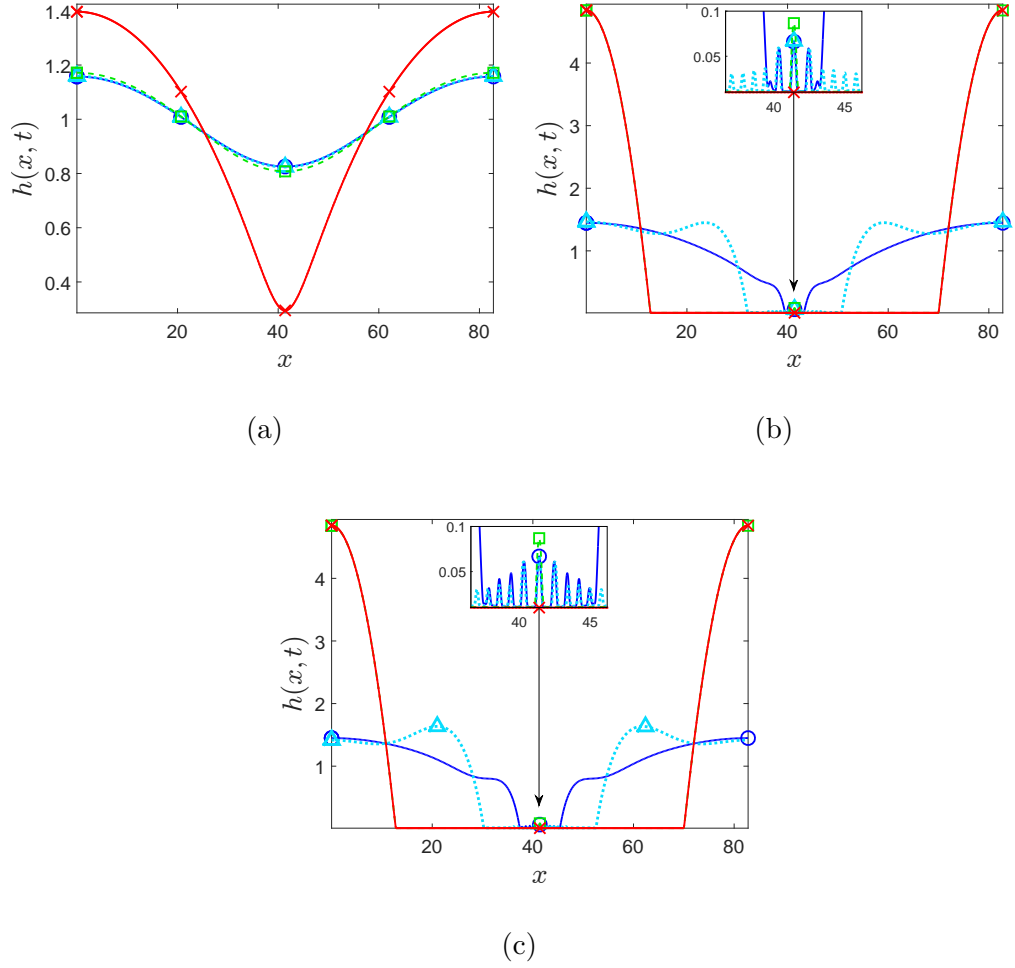
Figure 2.8 Evolution of dewetting films for $h_0 = 1$, $h_\star = 0.01$, $\lambda_1 = 10$ and $\lambda_2 = 0.01$ at three selected times, for $b = 0$ (blue circles), 0.001 (cyan triangles), 0.01 (green squares), and 0.1 (red crosses). At time $t = 2.5 \times 10^5$ in (a), the film with $b = 0.1$ is separating, while in (b) at time $t = 3.34 \times 10^5$, and in (c) at time $t = 3.345 \times 10^5$, the films with $b = 0.01$ and $b = 0.1$ are already fully developed. We note that for large slip, the evolution is faster and no satellite droplets form. As b is decreased, the dynamics is slower and satellites form. The insets show a close-up of the secondary droplets.

Figure 2.8(c) at time $t = 3.345 \times 10^5$, that the films with $b = 0.01$, and $b = 0.1$ are already fully developed, whereas the ones with $b = 0$, and $b = 0.001$ are still retracting. We show that not only does slip have an influence on the dynamics of the evolution, but it also has two main effects on the resulting morphologies of the interface: First, by raising the height of the retracting rims in the early stage of the evolution (we

35
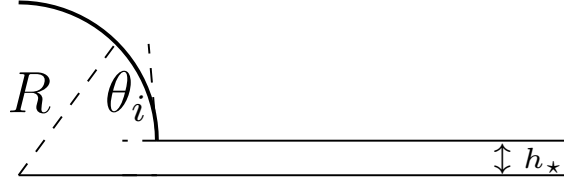
Figure 2.9 Schematic of the planar cap of fluid.

note in Figure 2.8(b) the dip in the interface of the receding rim for the film with $b = 0.001$ in contrast to the one with no-slip); Second, by preventing the formation of the secondary droplets in the final configuration. In fact, multiple satellite droplets form in the cases with $b = 0$, and $b = 0.001$, while only one secondary droplet remains present when $b = 0.01$, and none when $b = 0.1$.

2.5.3 Spreading and Receding Viscoelastic Drops

Spreading Drops   Next, we discuss spreading of a planar viscoelastic drop. The initial condition is a circular cap of radius R and center $(0, -R \cos \theta_i)$, that lies on the substrate with an offset of thickness $h_\star$, as depicted in Figure 2.9. We specify the initial contact angle between the fluid interface and the solid substrate, called θ_i, different from the equilibrium angle, denoted by θ_e. The latter is implicitly defined by the form of the disjoining pressure given by equation (2.25). We investigate the dynamic contact angle, θ_D, formed at the moving contact line, and study its relation with θ_e. θ_D is calculated as the slope of the tangent line at the inflection point of the fluid interface $h(x, t)$. In the discussion that follows, we start with $\theta_i = 30°$, and let the drop relax to $\theta_e = 15°$. For all cases shown, we impose a no-slip boundary condition.

Figure 2.10 shows the comparison of numerical simulations of a Newtonian drop, with $\lambda_1 = \lambda_2 = 0$ (blue dotted curve), versus a viscoelastic drop with $\lambda_1 = 15, \lambda_2 = 0.01$ (red solid curve), at three selected times ($t = 10, 50, 100$). Figures 2.10(a)–2.10(c), that use $h_\star = 0.01$, illustrate the difference in the velocity of the contact line. In
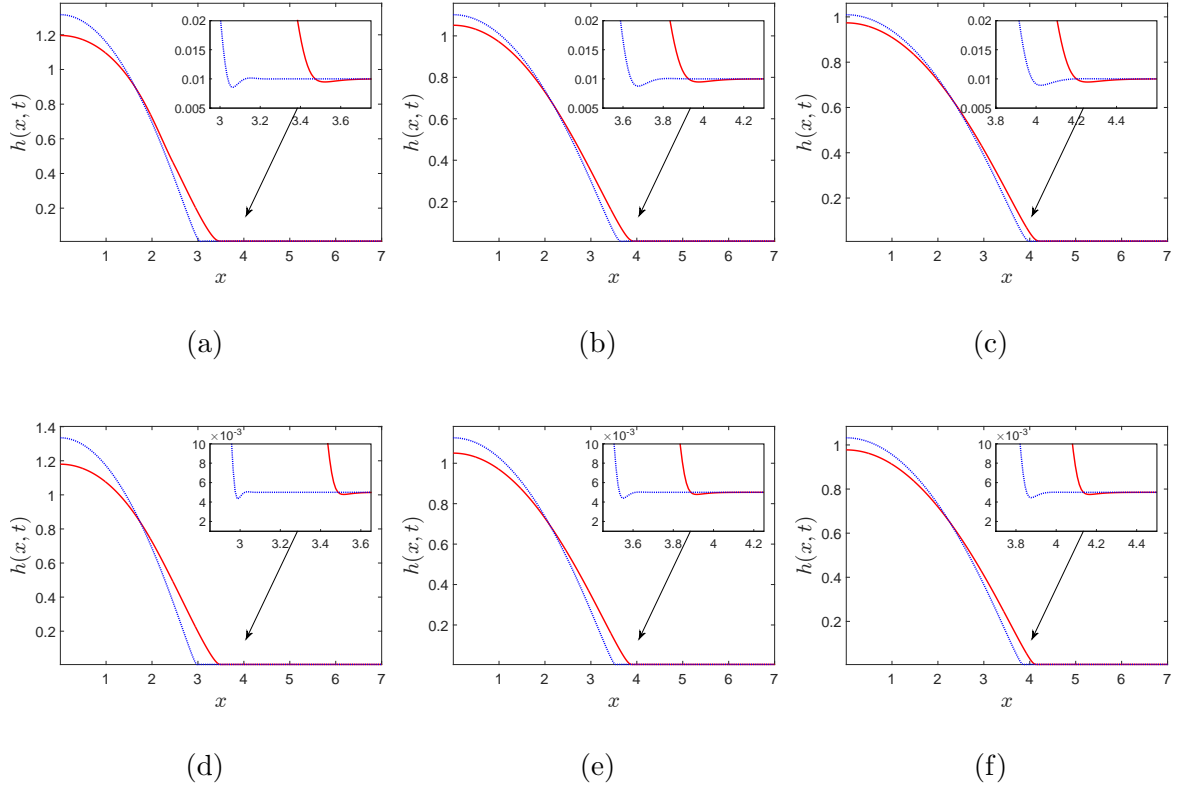
Figure 2.10 The spreading of a viscoelastic drop with $\lambda_1 = 15, \lambda_2 = 0.01$ (red solid curve) versus a Newtonian drop with $\lambda_1 = \lambda_2 = 0$ (blue dotted curve), at $t = 10, 50, 100$ from left to right. In (a)–(c) the equilibrium thickness $h_\star = 0.01$; in (d)–(f) $h_\star = 0.005$. The insets show a close-up of the contact line region.

Figure 2.10(a), we note that viscoelasticity influences predominantly the initial stage of the spreading. This behavior can be attributed to viscoelastic effects due to stretching of liquid around the contact line region in the direction of spreading. As the spreading velocity decreases, viscoelastic stresses relax in the contact line region, leading to the same spreading speed for both drops. In both cases, the drops relax towards the final configuration defined by θ_e (this regime of spreading is not shown in Figure 2.10). To shed more light on the origin of the difference in the spreading behavior, Figures 2.10(d)–2.10(f) use $h_\star = 0.005$. The consideration of thinner $h_\star$ is motivated by [72, 73], where it was shown, within the Oldroyd-B model, that elastic effects influence the behavior of the film ridge more remarkably when $h_\star$ is reduced.
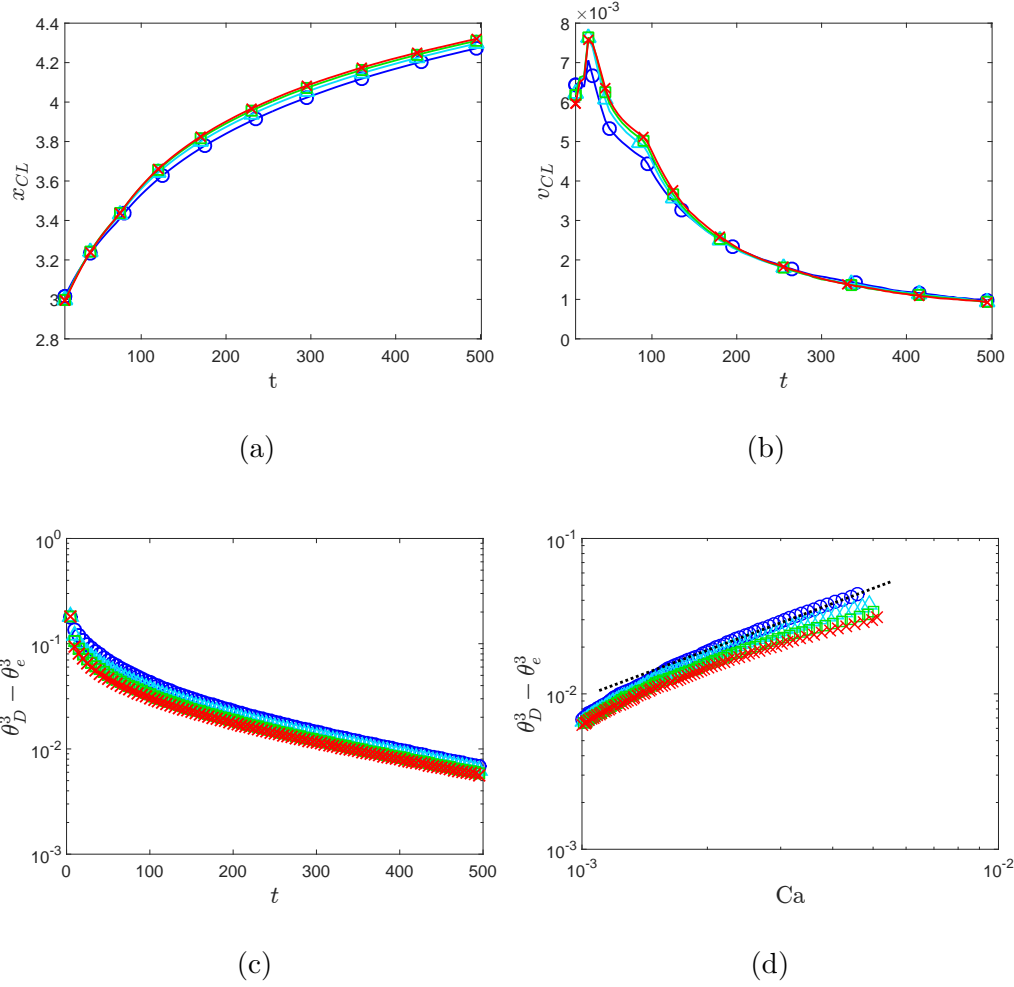
Figure 2.11 The spreading of a planar drop on a prewetted substrate with $h_\star = 0.005$, from an initial angle $\theta_i = 30°$ to an equilibrium configuration with $\theta_e = 15°$ for a viscous Newtonian drop, with $\lambda_1 = \lambda_2 = 0$ (blue circles), and viscoelastic drops, $\lambda_1 = 5$ (cyan triangles), 10 (green squares), and 15 (red crosses) when $\lambda_2 = 0.01$. (a) Contact line position, x_{CL}, versus time. (b) The velocity of the contact line, v_{CL}, versus time. (c) $\theta_D^3 - \theta_e^3$ versus time in a semilogarithmic scale. (d) $\theta_D^3 - \theta_e^3$ versus the capillary number Ca in a log-log plot. The dashed black line has a reference slope equal to one.

The comparison of Figure 2.10(d) and 2.10(a) shows that the difference between the Newtonian and the viscoelastic drop is indeed more significant for thinner $h_\star$. We attribute this difference to the dynamics of the interface at the contact line region: For the Newtonian drop, the interface of the prewetted film shows a "sagging" behavior, slowing down the spreading velocity. When decreasing $h_\star$, this oscillation is more

noticeable. For the viscoelastic drop, however, the prewetted film does not exhibit such pronounced behavior, as the interface at the contact line region is smoothed by viscoelasticity. A similar oscillatory behavior is demonstrated, both analytically [13] and experimentally [74], in the far-field region of dewetting viscoelastic fronts. Seemann et al. [74] also show that viscoelastic effects tend to stabilize the observed undulations, in agreement with our results. In addition, our simulations suggest that viscoelasticity enhances spreading, consistent with findings in [51, 73]. In particular, Spaid and Homsy [73] observe how the viscoelastic fluid interface tends to be stabilized primarily because of changes of transport of momentum in the spreading direction, and finite restoring forces that are present when a viscoelastic fluid is stretched. More recently, Izbassarov and Muradoglu [51] demonstrate that the enhancement of the spreading of viscoelastic drops is mainly due to the stretched polymer chains that exert an extensional stress, pushing the contact line, and thus increasing the spreading rate.

We next investigate the influence of the viscoelasticity on the dynamic advancing contact angle. In Figure 2.11, we consider three viscoelastic spreading drops with a fixed retardation time, $\lambda_2 = 0.01$, and three different relaxation times, $\lambda_1 = 5$ (cyan triangles), 10 (green squares), and 15 (red crosses), and compare them to the Newtonian drop with $\lambda_1 = \lambda_2 = 0$ (blue circles). All drops spread on a prewetted substrate with thickness $h_\star = 0.005$. In Figure 2.11(a), we show the front contact line, x_{CL}, determined as the x-coordinate of inflection point of $h(x, t)$. Figure 2.11(b) shows that viscoelastic drops initially move faster than the Newtonian counterpart. Eventually, both viscoelastic and Newtonian drops reach the same speed towards the equilibrium configuration. We also note that increasing λ_1 enhances the velocity of the contact line, v_{CL}. Figure 2.11(c) shows the difference of the cubes of the dynamic and equilibrium contact angles, $\theta_D^3 - \theta_e^3$, versus time in a semilogarithmic plot. As shown, the quantity $\theta_D^3 - \theta_e^3$ is smaller for viscoelastic drops with a higher

relaxation time λ_1, due to the fact that the viscoelastic drop contact line displaces faster from the initial configuration compared to the Newtonian one, as discussed above. Finally, Figure 2.11(d) shows $\theta_D^3 - \theta_e^3$ versus the capillary number $Ca = v_{CL}$ (given our choice for scales), both in logarithmic scales. The direct proportionality between these quantities is known as the Cox-Voinov law [52, 53], that we consider in the general form $\theta_D^3 - \theta_e^3 \propto Ca^\beta$ (consistent with [43]). In Figure 2.11(d), we show that this law holds for the Newtonian fluid, where the best linear fit of the data (denoted by blue circles) has unit slope (i.e., $\beta = 1$); while lower values of β are visible for the viscoelastic counterparts. These findings are consistent with recent experimental [46] and computational [50] results, showing that the viscoelasticity enhances contact line motion, and that there is a slight variation in the slope of the linear dependence on the capillary number in the Cox-Voinov law, due to viscoelasticity. Furthermore, we have verified (Figures not shown for brevity) that different values of the precursor film thickness do not significantly alter the dynamic contact angle, and hence the Cox-Voinov law results.

Receding drops　Similarly to the spreading case, we carry out investigations of the dynamic contact angle for receding drops. We use the same geometrical framework as the one for a spreading drop, but we impose $\theta_i = 15°$ and $\theta_e = 30°$. Figures 2.12(a)–(c) show the comparison of the evolution of two retracting drops at three selected times: a Newtonian drop with $\lambda_1 = \lambda_2 = 0$ (blue dotted curve), and a viscoelastic one with $\lambda_1 = 15, \lambda_2 = 0.01$ (red solid curve); for both simulations, we impose an equilibrium film thickness $h_\star = 0.005$. Again, the two drops exhibit discrepancy in their evolution. In Figure 2.12(a), at time $t = 100$, we see that the Newtonian drop has receded more than the viscoelastic one. This happens because, contrary to the spreading problem, the viscoelastic fluid interface initially shows more bending (visible in the inset of the Figure 2.12(a)), indicating that there is resistance to the force that drives the retraction of the drop. In Figure 2.12(b), at time $t = 350$, this oscillation in the
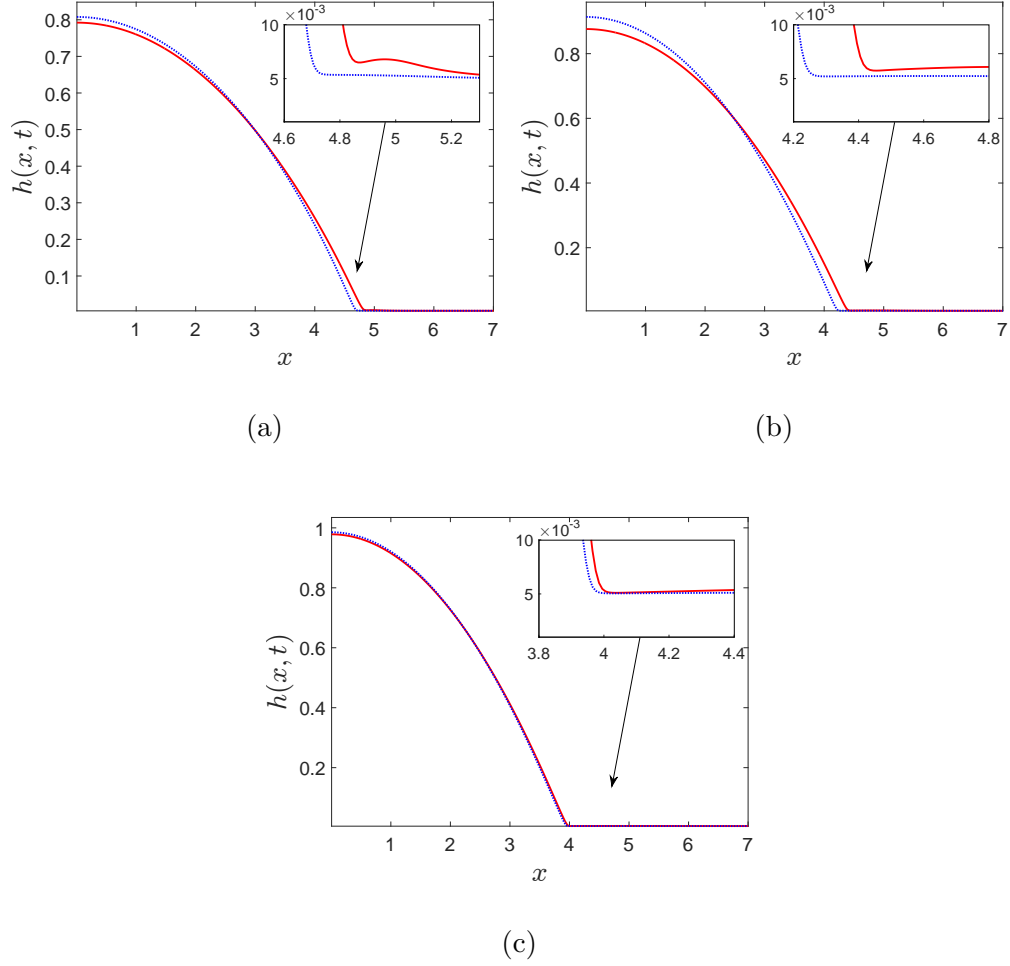
Figure 2.12 The retraction of a viscoelastic drop with $\lambda_1 = 15, \lambda_2 = 0.01$ (red solid curve) versus a Newtonian drop $\lambda_1 = \lambda_2 = 0$ (blue dotted curve), at $t = 100, 350, 1000$ from left to right; equilibrium film thickness $h_\star = 0.005$.

viscoelastic interface is flattened, and this allows for faster motion of the contact line for viscoelastic drop. As in the spreading case, eventually, both drops reach the same speed, and attain the same final configuration at time $t = 1000$, shown in Figure 2.12(c). The slower retraction of a viscoelastic drop is also investigated in [48], where it is demonstrated that this behavior is due to the elastic effects near the moving contact line.

Finally, we present the results of the dynamic contact angle for the receding drops. Figure 2.13(a) shows that the Newtonian drop with $\lambda_1 = \lambda_2 = 0$ (denoted by
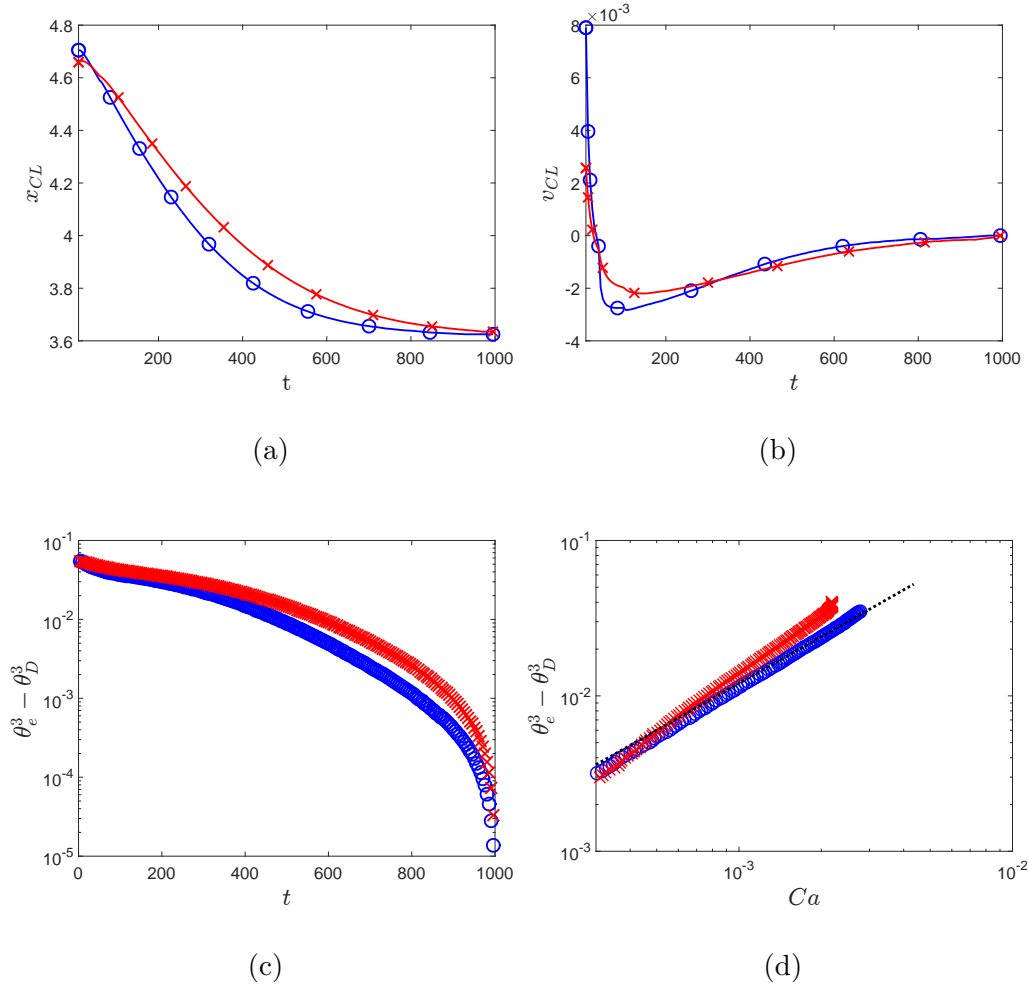
Figure 2.13 The retraction of a planar drop on a prewetted substrate with $h_\star = 0.005$, from an initial angle $\theta_i = 15°$ to an equilibrium configuration with $\theta_e = 30°$ for a viscoelastic drop with $\lambda_1 = 15, \lambda_2 = 0.01$ (red crosses), versus a Newtonian drop with $\lambda_1 = \lambda_2 = 0$ (blue circles). (a) The contact line position, x_{CL}, versus time. (b) The speed of the contact line, v_{CL}, versus time. (c) $\theta_e^3 - \theta_D^3$ versus time. (d) $\theta_e^3 - \theta_D^3$ versus the capillary number Ca. The dashed black line has a reference slope equal to one.

blue circles) recedes faster than the viscoelastic drop with $\lambda_1 = 15, \lambda_2 = 0.01$ (denoted by red crosses). Figure 2.13(b) shows the retraction velocities of the two drops as a function of time. The Newtonian drop initially recedes faster than the viscoelastic one, and eventually they reach the same speed towards the final configuration. Figure 2.13(c) shows $\theta_e^3 - \theta_D^3$ versus time, in a semilogarithmic plot. The quantity $\theta_e^3 - \theta_D^3$ is higher for the viscoelastic drop, since it retracts slower. Figure 2.13(d) shows

$\theta_e^3 - \theta_D^3$ versus Ca, both in logarithmic scales. Differently from the spreading case, the best linear fit of the receding viscoelastic data has a slope higher than the one corresponding to the Newtonian data ($\beta = 1$).

2.6 Conclusions

We summarize here our numerical investigation of two-dimensional thin viscoelastic films and drops on flat substrates, described in this chapter, that has provided the main contribution to our publication [30]. We numerically solve the nonlinear equation that governs the fluid interface of a dewetting thin film of viscoelastic fluid on a solid substrate. The governing equation is obtained as the long-wave approximation of the Navier-Stokes equations with the Jeffreys constitutive law describing the non-Newtonian nature of the viscoelastic fluid. The van der Waals interaction force drives the instabilities of the liquid interface and causes the film to break up, forming holes bounded by retracting rims. We investigate how physical parameters involved, such as the relaxation and retardation characteristic times of the viscoelastic fluid, and the slip coefficient, affect the dynamics and the final configuration of the fluid. In the linear regime, our results are in agreement with the linear stability analysis. Consistent with previous studies, we find that viscoelastic parameters and the slippage coefficient do not influence either the wavenumber corresponding to the maximum growth rate or the critical one, but influence the maximum growth rate. In particular, an increase of the relaxation time, λ_1, or the slip length, b, leads to an increase of the maximum growth rate. Conversely, increasing the retardation time, λ_2, leads to a decrease of maximum growth rate.

The simulations of the dewetting of thin viscoelastic films in the nonlinear regime reveal novel complex morphologies that depend on the viscoelasticity. The results show that for small values of λ_1, a single secondary droplet can be formed, while for large values, multiple secondary droplets can emerge. We note that the

emergence of these small length scales can be related to the relaxation time λ_1. In our work [30], we not only provide, for the first time, a study of these developing length scales, but also report on the migration and merging of the secondary droplets due to viscoelastic effects. Simulation results also show that the inclusion of λ_2 provides a numerical advantage by stabilizing the computations at high values of λ_1. In addition, the influence of the slip coefficient on the dynamics and final configurations is also addressed. Future work shall consider extension of these results to three spatial dimensions.

In the final part of this chapter, we investigate the dynamic contact angle of viscoelastic drops. Our numerical simulations show that the viscoelastic advancing front moves faster at early times, and that eventually it behaves as the Newtonian counterpart for large times. Our simulations suggest that the enhancement of the speed of the viscoelastic spreading drop is due to the smoothness of its interface in the prewetted region. The analysis of the dynamic contact angle also allows us to verify the Cox-Voinov law for the viscous Newtonian case; while we show small deviations from this law for viscoelastic drops. For receding viscoelastic drops, we show that the speed of the contact line is instead decreased, when compared to a Newtonian one. Again, we explain this behavior by the viscoelastic force at the contact line region resisting the receding motion of the contact line. Although our study is limited to the Jeffreys linear viscoelastic model, we hope that it will serve as a basis for further analysis of other viscoelastic models.

CHAPTER 3

THIN VISCOELASTIC FILMS ON INVERTED SUBSTRATES

3.1   Introduction

This chapter provides a natural extension of Chapter 2. In fact, it concerns the study of the interfacial dynamics of thin viscoelastic films subject to, not only the van der Waals interaction force, but also the gravitational force, in two spatial dimensions.

The instabilities of thin films down inclined planes have been widely studied for the case of viscous liquids (see, for instance, some of the first works [75, 76, 77, 78]). More recently, some industrial applications, such as the manufacturing of very thin (and possibly flexible) displays, have motivated similar investigations involving complex fluids, such as nematic liquid crystals [79], variable-viscosity fluids [80], or shear-thinning, non-Newtonian fluids [81]. However, to the best of our knowledge, a similar investigation that includes linear viscoelastic models is missing.

In this chapter, we outline the theoretical and numerical study concerning the interfacial flow of two-dimensional thin viscoelastic films under the effects of both the gravitational force and the van der Waals potential. We present here a novel derivation of the equation governing the dynamics of thin viscoelastic films of Jeffreys type flowing down an inclined plane, and present our numerical results in the particular case of an inverted plane. The goal is not only to investigate the effects of viscoelasticity on the interfacial flows of thin viscoelastic films laying on inverted planes, but also to analyze the competing effects of the different forces at play. In the same fashion as in Chapter 2, the linear stability analysis is performed to assess the effects of the different physical parameters involved on the dynamics governing the linear regime, and compare theoretical predictions of the early stage of the dynamics, with the numerical results obtained. The competing effects of the physical parameters

involved on the length and time scales of the instabilities are analyzed, in the linear and nonlinear regimes.

In the particular case in which regular or inverted planes are considered, we discover that, in the linear regime, the critical and most unstable wavenumbers are neither dependent on the viscoelastic parameters, nor on the slip length (similarly to our findings in Section 2.5), but only on the van der Waals interactions with the substrate and, in addition, the gravitational force. Moreover, we provide numerical simulations of the evolution of the interface in the nonlinear regime, for the particular case of inverted planes. In this regime, we find that the gravitational force affects the equilibrium configuration attained by the dewetted films, by suppressing the satellite droplets induced by viscoelasticity, that we described in Section 2.5, and forming a hump in the nominally dry central region.

3.2   Mathematical Formulation

We outline here the derivation of the governing equation for a viscoelastic fluid flowing down a plane, inclined at an angle α with respect to the positive x-axis, and subject to the van der Waals potential and weak slip regime with the substrate. For the reader's convenience, we repeat here the governing equations that were previously given in system (2.1)

$$\rho \left(\partial_t \mathbf{v} + \mathbf{v} \cdot \nabla \mathbf{v} \right) = -\nabla (p + \Pi) + \nabla \cdot \boldsymbol{\sigma} + \mathbf{F_b} \,, \tag{3.1a}$$

$$\nabla \cdot \mathbf{v} = 0 \,. \tag{3.1b}$$

We recall that, we consider the body force $\mathbf{F_b} = (\rho g \sin \alpha, -\rho g \cos \alpha)$, where, in this chapter, the gravitational acceleration constant is positive ($g > 0$) for the reference system depicted in Figure 3.1. Similarly to the setup in the previous chapter, this system of equations is subject to boundary conditions at the free surface, represented
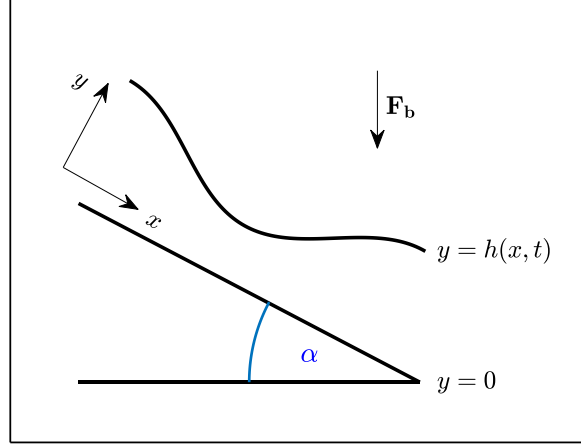
Figure 3.1 Schematic of the fluid interface on a plane inclined of an angle α.

parametrically by the function $f(x, y, t) = y - h(x, t) = 0$, and boundary conditions at the x-axis $(y = 0)$. The stress balance at the interface is the same as in equation (2.12) and we recall it here for the reader's convenience

$$(\boldsymbol{\sigma} - (p + \Pi)\mathbf{I}) \cdot \mathbf{n} = \gamma 2\kappa_m \mathbf{n} \,, \tag{3.2}$$

where $\mathbf{I}$ is the identity matrix, and the definitions of normal and tangent vectors to the interface, and of mean curvature remain the same as the ones given in equations (2.13) and (2.14). Similarly, we consider the same boundary conditions at the inclined solid substrate as in equation (2.15).

3.3   Thin Film Approximation

We nondimensionalize the problem in the same fashion as in Section 2.3, in which $\varepsilon \ll 1$ represents the small parameter for the asymptotic expansion. The incompressibility

condition, equation (3.1b), is invariant under rescalings, while the dimensionless forms of equation (3.1a), for the x and y component, respectively, are

$$\varepsilon^2 Re \frac{dv_1}{dt} = \varepsilon^2 \frac{\partial \sigma_{11}}{\partial x} + \frac{\partial \sigma_{21}}{\partial y} - \frac{\partial p}{\partial x} + \mathcal{S}, \tag{3.3a}$$

$$\varepsilon^4 Re \frac{dv_2}{dt} = \varepsilon^2 \left(\frac{\partial \sigma_{12}}{\partial x} + \frac{\partial \sigma_{22}}{\partial y} \right) - \frac{\partial p}{\partial y} - \mathcal{C}, \tag{3.3b}$$

where the definition of Reynolds number is given in Section 2.3, and we recall that it is assumed to be of order $1/\varepsilon$ or smaller. In equations (3.3) we have defined

$$\mathcal{S} = \mathcal{B} \sin \alpha \tag{3.4a}$$

$$\mathcal{C} = \mathcal{B} \cos \alpha \tag{3.4b}$$

with $\mathcal{B} = \rho g L^2 / \Gamma \equiv \rho g L^2 \varepsilon^3 / V \eta = O(1)$ the Bond number, a dimensionless quantity representing the importance of gravity relative to surface tension. The dimensionless components of the stress tensor given by the Jeffreys model in equations (2.20) remain invariant under the addition of gravitational effects.

As in Section 2.3, the kinematic boundary condition, equation (2.14), is invariant under rescaling, and the non-penetration condition and the Navier slip boundary condition for the velocity components parallel to the substrate, equation (2.15), in dimensionless form are given by equation (2.21). Now the leading-order terms in the governing equations (2.19a) and (2.19b), respectively, are

$$\frac{\partial \sigma_{21}}{\partial y} = \frac{\partial p}{\partial x} - \mathcal{S}, \tag{3.5a}$$

$$\frac{\partial p}{\partial y} = -\mathcal{C}. \tag{3.5b}$$

By integrating equation (3.5b) from y to $h(x,t)$, and using the leading-order term of the normal component of the stress balance at the free surface, equation (3.2), we obtain

$$p = -\frac{\partial^2 h}{\partial x^2} - \Pi(h) - \mathcal{C}(y - h)\,, \tag{3.6}$$

hence,

$$\frac{\partial p}{\partial x} = -\frac{\partial^3 h}{\partial x^3} - \Pi'(h)\frac{\partial h}{\partial x} + \mathcal{C}\frac{\partial h}{\partial x}\,. \tag{3.7}$$

We recall that the form of $\Pi(h)$ in equation (3.6) is given by equation (2.25), with all the quantities considered nondimensional. Moreover, integrating equation (3.5a) from y to $h(x,t)$, we obtain

$$\sigma_{21} = (y - h)\frac{\partial p}{\partial x} - (y - h)\mathcal{S}\,. \tag{3.8}$$

Noting that the stress tensor is symmetric, and substituting this form of σ_{21}, equation (3.8) into equation (2.20c), we obtain (up to the leading-order)

$$\frac{\partial p}{\partial x}(y - h) + \lambda_1\frac{\partial}{\partial t}\left(\frac{\partial p}{\partial x}(y - h) - \mathcal{S}(y - h)\right) = \frac{\partial v_1}{\partial y} + \lambda_2\frac{\partial}{\partial t}\left(\frac{\partial v_1}{\partial y}\right)\,. \tag{3.9}$$

Integrating equation (3.9) from 0 to $y = h(x,t)$ and using the corresponding boundary conditions at the substrate $y = 0$, we obtain

$$\left(1 + \lambda_2\frac{\partial}{\partial t}\right)\left(v_1 + bh\frac{\partial p}{\partial x} - bh\mathcal{S}\right) = \left(1 + \lambda_1\frac{\partial}{\partial t}\right)\left[\left(\frac{y^2}{2} - yh\right)\left(\frac{\partial p}{\partial x} - \mathcal{S}\right)\right]\,. \tag{3.10}$$

Integrating equation (3.10) again from $y = 0$ to $y = h(x,t)$ gives

$$\left(1 + \lambda_2 \frac{\partial}{\partial t}\right) \left(\int_0^{h(x,t)} v_1 \, dy + bh^2 \frac{\partial p}{\partial x} - bh^2 \mathcal{S}\right) -$$
$$\lambda_2 \frac{\partial h}{\partial t} \left(v_1(y = h(x,t)) + bh \frac{\partial p}{\partial x} - bh\mathcal{S}\right) =$$
$$-\left(\frac{h^3}{3} \frac{\partial p}{\partial x} + \lambda_1 h^2 \frac{\partial h}{\partial t}\right) \left(\frac{\partial p}{\partial x} - \mathcal{S}\right) . \tag{3.11}$$

Taking the spatial derivative of the latter equation and substituting it into the kinematic boundary condition (2.14), we obtain a long-wave approximation in terms of v_1 and $h(x,t)$

$$h_t + \lambda_2 \left[h_{tt} + \frac{\partial}{\partial x}(v_1(y = h(x,t))h_t)\right] = \frac{\partial}{\partial x}\left[(1 + \lambda_1 \partial_t)\left(\frac{h^3}{3} \frac{\partial p}{\partial x} - \frac{h^3}{3}\mathcal{S}\right) + \right.$$
$$\left. (1 + \lambda_2 \partial_t)\left(bh^2 \frac{\partial p}{\partial x} - bh^2 \mathcal{S}\right)\right] - \frac{\partial}{\partial x}\left\{\left[\lambda_1 \frac{h^2}{2}\left(\frac{\partial p}{\partial x} - \mathcal{S}\right) + \lambda_2 bh\left(\frac{\partial p}{\partial x} - \mathcal{S}\right)\right] h_t\right\} . $$
$$\tag{3.12}$$

To write this in a closed form relation for $h(x,t)$, we note that equation (3.10) can be written in a more compact form as a linear ordinary differential equation

$$v_1 + \lambda_2 \frac{\partial v_1}{\partial t} = -(1 + \lambda_2 \partial_t)\left(bh \frac{\partial p}{\partial x} - bh\mathcal{S}\right) + (1 + \lambda_1 \partial_t)\left[\left(\frac{y^2}{2} - hy\right)\left(\frac{\partial p}{\partial x} - \mathcal{S}\right)\right] . \tag{3.13}$$

One can simply solve this linear differential equation, obtaining

$$v_1 = \frac{1}{\lambda_2} \int_{-\infty}^t e^{-\frac{t-t'}{\lambda_2}} \tilde{f}(x,y,t') dt' , \tag{3.14}$$

with $\tilde{f}$ equal to the right-hand side of equation (3.13). Integration by parts can be performed to recast equation (3.14) at $y = h(x,t)$, and one finally obtains the following dimensionless equations

$$(1 + \lambda_2 \partial_t)h_t + (\lambda_2 - \lambda_1)\frac{\partial}{\partial x}\left[\left(\frac{h^2}{2}\widehat{Q} - h\widehat{R}\right)h_t\right] +$$
$$\frac{\partial}{\partial x}\left[(1 + \lambda_1 \partial_t)\frac{h^3}{3}\left(\frac{\partial^3 h}{\partial x^3} + \Pi'(h)\frac{\partial h}{\partial x} - \mathcal{C}\frac{\partial h}{\partial x} + \mathcal{S}\right) +\right.$$
$$\left.(1 + \lambda_2 \partial_t)bh^2\left(\frac{\partial^3 h}{\partial x^3} + \Pi'(h)\frac{\partial h}{\partial x} - \mathcal{C}\frac{\partial h}{\partial x} + \mathcal{S}\right)\right] = 0\,, \qquad (3.15)$$

where now $\widehat{Q} = \widehat{Q}(h)$ and $\widehat{R} = \widehat{R}(h)$ satisfy the ODEs:

$$(1 + \lambda_2 \partial_t)\widehat{Q} = \frac{\partial p}{\partial x} - \mathcal{S} \equiv \frac{\partial}{\partial x}\left(-\frac{\partial^2 h}{\partial x^2} - \Pi'(h) + \mathcal{C}h\right) - \mathcal{S}\,, \qquad (3.16a)$$

$$(1 + \lambda_2 \partial_t)\widehat{R} = h\left(\frac{\partial p}{\partial x} - \mathcal{S}\right) \equiv h\left[\frac{\partial}{\partial x}\left(-\frac{\partial^2 h}{\partial x^2} - \Pi'(h) + \mathcal{C}h\right) - \mathcal{S}\right]\,. \qquad (3.16b)$$

Here, we have used the form of $\partial p/\partial x$, up to leading order, defined in (3.7). We notice that for the case in which $\lambda_1 = \lambda_2$ (that corresponds to a Newtonian fluid), equations (3.15) and (3.16) reduce to the governing equation for thin viscous films on inclined planes, as outlined in [65, 68]. Equations (3.16) can be solved exactly by integrating factor

$$\widehat{Q} = \frac{1}{\lambda_2}\mathcal{L}[\partial_x p - \mathcal{S}]\,,$$
$$\widehat{R} = \frac{1}{\lambda_2}\mathcal{L}[h\left(\partial_x p - \mathcal{S}\right)]\,, \qquad (3.17)$$

with the operator $\mathcal{L}$ defined by

$$\mathcal{L}[\bar{g}] := \int_{-\infty}^{t} e^{-\frac{t-t'}{\lambda_2}}\bar{g}(x, y, z, t')dt'\,, \qquad (3.18)$$

where $\bar{g}$ equals the right-hand side of equations (3.16a) and (3.16b), respectively.

3.4   Numerical Methods

To conduct our spatial and temporal discretization, similarly to the recasting done in Section 2.4, equation (3.15) can be rearranged by swapping the mixed derivatives

$$\lambda_2 h_{tt} + \underbrace{\frac{\partial}{\partial x}\left[\left(\frac{h^3}{3} + bh^2\right)\left(\frac{\partial^3 h}{\partial x^3} + \Pi'(h)\frac{\partial h}{\partial x} - \mathcal{C}\frac{\partial h}{\partial x} + \mathcal{S}\right)\right]}_{\widehat{f}(h)} +$$

$$\underbrace{\left\{1 + (\lambda_2 - \lambda_1)\left[\frac{\partial}{\partial x}\left(\frac{h^2}{2}\widehat{Q} - h\widehat{R}\right)\right]\right\}}_{\widehat{g}(h)} h_t + \underbrace{\frac{\partial}{\partial t}\left(\frac{\partial h}{\partial x}\right)}_{l(h)} \underbrace{(\lambda_2 - \lambda_1)\left(\frac{h^2}{2}\widehat{Q} - h\widehat{R}\right)}_{\widehat{m}(h)} +$$

$$\lambda_1 \frac{\partial}{\partial t}\underbrace{\left[\frac{\partial}{\partial x}\left(\frac{h^3}{3}\left(\frac{\partial^3 h}{\partial x^3} + \Pi'(h)\frac{\partial h}{\partial x} - \mathcal{C}\frac{\partial h}{\partial x} + \mathcal{S}\right)\right)\right]}_{\widehat{p}(h)} +$$

$$\lambda_2 \frac{\partial}{\partial t}\underbrace{\left[\frac{\partial}{\partial x}\left(bh^2\left(\frac{\partial^3 h}{\partial x^3} + \Pi'(h)\frac{\partial h}{\partial x} - \mathcal{C}\frac{\partial h}{\partial x} + \mathcal{S}\right)\right)\right]}_{\widehat{q}(h)} = 0\,. \tag{3.19}$$

The only difference from equation (2.39) is provided by the extra terms, $-\mathcal{C}\partial h/\partial x + \mathcal{S}$, in the three blocks f, p, q, now called $\widehat{f}, \widehat{p}, \widehat{q}$, respectively. Moreover, the discrete versions of the equations (3.17) are now given by

$$\frac{\widehat{Q}_i^{n+1} - \widehat{Q}_i^n}{\Delta t} = -\frac{\widehat{Q}_i^n}{\lambda_2} - \frac{1}{\lambda_2}\left(\frac{\partial^3 h}{\partial x^3} + \Pi'(h)\frac{\partial h}{\partial x} - \mathcal{C}\frac{\partial h}{\partial x} + \mathcal{S}\right)_i^n, \tag{3.20a}$$

$$\frac{\widehat{R}_i^{n+1} - \widehat{R}_i^n}{\Delta t} = -\frac{\widehat{R}_i^n}{\lambda_2} - \frac{1}{\lambda_2}h_i^n\left(\frac{\partial^3 h}{\partial x^3} + \Pi'(h)\frac{\partial h}{\partial x} - \mathcal{C}\frac{\partial h}{\partial x} + \mathcal{S}\right)_i^n, \tag{3.20b}$$

that, we solve, in the same fashion as in Section 2.4, using the forward Euler method with initial conditions $\widehat{Q}_i^0 = 0$ and $\widehat{R}_i^0 = 0$, respectively.

We solve equations (3.19) and (3.20) for the particular case in which $\alpha = \pi$, with the same boundary and initial conditions outlined in Section 2.4, namely, a prescribed $h(x, 0)$, $h_t(x, 0) = 0$, and $\partial h/\partial x = \partial^3 h/\partial x^3 = 0$ at the endpoints of the domain.
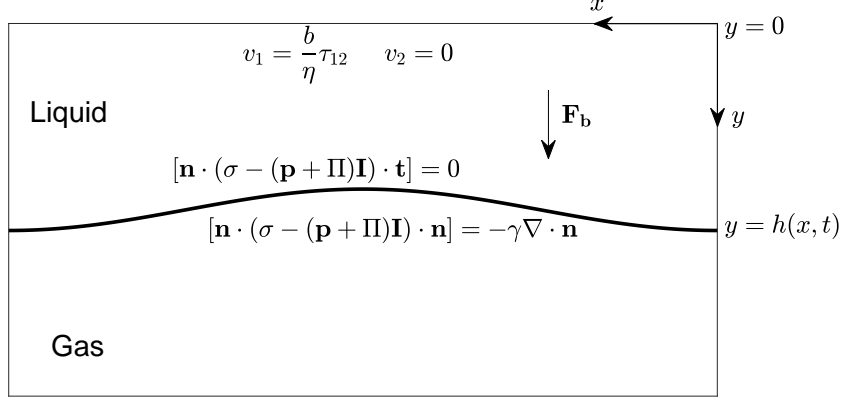
Figure 3.2 Schematic of a fluid interface for $\alpha = \pi$ (inverted plane).

3.5 Results and Discussion

3.5.1 Linear Stability Analysis

In this section, we report our results regarding the special case of an inverted plane, for which $\alpha = \pi$ (depicted in Figure 3.2). Similarly to the case analyzed in Section 2.5, we perturb a flat film of initial thickness h_0 by an oscillatory Fourier mode of amplitude δh_0 (such that $\delta \ll 1$), with wavenumber k and growth rate ω. Hence, we let $h(x,t) = h_0 + \delta h_0 e^{ikx+\omega t}$. Hence, performing the LSA on equations (3.15-3.16) leads to

$$\lambda_2 \omega^2 + \left[1 + (\mathcal{K}_\mathcal{C} + i\mathcal{S}k)\left(\lambda_1 \frac{h_0^3}{3} + \lambda_2 b h_0^2\right)\right]\omega + (\mathcal{K}_\mathcal{C} + i\mathcal{S}k)\left(\frac{h_0^3}{3} + b h_0^2\right) = 0\,, \quad (3.21)$$

where we have defined

$$\mathcal{K}_\mathcal{C} := k^4 - k^2(\Pi'(h_0) - \mathcal{C})\,. \tag{3.22}$$

Solving for ω in equation (3.21) we find two roots:

$$\omega_{1,2} = \frac{-\left[1 + (\mathcal{K_C} + i\mathcal{S}k)\left(\lambda_1\frac{h_0^3}{3} + \lambda_2 bh_0^2\right)\right] \pm \sqrt{\Delta_\omega}}{2\lambda_2}, \qquad (3.23)$$

where we have defined

$$\Delta_\omega := \left[1 + (\mathcal{K_C} + i\mathcal{S}k)\left(\lambda_1\frac{h_0^3}{3} + \lambda_2 bh_0^2\right)\right]^2 - 4\lambda_2(\mathcal{K_C} + i\mathcal{S}k)\left(\frac{h_0^3}{3} + bh_0^2\right). \qquad (3.24)$$

Considering only the real part of the two roots, we obtain

$$Re\{\omega_{1,2}\} = \frac{-\left[1 + \mathcal{K_C}\left(\lambda_1\frac{h_0^3}{3} + \lambda_2 bh_0^2\right)\right] \pm \sqrt{Re\{\Delta_\omega\}}}{2\lambda_2}, \qquad (3.25)$$

with

$$Re\{\Delta_\omega\} := \left[1 + \mathcal{K_C}\left(\lambda_1\frac{h_0^3}{3} + \lambda_2 bh_0^2\right)\right]^2 - 4\lambda_2\mathcal{K_C}\left(\frac{h_0^3}{3} + bh_0^2\right). \qquad (3.26)$$

This dispersion relation leads to two roots, namely $Re\{\omega_1\}$ and $Re\{\omega_2\}$, one of which, always negative (stable), say $Re\{\omega_2\}$, and the other one with varying sign (unstable), say $Re\{\omega_1\}$. The critical wavenumber now satisfies the relationship $k_c^2 = \Pi'(h_0) - \mathcal{C}$. Hence, we note that the gravitational term affects the critical wavenumber, and therefore, the length scales of instability. Moreover, we observe that the wavenumber of maximum growth, as for the case without gravity, satisfies the relationship $k_m = k_c/\sqrt{2}$.

3.5.2 Dewetting of Thin Viscoelastic Films on Inverted Substrates

We outline here the numerical results for a dewetting thin film under the influence of the van der Waals interaction and gravitational forces. As anticipated in the previous
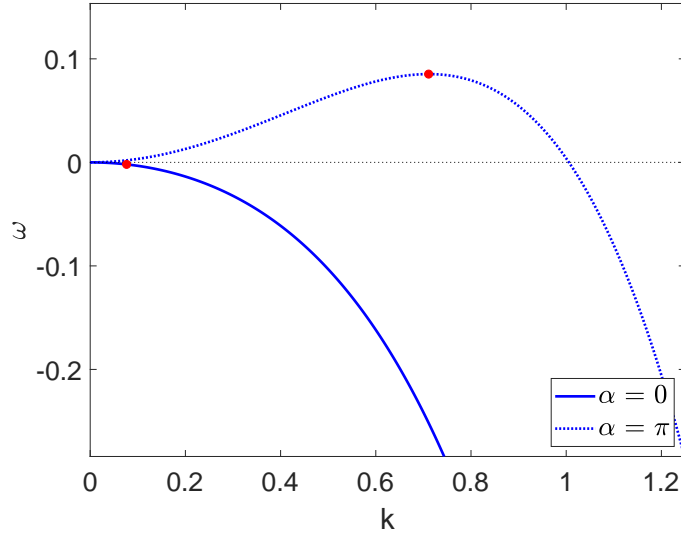
Figure 3.3 The comparison of the computed growth rate (red circles) with the prediction of the LSA, for $h_0 = 1$, $h_\star = 0.01$, $b = 0$, $\lambda_1 = \lambda_2 = 0$, and $\alpha = \pi$ (blue dotted line) and $\alpha = 0$ (blue solid line).

subsection, we consider the particular case in which $\alpha = \pi$ (unless stated otherwise), that is, for films that hang on an inverted plane. As described in Section 2.5, we perturb the initially flat fluid interface of thickness h_0, with $k = k_m$ and $\delta = 0.01$, and we choose the domain size to be equal to the wavelength of maximum growth, that is, $\Lambda = 2\pi/k_m$.

To isolate the effects of the gravitational force, we start by analyzing the behavior of dewetting films for the particular case of the absence of van der Waals potential with the substrate. In Figure 3.3, we present the comparison of the computed growth rates (red circles) with the theoretical values predicted by the dispersion relation, given by equation (3.26), for $h_0 = 1$, $h_\star = 0.01$, $b = 0$, $\lambda_1 = \lambda_1 = 0$, and $\alpha = \pi$ (blue dotted line) and $\alpha = 0$ (blue solid line). We remark that in this case, the only driving force for the instability is gravity. In fact, in the absence of the attraction/repulsion force with the substrate, and for $\alpha = 0$, we notice that there is no instability, and the growth rate is negative for all wavenumbers.
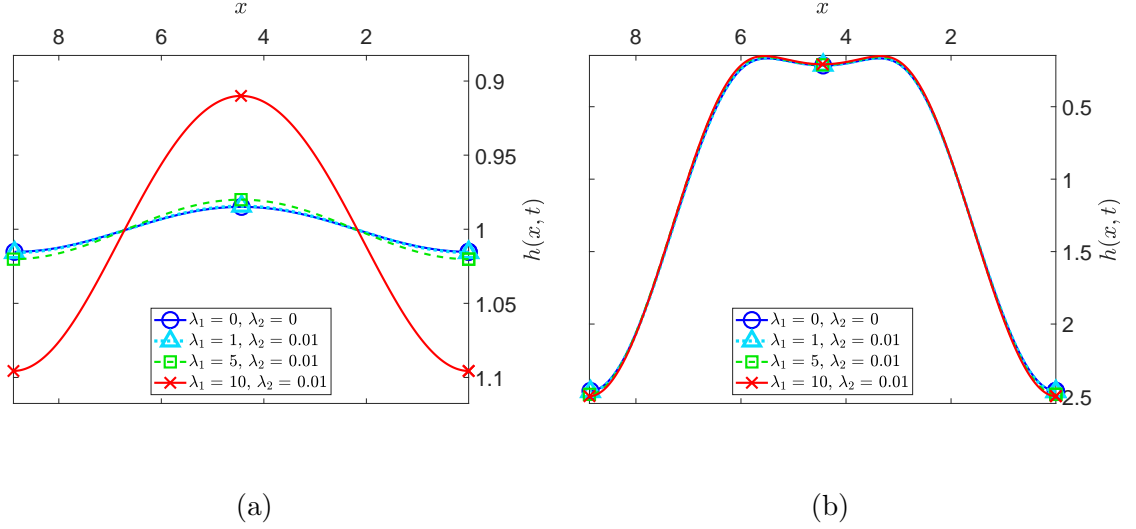
Figure 3.4 Evolution of different viscoelastic films, in the absence of the van der Waals potential with the substrate, for different values of λ_1 and $\lambda_2 : \lambda_1 = \lambda_2 = 0$ (blue solid curve with circles), $\lambda_2 = 0.01$ and $\lambda_1 = 1$ (cyan dotted curve with triangles), 5 (green dashed curve with squares), 10 (red solid curve with crosses); in (a) at time $t = 5$ and in (b) at time $t = 100$.

Next, in Figure 3.4, we investigate the dynamics of thin viscoelastic films, in the absence of van der Waals potential with the inverted substrate (i.e., $\alpha = \pi$). We compare the evolution of a Newtonian film, with $\lambda_1 = \lambda_2 = 0$ (blue solid curve with circles), with the one of viscoelastic films, with $\lambda_2 = 0.01$ and $\lambda_1 = 1$ (cyan dotted curve with triangles), 5 (green dashed curve with squares), 10 (red solid curve with crosses); in 3.4(a) at time $t = 5$, in 3.4(b) at time $t = 100$. Although in this case there is no van der Waals potential with the substrate, we can see that, similar to the cases analyzed in Section 2.5, in which the instability was solely driven by the van der Waals attraction/repulsion force, the viscoelastic film with highest relaxation time exhibits the fastest dynamics of dewetting. Eventually, all viscoelastic films reach the equilibrium configuration. However, the comparison of the final configurations attained with respect to the ones reached in the case of $\alpha = 0$ (see Figure 2.6) is remarkable. In fact, now the gravitational force has the effect of suppressing the satellite droplets, and forming a hump in the central region of dewetting. We also

notice that this nominally dry region is narrower compared to the one developed in the dewetting films for $\alpha = 0$.

(a)   (b)
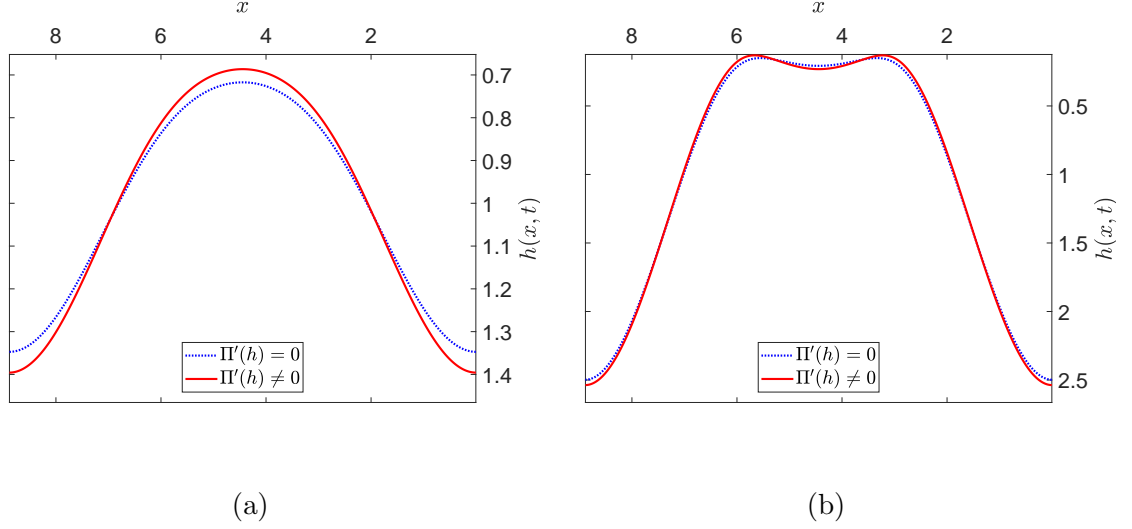
Figure 3.5 Evolution in the in absence (blue dotted curve) or presence (red solid curve) of the van der Waals potential with the inverted substrate for a viscoelastic film with $\lambda_1 = 10$ and $\lambda_2 = 0.01$, in (a) at time $t = 10$ and in (b) at time $t = 100$.

Commonly, only the isolated effects of the gravitational force or the van der Waals potential are analyzed. However, for liquid films of micro scale, the crossover region, where the effects of the two forces are comparable, can be considered. Hence, in Figure 3.5, we investigate the competing effects of the van der Waals potential and the gravitational force on the dynamics of dewetting films on an inverted plane. We compare the evolutions of two dewetting viscoelastic films, with $\lambda_1 = 10$ and $\lambda_2 = 0.01$, in 3.5(a) at time $t = 10$ and in 3.5(b) at time $t = 100$, in the absence (blue dotted curve) or presence (red solid curve) of the van der Waals potential with the inverted substrate. We can see that the film that is driven by both the gravitational force and the van der Waals attraction force exhibits a faster dynamics. Moreover, we notice that the equilibrium configuration attained by this film shows slightly lower minimum values of the interface function, manifesting the attraction toward the substrate due to the van der Waals potential.

3.6   Conclusions

We summarize here our numerical investigation described in this chapter. We derive a novel long-wave governing equation for the interfacial flow of two-dimensional thin viscoelastic films under the effects of the gravitational force and the van der Waals potential, in which the stresses are described by the Jeffreys model. The instability of the liquid interface that causes the film to break up and retracts with rims is caused by the competing effects of both forces. We carry out the linear stability analysis, that, as in the case with absence of gravity, shows that the viscoelastic parameters and the slippage coefficient do not influence either the wavenumber corresponding to the maximum growth rate or the critical one. However, the length scales of instabilities are affected by the gravitational contribution. Again, our numerical results of the computed growth rates in the linear regime are in agreement with the theoretical prediction provided by the linear stability analysis.

We simulate the behavior of dewetting viscoelastic films in the particular case in which they are attached to an inverted plane (i.e., for $\alpha = \pi$). To isolate the effects of the gravitational force, we begin by analyzing dewetting films in the absence of the van der Waals potential with the inverted substrate. The results for the nonlinear regime show that, at parity of viscoelastic and slippage parameters, gravity suppresses the satellite droplets that were found in absence of gravity and described in Section 2.5. Moreover, the gravitational force affects the equilibrium configuration of the dewetted films by forming a hump in the nominally dry central region, and narrowing the hole in the interface.

Finally, to investigate the competing effects of the gravitational and attraction/repulsion forces, we compare the evolution of two viscoelastic films dewetting an inverted substrate, in the absence or presence of the van der Waals potential. We find that the dewetting film whose evolution is driven by both the gravitational

force and the disjoining pressure exhibits a faster dynamics, and that the equilibrium configuration of its interface is slightly closer (being more attracted) to the substrate.

Future work shall consider the extension of this investigation in which planes inclined of arbitrary angles α, such that $\alpha \neq 0, \pi$, are considered. This would require the implementation of boundary conditions different from the ones described in Section 3.4. In fact, the no-flux boundary condition employed in our investigation is not suitable for the case of an inclined plane, as one should maintain a constant influx at the inlet, as in [68]. Similarly, for arbitrary values of α, the form of the perturbation employed for the linear stability analysis should present a wave-like mode [65, 68], rather than an oscillatory one. Furthermore, extensions of this investigation in three spatial dimensions would allow to describe and capture the fingering instabilities, that are known to arise in the direction transversal to the flow [65, 82].

FREE-BOUNDARY FLOW OF VISCOELASTIC MEMBRANES

4.1   Introduction

In this chapter, we present our numerical simulations of the dynamics of sheets of viscoelastic fluids, not necessarily deposited on a substrate, in three spatial dimensions. The majority of the studies in the literature of membrane theory of shells, focuses on the statics of load-carrying elastic shells that hold an equilibrium state (see, for instance, [37, 83, 84, 85, 86]). However, in this investigation we are interested in the transient analysis of the dynamics, described by the conservation of momentum equation, as outlined by Taylor et al. in [38], for the case of nonlinearly elastic membranes. Our goal is to expand the analysis conducted by Taylor et al. to include Newtonian and non-Newtonian membranes. For the non-Newtonian membranes we characterize the stresses by the Maxwell model [9]. We use this infinitesimal strain model within the general framework developed by Taylor et al. in [38] for finite strain theory, with the aim of expanding our analysis in future works, by including nonlinearities and corotational effects.

The majority of the previous studies on viscoelastic membranes focus on the rheological responses of the material to deformations (see, e.g., [34, 87, 88]), but only a few works investigate the dynamics of such membranes. For instance, Levine and MacKintosh [33], couple the dynamics of the viscoelastic membrane to the hydrodynamics of the surrounding viscous phase. Moreover, among the numerous studies on the rheology of viscoelastic membranes, Lubarda and Marzani [35] use the Kelvin-Voigt type of constitutive model, that is more suitable to describe viscoelastic solids [55], and Crawford and Earnshaw [89] use the Maxwell model, more suitable for the description of viscoelastic liquids [11], to identify the relaxation time of bilayer lipid membranes. However, to the best of our knowledge, a numerical investigation

solving for the equation of motion describing the hydrodynamics of the free-boundary flow of thin viscoelastic membranes of Maxwell type is lacking. The aim of this work is therefore to provide a general numerical framework for the simulations of thin viscoelastic membranes, and to analyze the role of viscoelasticity on their dynamics arising in different settings or engineering processes, such as the shearing flow [11] or the extensional flow in redrawing processes [90, 91].

The governing equation describes the conservation of linear momentum. To the typical steady formulation in which the balance of forces is considered, we retain the inertial term so we may consider transient analyses [92, 93]. The incompressibility condition that typically serves as a constraint on the vector velocity field in the equations describing the fluid dynamics [94] is replaced in this work via the use of a *penalty method* [95, 96]. This method, first introduced by Courant [97] for solutions of problems of equilibrium and vibrations, obtained by the calculus of variations, has been subsequently used to approximate solutions of the Navier-Stokes equations (see, for instance, [98] and the references therein). In the context of solutions of fluid flows, it relaxes the incompressibility condition allowing for a small perturbation of the volume change, which approximates the near incompressibility of the fluid. We propose a formulation of the penalty function as a direct proportionality on the rate of change of the volumetric strain, in which the constant of proportionality depends on the viscosity of the fluid.

In this numerical investigation, we use the finite element method for the spatial discretization of the slender geometry describing the membranes, and implicit schemes to discretize the time variations in the governing and constitutive equations. Finite element analyses of linearly elastic shells or membranes, in which the fluid domain is characterized by a surface, constitute a computational advantage relative to volumetric analyses and are vastly used in the Continuum Mechanics literature (see, e.g., [38, 92, 99, 100]). However, to the best of our knowledge, none of the existing analyses

included viscoelastic stresses of Maxwell type that can be adapted to Fluid Mechanics problems. We approximate the membrane with a mesh, constituted of linear 3-node triangles embedded in a three-dimensional global coordinate system (i.e., elements with nine degrees of freedom with respect to the global coordinates), and obtain the stress state on the surface of the membrane in terms of the nodal displacements. The spatial discretization formulation adopted closely follows the one by Taylor et al. [38], however, the novel aspects are the inclusion of viscoelasticity in the constitutive model, and the corresponding derivation of the material Jacobian (stiffness) tensor.

4.2   Mathematical Formulation

We consider a nearly incompressible viscoelastic liquid membrane with constant density ρ, surrounded by a passive gas with constant pressure. The equation describing the balance of linear momentum is

$$\text{div}(\boldsymbol{\sigma}) + \mathbf{F_b} = \rho \ddot{\mathbf{u}}, \qquad \text{in } \Omega \,, \tag{4.1}$$

where $\mathbf{u} = (u_1(x_1, x_2, x_3, t), u_2(x_1, x_2, x_3, t), u_3(x_1, x_2, x_3, t))$ represents the vector displacement field in a global coordinate system, $\ddot{\mathbf{u}} = d^2\mathbf{u}/dt^2$ in a Lagrangian formulation, $\mathbf{F_b}$ is the vector of the body force (such as gravity), $\text{div}(\boldsymbol{\sigma}) = \nabla \cdot \boldsymbol{\sigma}$, with $\boldsymbol{\sigma}$ the Cauchy symmetric stress tensor (suitable for small deformations [101]), and Ω is the two-dimensional surface embedded in $\mathbb{R}^3$. In what follows, we outline the weak and discrete versions of equation (4.1), leaving the detailed derivation for the interested reader in Appendix A.

We discretize the domain Ω with finite elements, in which each element represents a triangular membrane, uniquely described by its three vertices (nodes) in $\mathbb{R}^3$ (see Figure 4.1). By considering a global Cartesian coordinate system, we denote by upper case $\mathbf{X}$ the reference (undeformed state) configuration coordinates, and by lower case
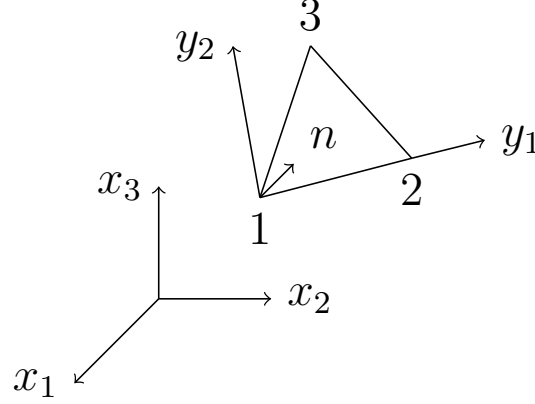
Figure 4.1 The surface coordinate system on a triangular element in the deformed configuration.

$\mathbf{x}$ the current (deformed state) ones. We denote the nodal values of the reference coordinates, current coordinates and displacement vector, respectively, by the use of superscripts, i.e $\widetilde{\mathbf{X}}^{\alpha}$, $\widetilde{\mathbf{x}}^{\alpha}$, and define the nodal displacement field as $\widetilde{\mathbf{u}}^{\alpha} = \widetilde{\mathbf{x}}^{\alpha} - \widetilde{\mathbf{X}}^{\alpha}$, with $\alpha = 1, 2, 3$ for each node. By using the virtual displacement field, $\delta\mathbf{u}$, we apply the virtual work formulation [38, 92], and obtain the volumetric contribution of the weak form of equation (4.1) as

$$\delta\Pi = \int_{\Omega^{(e)}} \delta\mathbf{u}^T \rho\ddot{\mathbf{u}} \, dV - \int_{\Omega^{(e)}} \delta\boldsymbol{\epsilon}^T \boldsymbol{\sigma} \, dV - \int_{\Omega^{(e)}} \delta\mathbf{u}^T \mathbf{F_b} \, dV = 0 \,, \qquad (4.2)$$

where $[\cdot]^T$ represents the matrix transpose operator, $\boldsymbol{\epsilon}$ the symmetric strain tensor, and $\Omega^{(e)}$ the domain of the element e. For the case of membranes of constant thickness h, we express an infinitesimal volume element as $dV = h \, dA$. Following the displacement-based finite element formulation provided in [38] for the spatial derivatives, we can write the spatially discrete version of the volume contribution terms (i.e., without the traction term) of equation (4.2), for each element, in vector form, as

$$
\mathbf{M}^{(e)} \begin{bmatrix} \ddot{\tilde{\mathbf{u}}}^1 \\ \ddot{\tilde{\mathbf{u}}}^2 \\ \ddot{\tilde{\mathbf{u}}}^3 \end{bmatrix} - hA^{(e)}\mathbf{B}^{(e)T} \begin{bmatrix} \sigma_{11} \\ \sigma_{22} \\ \sigma_{12} \end{bmatrix} - \begin{bmatrix} \widetilde{\mathbf{F}}_{\mathbf{b}}^1 \\ \widetilde{\mathbf{F}}_{\mathbf{b}}^2 \\ \widetilde{\mathbf{F}}_{\mathbf{b}}^3 \end{bmatrix} = \mathbf{0} \,, \tag{4.3}
$$

where we have used Voigt notation [92] for the Cauchy symmetric stress tensor in vector form for two-dimensional problems, defined by

$$
\boldsymbol{\sigma} = \begin{bmatrix} \sigma_{11} \\ \sigma_{22} \\ \sigma_{12} \end{bmatrix} .
$$

In equation (4.3), $A^{(e)}$ represents the area of each triangular element in the reference configuration, the vector $\widetilde{\mathbf{F}}_{\mathbf{b}} = (\widetilde{\mathbf{F}}_{\mathbf{b}}^1, \widetilde{\mathbf{F}}_{\mathbf{b}}^2, \widetilde{\mathbf{F}}_{\mathbf{b}}^3)$ represents the nodal body force, $\mathbf{M}^{(e)}$ is the element mass matrix, and $\mathbf{B}^{(e)T}\boldsymbol{\sigma}$ represents the divergence of the stress tensor on each element. In each triangle, we consider that both the strain and the stress tensors are constant. The interested reader can find the details of the derivation of each term in Appendix A. Our goal is to solve equation (4.3) for the nodal displacement field. We note that the nodal displacement vectors, $\tilde{\mathbf{u}}^\alpha$ ($\alpha = 1, 2, 3$), as well as the nodal force vectors, $\widetilde{\mathbf{F}}_{\mathbf{b}}^\alpha$ ($\alpha = 1, 2, 3$), represent three-dimensional vectors for each node, in the global coordinates. Hence, in components, we will solve for nine scalar equations, even though the strain and the stress tensors only account for the in-plane displacements.

4.3 Constitutive Models

To describe the material response to deformations, we need to express a constitutive law that relates the stress tensor and the strain and/or strain rate tensors. We consider a small deformation strain, within the general framework presented by Taylor et al. [38]

that allows nonlinearities due to large deformations (derived in Appendix A). For membrane problems, the in-plane magnitudes of the stress are dominant relative to the out-of-plane ones, leading to the conditions on the stress tensor components $\sigma_{13} = \sigma_{23} = \sigma_{33} = 0$. In two spatial dimensions, the *deviatoric* stress is defined, in tensor form, as

$$\sigma'_{ij} = \sigma_{ij} - \frac{1}{2}\sigma_{kk}\delta_{ij}\,, \tag{4.4}$$

where δ_{ij} is the Kronecker delta $(i,j = 1,2)$, and σ_{kk} is the trace of the stress tensor in indicial notation, i.e., $\sigma_{kk} = \sigma_{11} + \sigma_{22}$. In infinitesimal strain theory [92], the linear (small deformation) strain is given, in tensor form, by $\epsilon_{ij} = (\partial u_i/\partial x_j + \partial u_j/\partial x_i)/2$. In two dimensions, the trace of the strain tensor, also called the volumetric strain, is denoted by $\epsilon_{vol} = \epsilon_{kk} = \epsilon_{11} + \epsilon_{22}$. We call hydrostatic strain the mean of the normal strains, that is, $\epsilon_{hyd} = \epsilon_{kk}/2$. With this definition, we can also define the deviatoric strain, ϵ'_{ij}, satisfying

$$\epsilon'_{ij} = \epsilon_{ij} - \frac{1}{2}\epsilon_{kk}\delta_{ij}\,. \tag{4.5}$$

An important material parameter related to the response to (uniform) hydrostatic pressure in linear elasticity of isotropic media is the bulk modulus, K, and it is related to other material parameters such as ν, the Poisson's ratio, and Y, the Young's modulus, via the relationship $\nu = 1/2 - Y/6K$ [92]. We notice that for $K \gg Y$, meaning in the limiting case in which $K \to \infty$ (i.e., for $\nu \to 1/2$), we approach the incompressible limit. However, for nearly incompressible materials, a *penalty function* [95] that allows for small perturbations to the trace of the strain, representing the volumetric change, is given by

$$\epsilon_{kk} + p_{hyd}/K = 0 \, . \tag{4.6}$$

Hence, we find an expression for the hydrostatic pressure in terms of the volume variation, given by

$$p_{hyd} = -K\epsilon_{kk} \, , \tag{4.7}$$

We observe that for the limiting case of an incompressible material, i.e., with $K \to \infty$, equation (4.6) leads to the divergence-free condition on the displacement field, $\text{div}(\mathbf{u}) = 0$.

In this work, we expand the condition given by equation (4.6) to account for the hydrodynamic pressure in liquids, denoted by p. In constitutive models describing liquids, the stress response is directly proportional not to the strain, but to the rate of change of the strain, namely $\dot{\boldsymbol{\epsilon}}$. Accordingly, the consideration of a penalty method for liquids needs to take into account the strain rate [96]. We introduce a penalty formulation for the variation of the volume of nearly incompressible liquids

$$\dot{\epsilon}_{kk} + p/\widehat{K} = 0 \, , \tag{4.8}$$

for which the pressure in the liquid is then given in terms of the trace of the strain rate by

$$p = -\widehat{K}\dot{\epsilon}_{kk} \, , \tag{4.9}$$

with the penalty constant, $\widehat{K}$, such that

$$\widehat{K} \gg \eta \,, \tag{4.10}$$

where η represents the shear viscosity coefficient. We start our constitutive analysis by introducing the Newtonian constitutive model for viscous liquids, given by

$$\sigma_{ij} = 2\eta\dot{\epsilon}'_{ij} + \widehat{K}\dot{\epsilon}_{kk}\delta_{ij} \,. \tag{4.11}$$

Next, we include in our analysis viscoelastic fluids. Different linear viscoelastic constitutive models of interest can be expressed in linear differential form [11, 55, 56]. The Maxwell constitutive model for viscoelastic liquids is given by

$$\sigma_{ij} + \lambda_1\partial_t\sigma'_{ij} = 2\eta\dot{\epsilon}'_{ij} + \widehat{K}\dot{\epsilon}_{kk}\delta_{ij} \,, \tag{4.12}$$

where λ_1 is the relaxation time constant, such that $\lambda_1 = 2\eta/G$, with G the shear modulus [11]. We notice that when $\lambda_1 = 0$ we recover the Newtonian fluid constitutive law in equation (4.11). When $\lambda_1 > 0$, it determines the rate at which the stress relaxes (i.e decays) for constant strain. Maxwell model can interpolate between a linearly viscous and elastic behavior. In fact, when the stress applied has a fast time variation, the left hand side of equation (4.12) is dominated by the time derivative, and, upon time integration, the constitutive law for linearly elastic solids is recovered [11].

4.3.1   Time Discretization

The time interval $t \in [0, T]$ is discretized by n equal steps, with $n = 0, 1, \ldots$, and Δt is the temporal step size considered. At each spatial material point, we denote the stress at the previously converged time step by $\boldsymbol{\sigma}^n$, and at the current time step by $\boldsymbol{\sigma}^{n+1}$. We define the rate of change of the strain tensor with a finite difference

$\dot{\boldsymbol{\epsilon}}^{n+1} = (\boldsymbol{\epsilon}^{n+1} - \boldsymbol{\epsilon}^n)/\Delta t$, and similarly for the stress tensor. We consider initial conditions on both the strain and the stress to be $\boldsymbol{\epsilon}^0 = \boldsymbol{\sigma}^0 = \mathbf{0}$. We can hence write the discrete form of equation (4.11), in indicial form, as

$$\sigma_{ij}^{n+1} = \frac{2\eta}{\Delta t} \left\{ \left(\epsilon_{ij} - \frac{1}{2}\epsilon_{kk}\delta_{ij} \right)^{n+1} - \left(\epsilon_{ij} - \frac{1}{2}\epsilon_{kk}\delta_{ij} \right)^n \right\} + \frac{\widehat{K}}{\Delta t} \left\{ \epsilon_{kk}^{n+1}\delta_{ij} - \epsilon_{kk}^n\delta_{ij} \right\} , \tag{4.13}$$

and in vector form as

$$
\begin{bmatrix} \sigma_{11} \\ \sigma_{22} \\ \sigma_{12} \end{bmatrix}^{n+1} = \frac{2\eta}{\Delta t} \left\{ \begin{bmatrix} \frac{1}{2}\epsilon_{11} - \frac{1}{2}\epsilon_{22} \\ -\frac{1}{2}\epsilon_{11} + \frac{1}{2}\epsilon_{22} \\ \gamma_{12} \end{bmatrix}^{n+1} - \begin{bmatrix} \frac{1}{2}\epsilon_{11} - \frac{1}{2}\epsilon_{22} \\ -\frac{1}{2}\epsilon_{11} + \frac{1}{2}\epsilon_{22} \\ \gamma_{12} \end{bmatrix}^n \right\} +
$$
$$
\frac{\widehat{K}}{\Delta t} \left\{ \begin{bmatrix} \epsilon_{11} + \epsilon_{22} \\ \epsilon_{11} + \epsilon_{22} \\ 0 \end{bmatrix}^{n+1} - \begin{bmatrix} \epsilon_{11} + \epsilon_{22} \\ \epsilon_{11} + \epsilon_{22} \\ 0 \end{bmatrix}^n \right\} , \tag{4.14}
$$

where we have used the notation $\gamma_{12} = 2\epsilon_{12}$, for which in vector form shear strain components are twice that given in tensor form [92]. We consider the algorithmic consistent Jacobian (or stiffness) fourth order tensor to be defined for the case of Newtonian fluids as

$$\mathbb{C}_{ijlm} = \frac{\partial \sigma_{ij}^{n+1}}{\partial \epsilon_{lm}^{n+1}} = \eta(\delta_{il}\delta_{jm} + \delta_{im}\delta_{jl}) - \eta\delta_{ij}\delta_{lm} + \widehat{K}\delta_{ij}\delta_{lm} . \tag{4.15}$$

This way, we can write equation (4.11) in matrix form as a linear relation between the stress tensor and the strain rate tensor with a constant coefficient matrix, $\mathbf{D}_v$. We shall refer to $\mathbf{D}_v$ as the *viscosity matrix of moduli*, analogously to the elasticity matrix of moduli [92], and write

$$\boldsymbol{\sigma}^{n+1} = \mathbf{D}_v \dot{\boldsymbol{\epsilon}}'^{n+1} , \tag{4.16}$$

in components,

$$\mathbf{D}_v = \begin{bmatrix} \frac{c_v}{2} + \widehat{K} & -\frac{c_v}{2} + \widehat{K} & 0 \\ & & \\ -\frac{c_v}{2} + \widehat{K} & \frac{c_v}{2} + \widehat{K} & 0 \\ & & \\ 0 & 0 & \frac{c_v}{2} \end{bmatrix} , \tag{4.17}$$

where we have used the constant $c_v = 2\eta$.

Similarly, we discretize the Maxwell model, in equation (4.12), by considering the stress implicitly. In indicial form, it becomes

$$\sigma'_{ij}{}^{n+1} = \left(1 + \frac{\Delta t}{\lambda_1}\right)^{-1} \left\{ \sigma'_{ij}{}^{n} + \frac{2\eta}{\lambda_1} \left[\left(\epsilon_{ij} - \frac{1}{2}\epsilon_{kk}\delta_{ij}\right)^{n+1} - \left(\epsilon_{ij} - \frac{1}{2}\epsilon_{kk}\delta_{ij}\right)^{n} \right] + \right.$$
$$\left. \frac{\widehat{K}}{\lambda_1} \left[\epsilon_{kk}^{n+1}\delta_{ij} - \epsilon_{kk}^{n}\delta_{ij}\right] \right\} , \tag{4.18}$$

which may be written in vector form, as

69

$$
\begin{bmatrix} \sigma'_{11} \\ \sigma'_{22} \\ \sigma'_{12} \end{bmatrix}^{n+1} = \left(1 + \frac{\Delta t}{\lambda_1}\right)^{-1} \left\{ \begin{bmatrix} \sigma'_{11} \\ \sigma'_{22} \\ \sigma'_{12} \end{bmatrix}'^{n} + \frac{2\eta}{\lambda_1} \left[\begin{bmatrix} \frac{1}{2}\epsilon_{11} - \frac{1}{2}\epsilon_{22} \\ -\frac{1}{2}\epsilon_{11} + \frac{1}{2}\epsilon_{22} \\ \gamma_{12} \end{bmatrix}^{n+1} - \right.
$$

$$
\left. \begin{bmatrix} \frac{1}{2}\epsilon_{11} - \frac{1}{2}\epsilon_{22} \\ -\frac{1}{2}\epsilon_{11} + \frac{1}{2}\epsilon_{22} \\ \gamma_{12} \end{bmatrix}^{n} \right] + \frac{\widehat{K}}{\lambda_1} \left[\begin{bmatrix} \epsilon_{11} + \epsilon_{22} \\ \epsilon_{11} + \epsilon_{22} \\ 0 \end{bmatrix}^{n+1} - \begin{bmatrix} \epsilon_{11} + \epsilon_{22} \\ \epsilon_{11} + \epsilon_{22} \\ 0 \end{bmatrix}^{n} \right] \right\} .
\tag{4.19}
$$

Now we can rewrite the relation in equation (4.12) in matrix form, with a constant coefficient matrix, $\mathbf{D}_{ve}$, that we shall call the *viscoelasticity matrix of moduli*. This matrix does not express a direct proportionality between the variation of the stress and the one of the strain, as in the viscous case. But it expresses the variation of the total change of the algorithmic stress (including its history) with respect to the rate of change of the strain, that is

$$
\boldsymbol{\sigma}^{n+1} + \lambda_1 \partial_t \boldsymbol{\sigma}'^{n+1} = \mathbf{D}_{ve} \dot{\boldsymbol{\epsilon}}'^{n+1} ,
\tag{4.20}
$$

where in components $\mathbf{D}_{ve}$ has the same form as the Newtonian one, in equation (4.17), except for the constant that now is defined as $c_{ve} = c_v/\lambda_1$, and $\widehat{K}/\lambda_1$ appears in place of $\widehat{K}$.

The discrete material models presented are implemented as a user defined subroutine for the software Abaqus/Standard 6.13, and the time derivatives of equation (4.3) are discretized implicitly with a generalized Newmark scheme [102]. The complete description of the spatial discretization for each term in equation (4.2) is given in Appendix A.
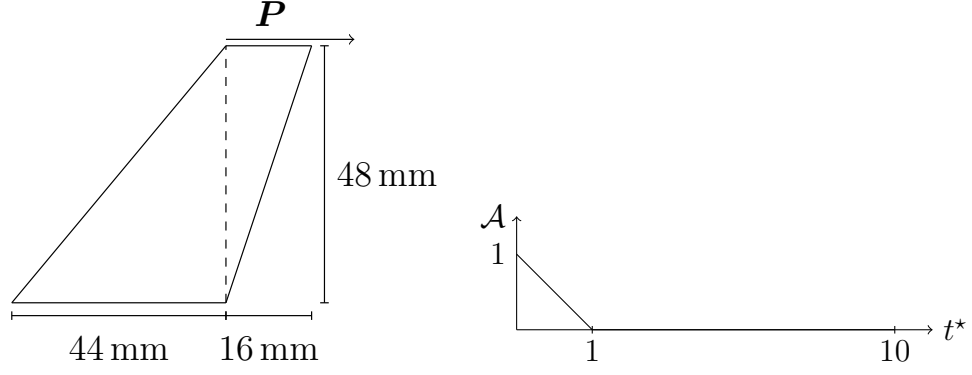
Figure 4.2 The left panel shows the Cook's membrane schematic for the numerical experiment. On the right panel, we display the values of the ramp of the amplitude of the applied load, denoted by $\mathcal{A}$, versus the normalized time, not in the same scale.

4.4   Results and Discussion

4.4.1   Convergence Tests

We present our numerical results in absence of gravity, and in terms of the surface coordinate system, for which the surface vector displacement and applied loads only have two in-plane nontrivial components, and therefore we omit the null third component to avoid cumbersome notation. To validate our formulation and implementation, we have performed several convergence tests.

One of the typical convergence tests for membrane structures is the Cook's membrane [103, 104]. This is a free-boundary problem in which a membrane, shaped as in the left panel of Figure 4.2, undergoes a load on its top boundary, while its bottom boundary is held fixed. We apply a horizontal load along the top boundary, given by $\boldsymbol{P} = (1,0)$ N, and the bottom boundary satisfies a homogeneous Dirichelet boundary condition on the displacement field, i.e., $\boldsymbol{u} = (0,0)$ m. All other boundaries of the membrane are free to move, and satisfy no-flux and traction-free boundary conditions. For the convergence test of both the Newtonian and Maxwell models, we apply a load with an amplitude, denoted by $\mathcal{A}$, linearly varying in time, as shown in the right panel of Figure 4.2. In problems in which a load is applied and/or removed, we relate the time of the loading/unloading phases to the characteristic time of the

(a)

(b)
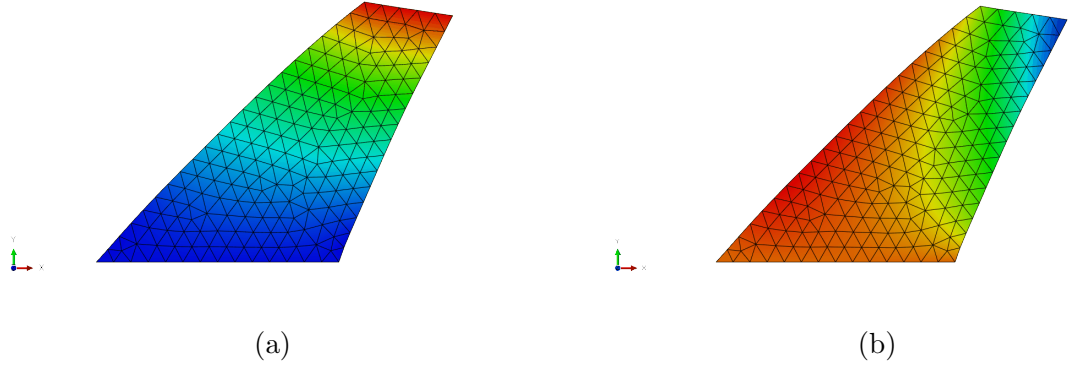
Figure 4.3 The final configuration, at $t^\star = 1$, of a Cook's membrane of viscoelastic material of Maxwell type, with viscosity coefficient $\eta = 10\,Pa\,s$, and relaxation time $\lambda_1 = 1\,s$. The color gradient represents contour plots of the displacement field, in which warmer shades mean higher values. In (a), we show the first component of the displacement field, u_1, that ranges between its minimum value, $u_{1min} = 0$ m (blue), and its maximum value, $u_{1max} = 5.686 \times 10^{-3}$ m (red). In (b), we display the second component, u_2, that ranges between its minimum value, $u_{2min} = -3.275 \times 10^{-3}$ m (blue), and its maximum value, $u_{2max} = 0$ m (red).

response of the material. For the case of Maxwell liquids we scale the time interval of

the loading/unloading phases by the normalized time $t^\star = t/\lambda_1$. On the other hand,

for Newtonian liquids, we use $t^\star = t/t_c$, where $t_c = 1$ s is a characteristic time scale for

viscous fluids. For the numerical investigations that follow, we consider membranes of

viscosity coefficient $\eta = 10$ Pa s, density $\rho = 10^3$ kg/m^3, and relaxation time $\lambda_1 = 1$ s

for the Maxwellian (for Maxwell model) membrane, unless specified differently.

In Figure 4.3, we show the deformed Maxwellian membrane at time $t^\star = 1$,

discretized by an unstructured mesh composed of 336 triangular elements. We display

the contour plots of the vector displacement field, for which warmer shades indicate

higher values. In Figure 4.3(a) we show the contour plot of the first component of the

vector displacement field, u_1, that ranges between its minimum value, $u_{1min} = 0$ m

(blue), on the bottom boundary, and its maximum value, $u_{1max} = 5.686 \times 10^{-3}$ m,

(red) on the top-right corner of the membrane. In Figure 4.3(b), we display the

contour plot of the second component of the vector displacement field, u_2, that ranges
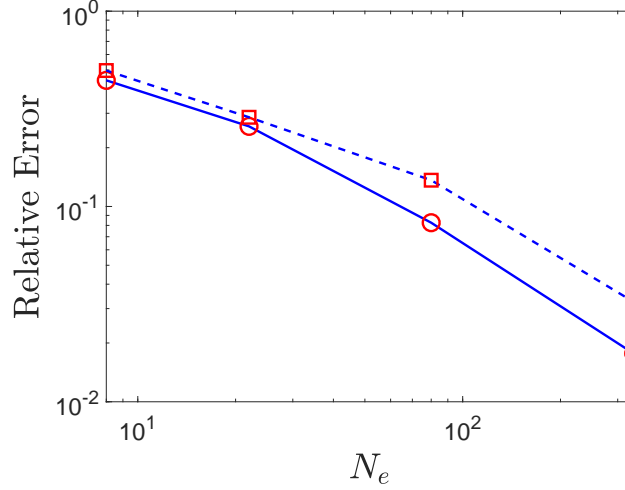
Figure 4.4 Convergence tests for the Cook's membrane for Maxwell (red square data on blue dashed curve) and Newtonian (red circle data on blue solid curve) models. We display the relative error on the computed u_1, as measured at the top-right corner of the deformed Cook's membrane, at time $t^\star = 1$, versus the number of elements, $N_e = 8, 22, 80, 336$, both in logarithmic scale.

between its minimum value, $u_{2min} = -3.275 \times 10^{-3}$ m (blue), on the top-right corner of the membrane, and its maximum value, $u_{2max} = 0$ m (red), on the left boundary.

By performing several numerical experiments, with a fixed time step, $\Delta t = 10^{-4}$ s, and refined unstructured meshes, we can have a quantitative analysis of the convergence of our numerical algorithms, equations (4.14) and (4.19), and show that our results converge under mesh refinement. In Figure 4.4, we show our numerical results of the relative error on the computed u_1, as measured at the top-right corner of the deformed Cook's membrane, at time $t^\star = 1$, versus the number of elements, $N_e = 2, 8, 22, 80, 336$, both in logarithmic scale. For the computation of the relative error, we have considered as approximation of the actual solution the result obtained with an unstructured mesh composed of $N_e = 1346$ elements. We represent with red squares on a blue dashed curve the data for the Maxwellian membrane, and with red circles on a blue solid curve the Newtonian one. We can see that the results of our implementation of both constitutive models converge, with increasing number of elements.
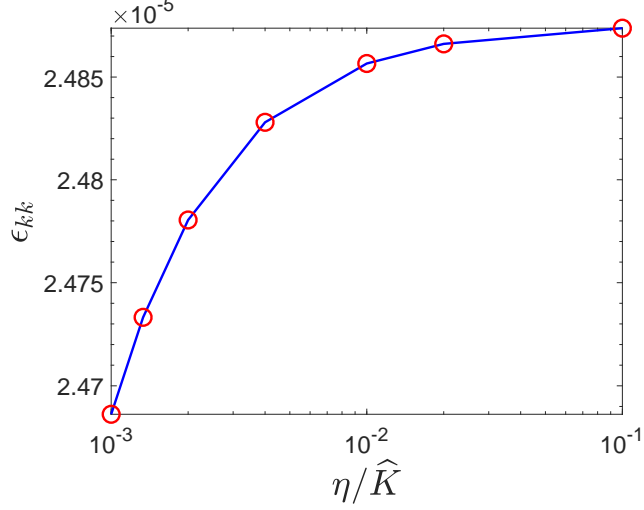
Figure 4.5 The computed volumetric strain, ϵ_{kk}, versus the dimensionless constant $\eta/\widehat{K}$, for different values of $\widehat{K} = 10^2, 5 \times 10^2, 10^3, 5 \times 10^3, 7.5 \times 10^3, 10^4$ Pa s, keeping $\eta = 10$ Pa s fixed, both in logarithmic scale.

A validation test for the pressure formulation and the near incompressibility condition is given by a tension experiment. For this test, the liquid membrane is deposited on a plane and surrounded by rigid plates, forming a square bounding box. On the left boundary, the plate is allowed to move vertically, by imposing a zero boundary condition for u_1. On the bottom boundary, the plate is allowed to move horizontally, by imposing a zero boundary condition for u_2. The right boundary satisfies a no-flux and traction-free boundary condition. The top boundary satisfies a no-flux boundary condition and it is displaced linearly in time by $\boldsymbol{u} = (0, 0.005)$ m, such that for $t^\star = 0$, the corresponding amplitude is $\mathcal{A} = 0$, and for $t^\star = 1$, the corresponding amplitude is $\mathcal{A} = 1$. Hence, by studying the dimensionless parameter related to the pressure, $\eta/\widehat{K}$, we can quantitatively verify that the pressure formulation leads, in the limit, to incompressibility. In Figure 4.5, we show the results of our simulations for the Maxwellian film. We measure the computed volumetric strain, ϵ_{kk}, for different values of $\widehat{K} = 10^2, 5 \times 10^2, 10^3, 5 \times 10^3, 7.5 \times 10^3, 10^4$ Pa s, keeping $\eta = 10$ Pa s fixed, both in logarithmic scale. We can see that the data corresponding to the small values of the dimensionless ratio $\eta/\widehat{K}$, have a smaller volume change
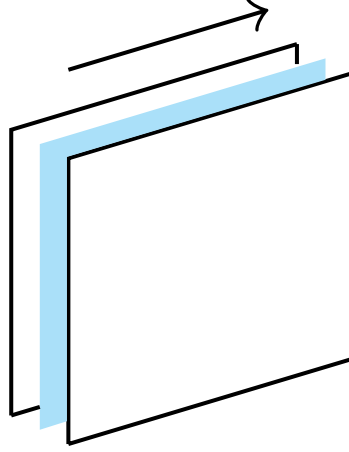
Figure 4.6 Schematic of a sheared membrane between parallel plates. Both plates are sheared on the top, held fixed at the bottom, and no-flux and traction-free boundary conditions are applied on the lateral boundaries of the plates. Friction between the liquid and the plates is neglected.

ϵ_{kk}. We have found that the optimal range for the near incompressibility condition is $\eta/\widehat{K} \in [10^{-3}, 10^{-1}]$. In fact, when $\eta/\widehat{K} < 10^{-3}$ the penalty method leads to stringent constraints on the time step [98, 105], whereas, $\eta/\widehat{K} > 10^{-1}$ allows for more compressibility of the material.

4.4.2 Membrane Deformation under Shear Flow

The first application we consider is the simple shear flow [11, 94] of a thin liquid layer between parallel rigid plates. In this investigation, we do not include friction effects between the liquid layer and the rigid plates. The shear motion is obtained by holding the bottom boundary of the plates fixed, and by horizontally shearing the top boundary, by either imposing a horizontal displacement, or a horizontal force. In Figure 4.6, we show the schematic of the setup of this numerical experiment, where square membranes of length $L = 10^{-1}$ m are used. For the first numerical experiment, a constant horizontal load $\boldsymbol{P} = (10^{-2}, 0)$ N has been linearly applied in time for $t^\star = 5$. The right and left boundaries satisfy a traction-free and no-flux boundary conditions,
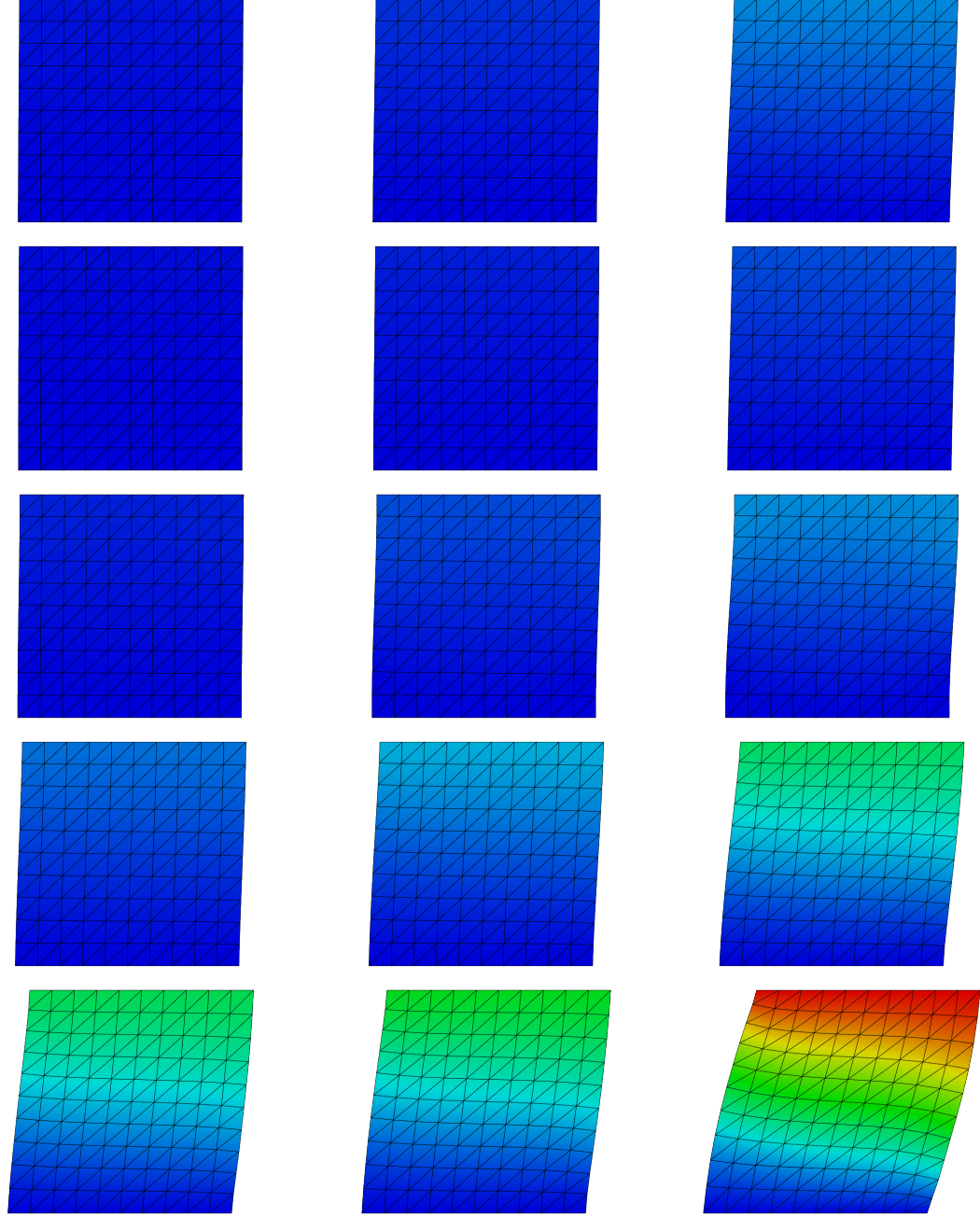
Figure 4.7 Comparison of the evolution of sheared membranes of Newtonian and Maxwellian fluids. The contour plots of u_1, are displayed at time $t^\star = 1, 2, 5$ (from left to right), where the red color represents the maximum value attained at $t^\star = 5$, $u_{1max} = 2.381 \times 10^{-2}$ m, and the blue color represents the minimum value, $u_{1min} = 0$ m. The viscosity coefficient for all membranes is $\eta = 20$ Pa s, and the relaxation times are $\lambda_1 = 0, 0.5, 1, 2, 5$ s, (from top to bottom).

and the bottom boundary is clamped. In Figure 4.7, we show the final configuration of sheared membranes of Maxwell type, compared to a viscous one. The contour

plots of u_1, are displayed at time $t^\star = 1, 2, 5$ (from left to right), where the red color represents the maximum value attained at $t^\star = 5$, $u_{1max} = 2.381 \times 10^{-2}$ m, and the blue color represents the minimum value, $u_{1min} = 0$ m. The viscosity coefficient for all membranes is $\eta = 20$ Pa s, and the relaxation times are $\lambda_1 = 0, 0.5, 1, 2, 5$ s, (from top to bottom). We observe that the liquid membrane of Maxwell type with the highest relaxation time has deformed the most, corresponding to a longer dimensional time of imposed load. Since this numerical experiment reproduces a simple shear motion, the second component of the displacement is identically zero, and it is not displayed.

Next, we investigate the effect of the relaxation time on both the stress and the displacement in the simple shear flow. We observe that the relaxation time, $\lambda_1 = 2\eta/G$, represents the ratio of the shear viscosity coefficient over the shear elastic modulus. Hence, by keeping the viscosity fixed, and by increasing λ_1, we increase the importance of viscosity relative to elasticity. In this test case, we displace the top plates by applying a velocity of $\mathbf{v} = (10^{-4}, 0)$ m/s. This boundary condition is time-dependent, with the magnitude of the applied velocity linearly decreasing in time, similarly to the ramp in Figure 4.2, but with final time $t^\star = 4$. In Figure 4.8, we plot the time evolution of the shear stress component, σ_{12}, for the values of the relaxation time $\lambda_1 = 0$ s (blue solid curve), 0.5 s (green dashed curve), 1 s (purple dash-dotted curve), 2 s (yellow dashed curve), 5 s (red dotted curve). In this Figure we can see that the limiting case, for $\lambda_1 = 0$ s, that corresponds to a Newtonian fluid, exhibits the linear relationship between the shear stress and strain rate. Moreover, the Maxwellian liquid of relaxation time $\lambda_1 = 0.5$ s shows a similar behavior, and the ones with $\lambda_1 > 1$ s show the stress relaxation feature, typical of Maxwell model [11], in which the peak of shear stress is lowered by higher values of the relaxation time.

Following that, we carry out one last parameter study on the relaxation time. For this test case, and different from the previous one in which we imposed an initial velocity for the shear motion, we displace the top plate by applying a horizontal
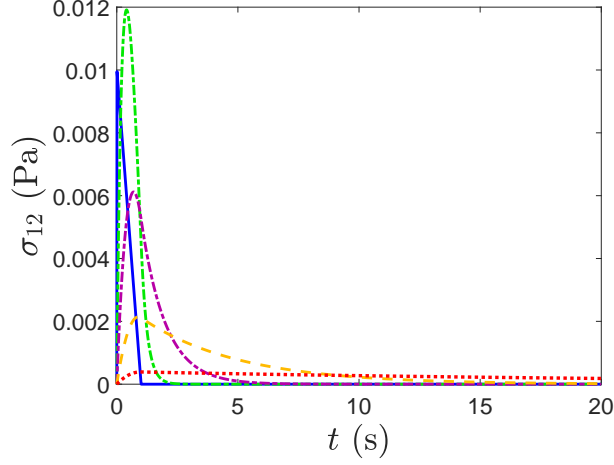
Figure 4.8 Evolution of the shear stress component, σ_{12}, of sheared membranes, for different values of the relaxation time $\lambda_1 = 0$ s (blue solid curve), 0.5 s (green dashed curve), 1 s (purple dash-dotted curve), 2 s (yellow dashed curve), 5 s (red dotted curve).
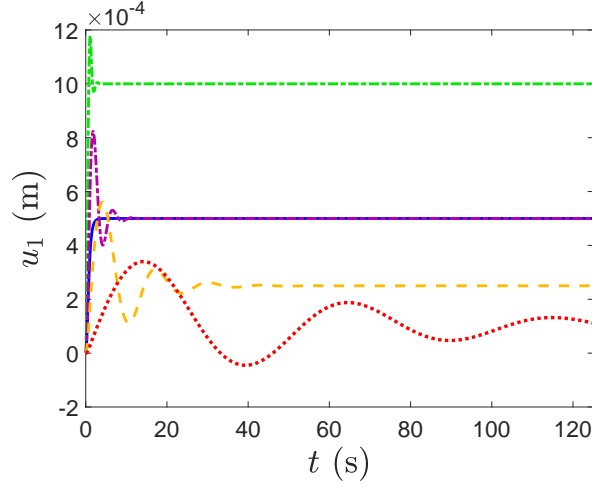
Figure 4.9 Evolution of u_1, measured from the top-right corner of the sheared membrane, for different values of the relaxation time $\lambda_1 = 0$ s (blue solid curve), 0.5 s (green dashed curve), 1 s (purple dash-dotted curve), 2 s (yellow dashed curve), 5 s (red dotted curve).

load $\boldsymbol{P} = (0.1, 0)$ N, linearly decreasing in time, similarly to the ramp in Figure 4.2, but with final time $t^\star = 25$. When the load or the deformation is removed, different behaviors occur according to the material model considered. A linearly elastic material bounces back and forth, with no constitutive dissipation. A Newtonian liquid exhibits
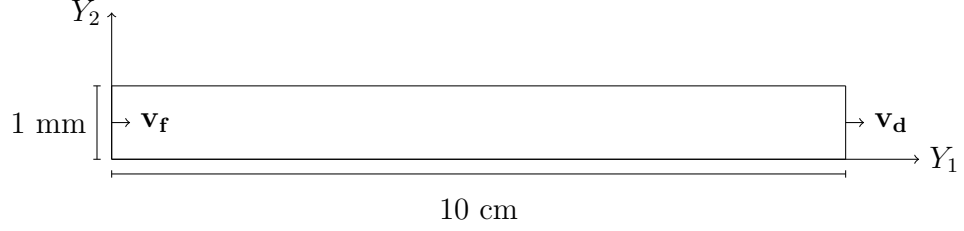
Figure 4.10 Schematic of the drawing process of a thin viscoelastic membrane (not in scale).

resistance to the shearing velocity and no elastic behavior. A Maxwell liquid can combine both these two characteristic behaviors, as described in Section 4.3. We measure u_1, on the top-right corner of the membrane, and track its evolution in time. In Figure 4.9 we show the values corresponding to the results with $\lambda_1 = 0$ s (blue solid curve), 0.5 s (green dashed curve), 1 s (purple dash-dotted curve), 2 s (yellow dashed curve), 5 s (red dotted curve). We observe how the viscous fluid, corresponding to the curve with $\lambda_1 = 0$ s, reaches a plateau and does not exhibit any elastic effects. In fact, even when the load is removed, the Newtonian membrane displacement remains constant. By contrast, the Maxwell liquids exhibit a nearly elastic response in the early times, that is dissipated by viscosity in later times. As stated in the previous paragraph, by increasing the relaxation time λ_1, at parity of viscosity coefficient, we increase the importance of the viscosity relative to elasticity. We can in fact see the increasing effects of viscosity in the oscillations with smaller amplitude and larger wavelengths for the curves of $\lambda_1 > 1$ s.

4.4.3   Membrane Deformation under Extensional Flow

Finally, we consider the application of the drawing of viscoelastic membranes with constant thickness, as a planar study of a more general redrawing process of viscoelastic flat sheets [106]. Drawing or redrawing processes are manufacturing practices for which a sheet, usually of glass or metal, is heated and stretched to obtain a reduced cross sectional area, such as in the production of glass fibers (see [90, 91, 106] and references
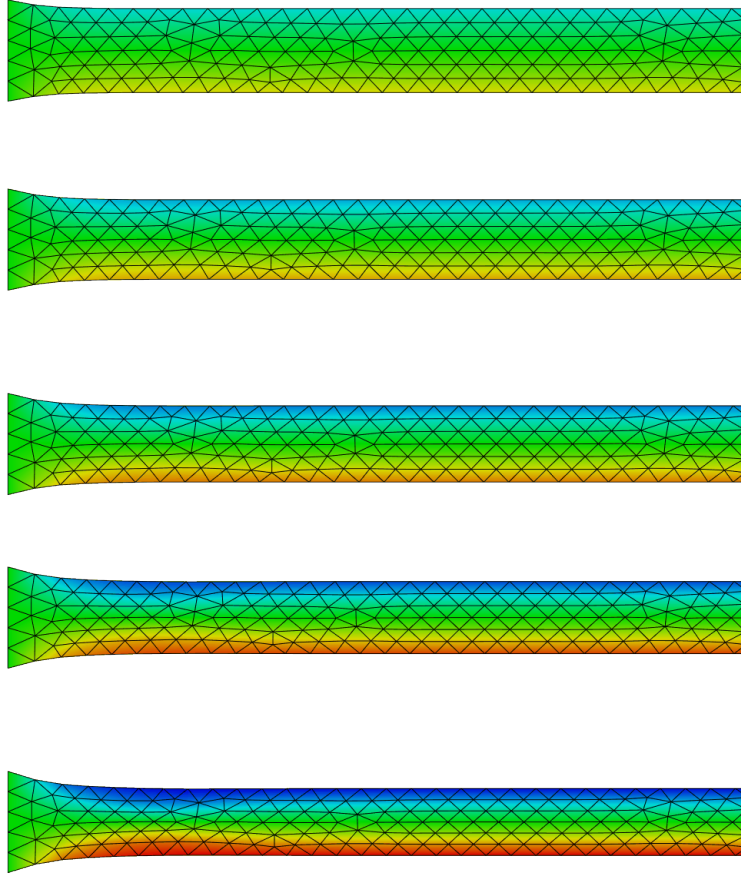
Figure 4.11 Left region of drawn viscoelastic membranes. Contour plots of u_2, for the quasi-static solution of drawn membranes, of relaxation time $\lambda_1 = 0, 0.5, 1, 2, 5$ s, (from top to bottom), at $t \sim 23$ s. The blue color on the top of the necking region represents the minimum value of u_2, $u_{2min} = -1.727 \times 10^{-4}$ m, and the red color at the bottom of the necking region represents its maximum value, $u_{2max} = -u_{2min}$.

therein). This process usually consists of two phases: a sheet is first cast and then subsequently reheated and drawn [90]. We consider only the drawing phase, for which we model the sheet as a slender membrane of initial length $L = 100$ mm and width $W = 1$ mm, with its bottom-left corner coinciding with the origin of the surface coordinate system (see Appendix A) in reference state, (Y_1, Y_2), as depicted in Figure 4.10. The membrane is clamped on its right and left boundaries to rigid walls that move with a drawing velocity on the right boundary, $\mathbf{v_d} = (10^{-3}, 0)$ m/s, and a feed velocity on the left boundary, $\mathbf{v_f} = (10^{-4}, 0)$ m/s, respectively (unless specified
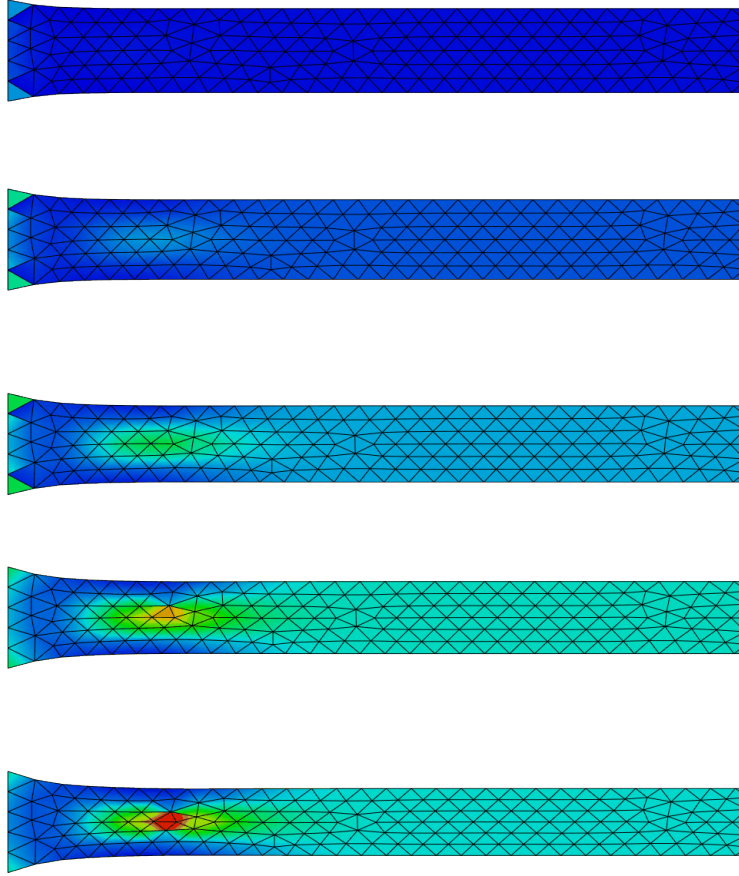
Figure 4.12 Left region of drawn viscoelastic membranes. Contour plots of the second normal stress component, σ_{22}, of viscoelastic membranes of relaxation time $\lambda_1 = 0, 0.5, 1, 2, 5$ s, (from top to bottom), at $t \sim 23$ s. The principal stress σ_{22} has reached its maximum value, $\sigma_{22max} = 8.605 \times 10^{-1}$ Pa, represented by the red shades, and its minimum value, $\sigma_{22min} = 1.193 \times 10^{-2}$ Pa, represented by the blue shades. The region of maximum stress represents the onset of buckling.

differently). The top and bottom boundary satisfy no-flux and traction-free boundary conditions.

We start by considering the drawing process in which viscoelastic membranes, with constant viscosity, are stretched and held in thermal equilibrium. The setup of this process, together with the initial size of the membrane (not in scale), is depicted in Figure 4.10. As the viscoelastic film is stretched, it necks, i.e., it shrinks along the direction perpendicular to the elongation direction. In Figure 4.11, we show contour plots of u_2, for the quasi-static solution of the central region of drawn membranes,
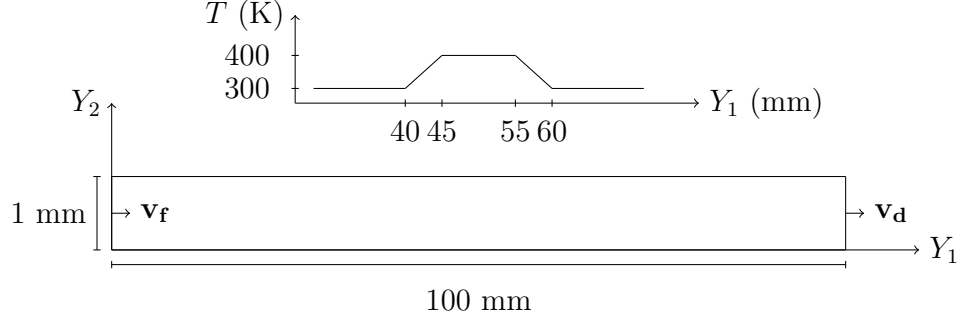
Figure 4.13 Schematic of the drawing process of a thin viscoelastic membrane (not in scale), and the temperature profile at the location of the furnace.

of relaxation time $\lambda_1 = 0, 0.5, 1, 2, 5$ s, (from top to bottom), at $t \sim 23$ s, and in Figure 4.12, we display the contour plots of σ_{22} for the same membranes as in Figure 4.11, at the same time. In the latter, we note that for higher relaxation times, the membranes exhibit more necking, reaching the minimum value of u_2, represented by the blue shade on the top boundary of the membrane, $u_{2min} = -1.727 \times 10^{-4}$ m, and its maximum value at the bottom of the necking region, represented by the red color, $u_{2max} = -u_{2min}$. Moreover, in Figure 4.12, we observe that the principal stress, σ_{22}, has reached its maximum value, $\sigma_{22max} = 8.605 \times 10^{-1}$ Pa, represented by the red shades, and its minimum value, $\sigma_{22min} = 1.193 \times 10^{-2}$ Pa, represented by the blue shades. The region of the maximum value of the normal stress suggests an onset of buckling. To investigate this phenomenon and its dependence on the stiffness of the material, in what follows, we consider membranes with variable viscosity.

Next, we analyze drawing processes in which the stretched film is also heated [90]. As the membrane is drawn, it passes a heated region, representing an idealized furnace, starting at location $Y_1 = 40$ mm. The furnace temperature follows a linear profile that increases from the ambient temperature, $T_a = 300$ K, reaching its maximum, $T_f = 400$ K, that is held constant over the interval 45 mm $< Y_1 <$ 55 mm, and returns to the ambient temperature at $Y_1 = 60$ mm, as shown in Figure 4.13. According to the industrial application of interest, the dimension of the membrane and the furnace can
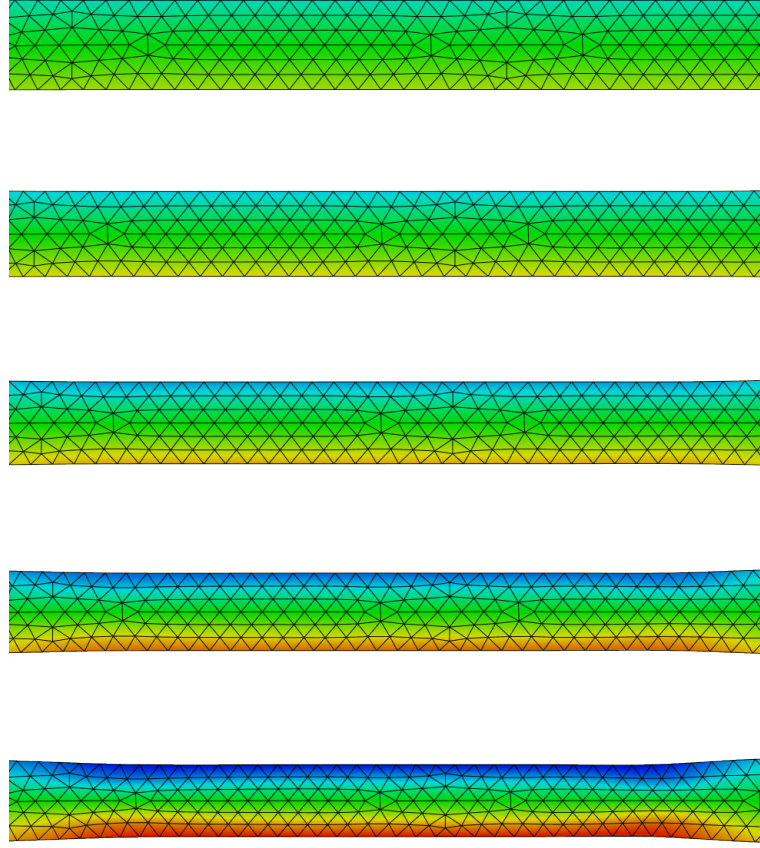
Figure 4.14 Central region of drawn viscoelastic membranes. Contour plots of u_2, for the quasi-static solution of drawn membranes, of relaxation time $\lambda_1 = 0, 0.5, 1, 2, 5$ s, (from top to bottom), at $t \sim 10$ s. The blue color on the top of the necking region represents the minimum value of u_2, $u_{2min} = -5.863 \times 10^{-5}$ m, and the red color at the bottom of the necking region represents its maximum value, $u_{2max} = -u_{2min}$.

vary [90]. We are interested in industrially relevant processes where the furnace zone is short relative to the membrane length, but large relative to the membrane width. Consistent with Srinivasan et al. [106], we assume that the temperature irradiation between the heating device and the viscoelastic membrane is in equilibrium, so that the temperature in the fluid equals the one prescribed by the furnace. As the temperature reaches its maximum, we model the viscosity as linearly dependent on the temperature T, according to the following expression
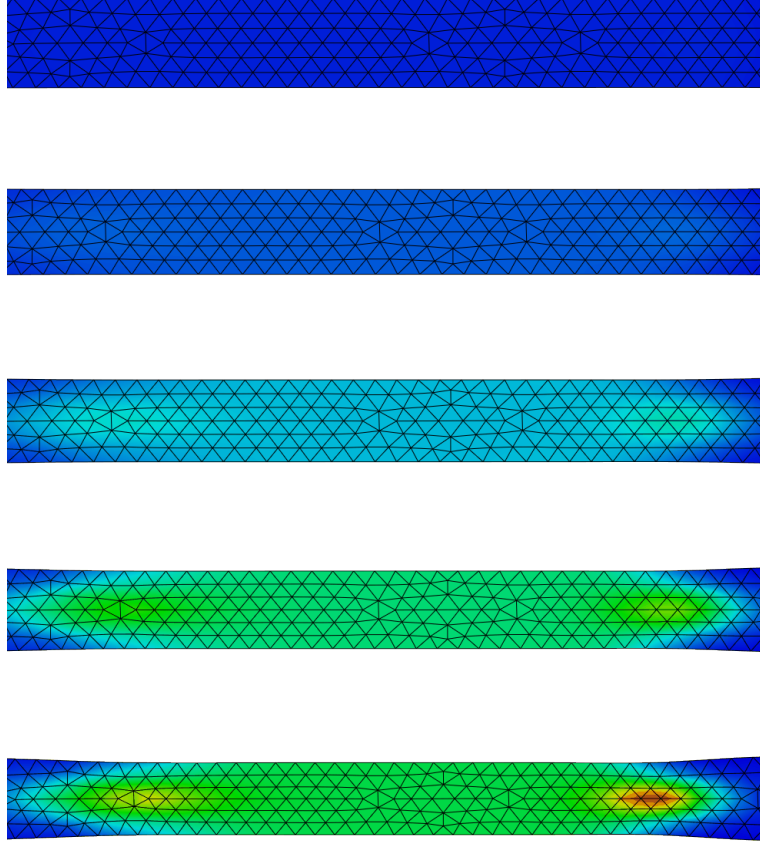
Figure 4.15 Central region of drawn viscoelastic membranes. Contour plots of the second normal stress component, σ_{22}, of viscoelastic membranes of relaxation time $\lambda_1 = 0, 0.5, 1, 2, 5$ s, (from top to bottom), at $t \sim 10$ s. The principal stress σ_{22} has reached its maximum value, $\sigma_{22max} = 3.759 \times 10^{-1}$ Pa, represented by the red shades, and its minimum value, $\sigma_{22min} = -1 \times 10^{-3}$ Pa, represented by the blue shades. The region of maximum stress represents the onset of buckling.

$$\eta = \eta_a - \frac{\eta_f - \eta_a}{T_f - T_a}(T - T_a),\tag{4.21}$$

where we have considered the difference between the viscosity of the liquid in the furnace, η_f, and in the ambient, η_a, to be modeled as $\eta_f - \eta_a = \eta_a/2$, with $\eta_a = 1$ Pa s.

In Figure 4.14, we show contour plots of u_2, for the quasi-static solution of the central region of drawn membranes, of relaxation time $\lambda_1 = 0, 0.5, 1, 2, 5$ s, (from top to bottom), at $t \sim 10$ s. As the membranes are stretched, they exhibit some necking
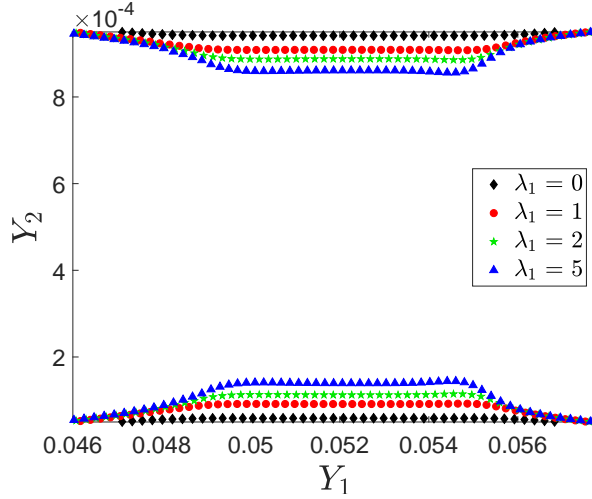
Figure 4.16 Profile evolution, at the point of maximum necking, in the central region of the stretched Newtonian and Maxwellian membranes, for $\lambda_1 = 0$ s (black diamonds), $\lambda_1 = 1$ s (red circles), $\lambda_1 = 2$ s (green stars), $\lambda_1 = 5$ s (blue triangles), at $t \sim 10$ s.

in their central part, corresponding to the region of lowest viscosity, consistently with [107]. The blue color on the top of the necking region represents the minimum value of u_2, $u_{2min} = -5.863 \times 10^{-5}$ m, and the red color at the bottom of the necking region represents its maximum value, $u_{2max} = -u_{2min}$. In addition, by analyzing the stresses even in the case of heated membranes, we can identify the onset of buckling, leading to wrinkling instabilities. These are known to arise when viscous [106, 107] or elastic [108] sheets are stretched. In Figure 4.15, we show the second normal stress component, σ_{22}, for the corresponding stretched membranes in Figure 4.14. The principal stress σ_{22} has reached its maximum value, $\sigma_{22max} = 3.759 \times 10^{-1}$ Pa, represented by the red shades, and its minimum value, $\sigma_{22min} = -1 \times 10^{-3}$ Pa, represented by the blue shades. The region of maximum stress represents the onset of buckling, due to the in-plane compression generated by Poisson's effect [108].

Next, we are interested in tracking the evolution of the membrane profile, as it necks. Hence, in Figure 4.16, we show the discrete points corresponding to the nodes belonging to the boundary of the mesh, at $t \sim 10$ s, of the central region of drawn membranes, of relaxation time $\lambda_1 = 0$ s (black diamonds), $\lambda_1 = 1$ s (red circles),
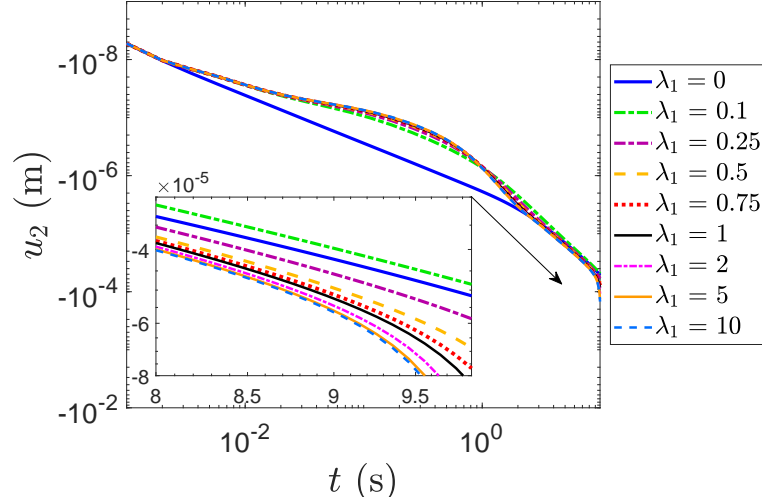
Figure 4.17 Comparison of u_2 at the midpoint of the top boundary of the stretched Newtonian and Maxwellian membranes, for $\lambda_1 = 0$ s (blue solid curve), 0.1 s (green dashed curve), 0.25 s (purple dash-dotted curve), 0.5 s (yellow dashed curve), 0.75 s (red dotted curve), 1 s (black solid curve), 2 s (magenta dash-dotted curve), 5 s (orange solid curve), and 10 s (light blue dashed curve), both in logarithmic scale. The inset shows a magnification of the graphs for $t \in [8, 10]$ s.

$\lambda_1 = 2$ s (green stars), $\lambda_1 = 5$ s (blue triangles). We can see that the Maxwellian membranes with higher values of the relaxation time exhibit more necking.

We next want to quantitatively assess the effect of the relaxation time on the necking. Therefore, in Figure 4.17, we analyze the evolution of the point of maximum necking, at the center of the redrawn Newtonian and Maxwellian sheets. We plot u_2, at the midpoint of the top boundary of the stretched film, for $\lambda_1 = 0$ s (blue solid curve), 0.1 s (green dashed curve), 0.25 s (purple dash-dotted curve), 0.5 s (yellow dashed curve), 0.75 s (red dotted curve), 1 s (black solid curve), 2 s (magenta dash-dotted curve), 5 s (orange solid curve), and 10 s (light blue dashed curve), both in logarithmic scale.

Finally, we investigate the maximum stretch, defined as $\bar{\varepsilon} = u_{1max}/L$, attained by the elongated membranes before the onset of buckling. This quantity, industrially relevant, can help manufacturers avoid undesired wrinkling instabilities. In Figure 4.18, we investigate the influence of the relaxation time, for $\lambda_1 \in [0, 10]$ s, on $\bar{\varepsilon}$,
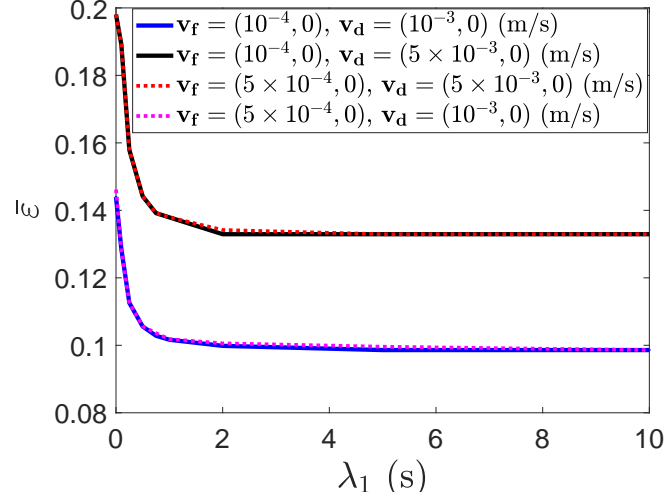
Figure 4.18 Stretch factor, $\bar{\varepsilon} = u_{1max}/L$, versus the relaxation time λ_1, for four different sets of feeding and drawing velocities: $\mathbf{v_f} = (10^{-4}, 0)$ m/s and $\mathbf{v_d} = (10^{-3}, 0)$ m/s (blue solid curve), $\mathbf{v_f} = (5 \times 10^{-4}, 0)$ m/s and $\mathbf{v_d} = (10^{-3}, 0)$ m/s (magenta dotted curve), $\mathbf{v_f} = (10^{-4}, 0)$ m/s and $\mathbf{v_d} = (5 \times 10^{-3}, 0)$ m/s (black solid curve), and $\mathbf{v_f} = (5 \times 10^{-4}, 0)$ m/s and $\mathbf{v_d} = (5 \times 10^{-3}, 0)$ m/s (red dotted curve).

for four different sets of feeding and drawing velocities: $\mathbf{v_f} = (10^{-4}, 0)$ m/s and $\mathbf{v_d} = (10^{-3}, 0)$ m/s (blue solid curve), $\mathbf{v_f} = (5 \times 10^{-4}, 0)$ m/s and $\mathbf{v_d} = (10^{-3}, 0)$ m/s (magenta dotted curve), $\mathbf{v_f} = (10^{-4}, 0)$ m/s and $\mathbf{v_d} = (5 \times 10^{-3}, 0)$ m/s (black solid curve), and $\mathbf{v_f} = (5 \times 10^{-4}, 0)$ m/s and $\mathbf{v_d} = (5 \times 10^{-3}, 0)$ m/s (red dotted curve). We can see that membranes that are drawn at higher speeds, i.e., with $\mathbf{v_d} = (5 \times 10^{-3}, 0)$ m/s, reach a maximum elongation of 20% from their initial length. We moreover notice that membranes with equal drawing velocities exhibit a similar behavior, although the ratio of the magnitude of their drawing to feed velocities, is different, ranging from 10 for the first and third set of data, to 50 for the second and fourth ones.

4.5   Conclusions

We have presented a novel numerical investigation of the dynamics of nearly incompressible viscoelastic liquid membranes. We have introduced a displacement-based finite element formulation, in which the stresses are expressed for both

viscoelastic fluids of Maxwell type, and viscous (Newtonian) fluids. For the nearly incompressibility condition of both the Newtonian and Maxwellian cases, we have introduced a penalty function, in which the penalty constant is proportional to the viscosity of the fluid. We have validated our numerical implementation with several numerical experiments, demonstrating mesh-independence of our results, and validity of the formulation for near incompressibility, in the limit of the dimensionless parameter $\eta/\widehat{K}$.

We have focused on two main applications of our general numerical framework: the shear flow [11] and the extensional flow in drawing processes [90, 91]. For the case of the simple shear flow of membranes between parallel plates, we have investigated the effect of the relaxation time on the stress relaxation and the dynamics of the liquid. Comparing the behavior of sheared Newtonian and Maxwellian membranes, we have observed the effects of viscoelasticity on the nature of the dynamics, as well as on their final configuration. We have found that Maxwellian membranes deform the most, compared to Newtonian ones, when they are continuously sheared. While they exhibit an elastic response, that is constitutively damped by viscosity, in the case of loading/unloading forcing.

For the drawing process of Newtonian and Maxwellian membranes, with a constant or thermally-dependent viscosity, we have investigated how viscoelasticity affects the necking of the membranes in extensional flows. We have found that higher values of the relaxation time enhance the necking of the stretched membranes. Finally, we have investigated the influence of the relaxation time on the maximum stretch attained by the membranes before the onset of wrinkling instabilities, that are known to arise when viscous [106, 107] or elastic [108] sheets are stretched. We have found that higher values of the relaxation time facilitate the onset of buckling and therefore the emergence of the wrinkling instabilities. To have a better understanding of this phenomenon, one should model the sheets as shells, so that they possess not only a

stretching energy, but also a bending energy. We propose this formulation in the next chapter.

CHAPTER 5

FREE-BOUNDARY FLOW OF VISCOELASTIC SHEETS

5.1   Introduction

In this chapter, we introduce our preliminary work on three-dimensional simulations
of thin layers of viscoelastic fluids that are capable of stretching and bending. The
problem of the buckling of a viscoelastic thin sheet has been widely studied in classical
continuum mechanics [109]. This problem has two natural limiting situations: the
elastic limit (also called by Euler the problem of *elastica* [110]) and the viscous limit
(called by analogy the problem of *viscida* [109]). We propose to numerically simulate
the intermediate regime of this phenomenon, that, by analogy, we shall refer to as the
problem of *viscoelastica*.

Our numerical investigation aims to be a natural extension of the computational
study developed by Batty et al. [111], in the field of Physics-based Computer
Animations. Simulations of thin incompressible viscous sheets that can sag, fold,
buckle and wrinkle, are obtained by Batty et al. [111] within a discrete Lagrangian
formulation. In their work, the stresses exerted on a deformed sheet are implicitly
accounted for through the stretching and bending energy densities, defined for linearly
elastic shells. Surface tension effects are considered through the surface energy density
[94].

In their computational investigation, Batty et al. use approximations valid
within the theory of thin elastic shells to find the energy densities associated to
both stretching (in-plane) and bending (transverse) deformations, based on the linear
relationship that exist between the stress and the strain tensor in linear elasticity
[112]. To apply notions proper of shell theory (statics) to the study of viscous sheets in
motion (dynamics), Batty et al. [111] take advantage of the Stokes-Rayleigh analogy,
that relates the constitutive equations and the material parameters of elastic solids

and viscous fluids. In fact, Stokes [113] and Rayleigh [114], independently proved that the constitutive relation for viscous fluids is analogous to the one for elastic solid materials, provided the displacement is replaced by the velocity, and thus the strain replaced by the strain rate [115]. By this correspondence, techniques used to solve problems for elastic solids can be extended to find solutions of Stokes (creeping) flow problems. In the present chapter, we find an extension of the Stokes-Rayleigh analogy to account for linear viscoelastic constitutive models. To expand the framework developed by Batty et al. [111], one should propose a viscoelastic stretching energy potential, analogous to the elastic one. This modification would allow to obtain simulations of thin viscoelastic layers of fluids that are visually interesting for the Computer Graphics community and physically accurate, and that include features typical of viscoelasticity: stress relaxation, creep, and hysteresis (the relationship between the stress tensor and the strain rate is time-dependent).

However, to the best of our knowledge, the formulation of a viscoelastic energy potential cannot follow exactly the same form of the linear elastic case [112], because the relationship between the stress and the strain tensors is not a linear relation, but a differential one. Therefore the analogy that has successfully worked for the linear elastic and viscous cases, cannot equally provide an aid for the extension to the viscoelastic case. Thus, to account for viscoelastic effects, one should directly utilize a stressed-based formulation, rather than an energy-based one. This would need a new approach in the mathematical and physical modeling and an overhaul of the numerical framework in [111], that goes outside of the scope of the present work. Nonetheless, in this chapter we give the complete description of the problem, and leave as future work the possibility of expansion.

In the first part of this chapter, we describe in detail the theoretical background needed for the discrete formulation [111]. We then propose how to extend the Stokes-Rayleigh analogy to include viscoelastic constitutive models. Finally, we show
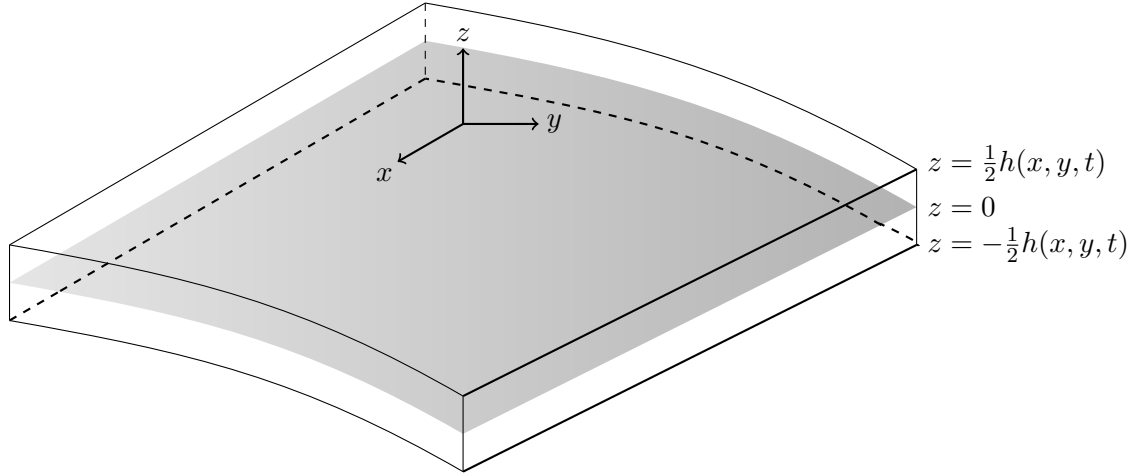
Figure 5.1 Schematic of a $3D$ thin layer of fluid.

two applications of the numerical formalism presented, describing different physical phenomena for viscous fluids: the *viscous catenary* problem that exhibits sagging and stretching of a thin sheet of viscous fluid attached to two rigid walls, and a *viscous bubble*, i.e., a thin viscous film on a solid substrate enclosing an air bubble, that wrinkles and collapses when punctured. The extension of these applications to include viscoelastic effects are left as future work.

5.2 Mathematical Formulation

In contrast to the cases considered in Chapters 2 and 3, where the fluid is geometrically confined, due to the solid substrate, represented by the x-axis ($y = 0$), in this chapter the slender geometry of the fluid sheet is described through a free-boundary, three-dimensional domain Ω. Its boundary, $\partial\Omega$, is constituted by two free surfaces: the top surface, namely H^+, of equation $z = \frac{1}{2}h(x, y, t)$, and the bottom surface, namely H^-, of equation $z = -\frac{1}{2}h(x, y, t)$; where the midsurface is, without loss of generality, $z = 0$ [37, 39, 116] (see Figure 5.1 for a sketch). Thus, we have that

$$-\frac{h}{2} \leq z \leq \frac{h}{2}. \tag{5.1}$$

In thin shell theory, it is customary to use notations borrowed from differential geometry and tensor calculus. Hence, we can write a position vector $\mathbf{x} = (x, y, z) \in \mathbb{R}^3$ in the equivalent form $\mathbf{x} = (x_1, x_2, x_3)$. The use of an indexed generic component x_i of a vector $\mathbf{x}$ is preferred when the summation convention (or indicial notation) is adopted for repeated indices. By convention, Greek indices $\{\alpha, \beta\} = \{1, 2\}$ are used for in-plane components of tensors, while x_3 refers to the transversal coordinate that is locally normal to the surface. A matrix (or tensor) $\mathbf{A}$, can be defined in terms of its components by $\mathbf{A} = a_{ij}$, where Latin indices $\{i, j, k\} = 1, 2, 3$.

5.3   Governing Equations for Thin Liquid Sheets

We report here the conservation laws for creeping (Stokes) flows

$$\nabla \cdot \boldsymbol{\Upsilon} + \mathbf{F_b} = 0\,, \tag{5.2a}$$

$$\nabla \cdot \mathbf{v} = 0\,, \tag{5.2b}$$

where $\mathbf{F_b}$ is the body (or volumetric) force, such as the gravitational force and $\boldsymbol{\Upsilon}$ represents the totality of stresses, that depend on the gradient of the vector velocity field, denoted by $\mathbf{v} = (v_1(x, y, t), v_2(x, y, t), v_3(x, y, t))$. In what follows, we consider the stress constitutive model for viscous (Newtonian) fluids, and we will include viscoelastic stresses in Section 5.6.

Supposing that there is a distribution of stress throughout the shell, we can write the stress tensor referred to the midsurface

$$\Upsilon^{i\lambda} = \widehat{h}\varsigma_\alpha^\lambda \sigma^{i\alpha}\,, \tag{5.3a}$$

$$\Upsilon^{i3} = \widehat{h}\sigma^{i3}\,, \tag{5.3b}$$

where the definitions of ς and $\widehat{h}$ are given in Appendix B. For a viscous fluid, we can describe the stress tensor, σ^{ij}, at an arbitrary point in the sheet as

$$\sigma^{ij} = 2\eta g^{ik} g^{jl} \dot{\epsilon}_{kl} - p g^{ij} \, , \tag{5.4}$$

where p is the pressure, $\dot{\epsilon}_{ij}$ the strain rate tensor (whose definition is provided in the following section), and $g^{\alpha\beta}$ represent the contravariant components of the metric tensor, defined in Appendix B. Following [37, 39], the equation of equilibrium (5.2a) for a shell becomes

$$\Upsilon^{\alpha\beta}|_\alpha - b_\alpha^\beta \Upsilon^{\alpha 3} + \Upsilon_{,3}^{3\beta} = -\widehat{h}\rho F_{b\alpha} \, , \tag{5.5a}$$

$$\Upsilon^{\alpha 3}|_\alpha + b_{\alpha\beta}\Upsilon^{\alpha\beta} + \Upsilon_{,3}^{33} = -\widehat{h}\rho F_{b3} \, , \tag{5.5b}$$

where $b_{\alpha\beta}$ are the covariant components of the second fundamental tensor of the midsurface, whose form is given in Appendix B. The incompressibility condition, equation (5.2b), reads

$$(\widehat{h}w)_{,z} + [a^{\alpha\beta} + z(b^{\alpha\beta} - 2\kappa_m a^{\alpha\beta})]u_\alpha|_\beta = 0 \, , \tag{5.6}$$

where the definition of the mean curvature, κ_m, and of the contravariant components of the (symmetric) metric tensor, $a^{\alpha\beta}$, are given in Appendix B, and where $_{,\alpha}$ indicates, by convention, $\partial/\partial_{x_\alpha}$. We define the quantities

$$n^{\alpha\beta} := \int_{H^-}^{H^+} \Upsilon^{\alpha\beta} dz \tag{5.7a}$$

$$q^\alpha := \int_{H^-}^{H^+} \Upsilon^{\alpha 3} dz \tag{5.7b}$$

$$\mathcal{P}^i := F_b^i \int_{H^-}^{H^+} \rho \widehat{h} dz + \mathcal{F}_+^i + \mathcal{F}_-^i \, , \tag{5.7c}$$

94

where $\mathcal{F}^i_\pm := \Lambda_\pm \Upsilon^{ij}_\pm n^\pm_i$ are the components of the stress applied in the direction $\mathbf{a}_i$ to the outer surface, measured per unit area of the midsurface [39]. We emphasize the difference in the notation of the normal vector $n^\pm_i$, that has one Latin index, and the stress resultant tensor $n^{\alpha\beta}$, with two Greek superscripts.

We integrate equation (5.5a) with respect to z, from H^- to H^+, and use the quantities in equation (5.7) to obtain

$$n^{\alpha\beta}|_\alpha - b^\beta_\alpha q^\alpha + \mathcal{P}^\beta = 0\,, \tag{5.8a}$$

$$q^\alpha|_\alpha + b_{\alpha\beta} n^{\alpha\beta} + \mathcal{P}^3 = 0. \tag{5.8b}$$

We now define the bending moment tensor (or stress couple) as

$$m^{\alpha\beta} := \int_{H^-}^{H^+} z \Upsilon^{\alpha\beta} dz\,. \tag{5.9}$$

We multiply equation (5.8a) by z and integrate in z from H^- to H^+. Using equation (5.9), we can write

$$m^{\alpha\beta}|_\alpha - q^\beta + \mathcal{M} = 0\,, \tag{5.10}$$

where

$$\mathcal{M}^\beta := F^\beta_b \int_{H^-}^{H^+} \rho z \widehat{h} dz + \frac{h}{2}(\mathcal{F}^\beta_+ - \mathcal{F}^\beta_-)\,. \tag{5.11}$$

Now we isolate the term q^β in equation (5.10), and use it into equation (5.8a), obtaining

$$n^{\alpha\beta}|_\alpha - b^\beta_\alpha \left(\mathcal{M}^\alpha + m^{\beta\alpha}|_\beta \right) + \mathcal{P}^\beta = 0\,. \tag{5.12}$$

We then define the quantities

$$N^{\alpha\beta} := n^{\alpha\beta} + b_\vartheta^\beta m^{\vartheta\alpha} \,, \tag{5.13a}$$

$$M^{\alpha\beta} := \frac{1}{2}\left(m^{\alpha\beta} + m^{\alpha\beta}\right) \,. \tag{5.13b}$$

We can finally rewrite the equations (5.8) of equilibrium as

$$N^{\alpha\beta}|_\alpha - 2b_\vartheta^\beta M^{\vartheta\alpha}|_\alpha - b_\vartheta^\beta|_\alpha M^{\vartheta\alpha} + \mathcal{P}^\beta - b_\alpha^\beta \mathcal{M}^\alpha = 0 \,, \tag{5.14}$$

$$M^{\alpha\beta}|_{\alpha\beta} - b_{\alpha\vartheta} b_\beta^\vartheta M^{\alpha\beta}| + b_{\alpha\beta} N^{\alpha\beta} + \mathcal{P}^3 + \mathcal{M}^\alpha|_\alpha = 0 \tag{5.15}$$

To define the boundary conditions at the free surfaces of the sheet, we let $\mathbf{P}^\pm = P_i^\pm \mathbf{c}_\pm^i = P_\pm^i \mathbf{c}_i^\pm$ be the vector of the stress applied to the outer surfaces $H^\pm$ per unit area. Hence, $P_\alpha^\pm$ or $P_\pm^\alpha$ are the tangential components, and $P_3^\pm = P_\pm^3$ are the normal components of the applied stress. The continuity of stress at the boundary of the sheet is then described by

$$\sigma_\pm^{ij} n_i^\pm \mathbf{g}_j^\pm = \mathbf{P}^\pm \pm 2\gamma \kappa_{m_\pm} \mathbf{n}^\pm \,, \tag{5.16}$$

where γ is the surface tension constant coefficient.

5.3.1 Nondimensionalization

The thin sheet of fluid has an initially constant characteristic thickness h, and a characteristic length scale L, where L is the smallest lateral length scale (radius of curvature or characteristic wavelength of the applied load). We thus have

$$(x, y) = L(x^\star, y^\star) \,, z = h z^\star \,, \frac{h}{L} = \varepsilon \ll 1 \,. \tag{5.17}$$

Hence, equation (5.1) becomes

$$-\frac{1}{2} \ll z^\star \ll \frac{1}{2}\,.$$

The principal curvatures are proportional to the inverse of the radii of curvature, hence we scale them as

$$(\kappa_1, \kappa_2) = \frac{1}{L}\left(\kappa_1^\star, \kappa_2^\star\right)\,. \tag{5.18}$$

Thus, we have that

$$\varsigma_\beta^{\alpha\star} = \delta_\beta^\alpha\,,\ \ \varsigma_{\alpha\beta}{}^\star = a_{\alpha\beta}\,,\ \ \widehat{h}^\star = 1\,,\ \ N^{\alpha\beta} = n^{\alpha\beta}\,,\ \ M^{\alpha\beta} = m^{\alpha\beta}\,,\ \ \Lambda_\pm = 1\,. \tag{5.19}$$

It follows that the stress tensor, in equation (5.4), reduces to

$$\Upsilon^{ij} \equiv \sigma^{ij} = 2\eta\dot{\epsilon}_{ij} - p\delta_j^i\,. \tag{5.20}$$

Hence, from now on, we will use $\boldsymbol{\sigma}$ to denote the stress tensor throughout the thickness of the shell. Moreover, the stress tensor is symmetric, i.e., $\sigma^{\vartheta\beta} = \sigma^{\beta\vartheta}$, and $\sigma^{3\vartheta} = \sigma^{\vartheta 3}$.

Let us consider equation (5.5a), that, without the contribution of body forces $\mathbf{F_b}$ (such as the gravitational acceleration), reduces to

$$\sigma_{,\alpha}^{\alpha\beta} - b_\alpha^\beta \sigma^{\alpha 3} + \frac{1}{h}\frac{\partial\sigma^{3\beta}}{\partial z^\star} = 0\,. \tag{5.21}$$

Then, if $\partial\sigma^{3\beta}/\partial z^\star$ is of greater (or the same) order of magnitude as $\sigma^{\alpha 3}$, equation (5.21) reduces further to

$$\sigma^{\alpha\beta}_{,\alpha} + \sigma^{3\beta}_{,3} = 0 \,. \tag{5.22}$$

This in turns reduces the equations (5.8a) to

$$n^{\alpha\beta}_{,\alpha} + P^\beta = 0 \,, \tag{5.23}$$

where now $n^{\alpha\beta} = n^{\beta\alpha}$. Equation (5.8b) remains invariant, but we repeat it here for completeness sake

$$b_{\alpha\beta}n^{\alpha\beta} + q^\alpha_{,\alpha} + P^3 = 0 \,, \tag{5.24}$$

while equation (5.10) reduces to

$$m^{\alpha\beta}_{,\alpha} - q^\beta + \widetilde{P}^\beta = 0 \,, \tag{5.25}$$

where $\widetilde{P}^\beta = (h/2)P^\beta$. If $(h/2)P^\alpha_{,\alpha}$ is small compared with P^3, we can drop this term when we apply the same procedure outlined before, that is, to isolate the term q^β from equation (5.25) and substitute it into equation (5.24). Hence, equation (5.25) simplifies further to

$$m^{\alpha\beta}_{,\alpha} - q^\beta = 0 \,, \tag{5.26}$$

where now the bending moment stress $m^{\alpha\beta}$ is symmetric as well. And finally, equation (5.24) simplifies further to

$$m^{\alpha\beta}_{,\alpha\beta} + b_{\alpha\beta}n^{\alpha\beta} + P^3 = 0 \,. \tag{5.27}$$

Equations (5.23) and (5.27) provide the set of governing equation that we need to solve to describe the flow of the thin viscous sheet, coupled with the incompressibility condition.

5.4   Linearly Elastic Shells

In this section, we introduce the constitutive laws for linear elastic solids, commonly used in the field of linear elasticity to study the behavior of thin plates or shells undergoing stretching or bending deformations. We then outline the derivation of the Stokes-Rayleigh analogy that relates the constitutive equations of elastic solids and viscous fluids [113, 114]. By this correspondence, techniques used for the study of linear elastic solids can then be extended to the ones employed for creeping viscous flows.

Let us provide a general overview of a linear stress-strain relation, valid for all Hookean elastic media

$$\sigma_{ij} = 2G\epsilon_{ij} + K\epsilon_{kk}\delta_{ij}\,, \tag{5.28}$$

where $\epsilon_{kk} = Tr\epsilon$, with ϵ the strain tensor, K and G the two elastic parameters, which characterize the material's response to deformations: K, the bulk modulus, describes the medium response to (uniform) hydrostatic pressure; G, the shear modulus, represents the material's response to shear deformation. These two constants are related to the Young's modulus, Y, and the Poisson's ratio, ν, by the following relations

$$K = \frac{Y\nu}{(1+\nu)(1-2\nu)}\,, \qquad G = \frac{Y}{2(1+\nu)}\,. \tag{5.29}$$

As anticipated in Section 4.3, an incompressible, elastic solid corresponds to the limits $K/Y \to \infty$ and $\nu \to 1/2$. As these limits are approached, together with the assumption that only small deformations are considered, the product $-K\epsilon_{kk}$ tends to a finite value, the pressure p [115]. Hence, equation (5.28) reduces to

$$\sigma_{ij} = 2G\epsilon_{ij} - p\delta_{ij} \,. \tag{5.30}$$

We can see that the latter relation is identical to equation (5.20), provided the following transformations are applied

$$(Y, \nu) \leftrightarrow (3\eta, 1/2) \,, \quad (\mathbf{u}, \boldsymbol{\epsilon}, G) \leftrightarrow (\mathbf{v}, \dot{\boldsymbol{\epsilon}}, \eta) \,, \tag{5.31}$$

where we recall that the variable $\mathbf{u}$ indicates the vector displacement field and $\mathbf{v}$ the vector velocity field. We refer to the set of relations (5.31) as the Stokes-Rayleigh analogy relations.

Using equations (5.31), we can then rewrite equation (5.28) as

$$\sigma_{ij} = \frac{Y}{1+\nu} \left(\epsilon_{ij} + \frac{\nu}{1-2\nu} \epsilon_{kk} \delta_{ij} \right) \,. \tag{5.32}$$

We note that in equation (5.32), the limit $\nu \to 1/2$ represents the fact that the material requires an infinite amount of stress to change its volume, due to incompressibility. Following [112], we can invert the stress-strain relation (5.30) to write the strain in terms of the stress

$$\epsilon_{ik} = \frac{1+\nu}{Y} \sigma_{ik} - \frac{\nu}{Y} \sigma_{jj} \delta_{ik} \,. \tag{5.33}$$

For an elastic shell, subjected to both stretching and bending, the dimensional strain is given, in terms of the displacement vector $\mathbf{u} = u^\alpha \mathbf{a}_\alpha + u^3 \mathbf{a}_3$, by

$$\epsilon_{\alpha\beta} = \frac{1}{2}\left(u_\vartheta|_\alpha \mu_\beta^\vartheta + u_\vartheta|_\beta \mu_\alpha^\vartheta - 2(b_{\vartheta\alpha}\mu_\beta^\vartheta + b_{\vartheta\beta}\mu_\alpha^\vartheta)u_3\right) ,\tag{5.34a}$$

$$\epsilon_{\alpha 3} = \frac{1}{2}\left(\frac{\partial u_3}{\partial x_\alpha} + \frac{\partial u_\alpha}{\partial z} + b_\alpha^\vartheta u_\vartheta - z b_\alpha^\vartheta \frac{\partial u_\vartheta}{\partial z}\right) ,\tag{5.34b}$$

$$\epsilon_{33} = \frac{\partial u_3}{\partial z} .\tag{5.34c}$$

These can be nondimensionalized and used to rewrite the strain-stress relation in the context of thin shells

$$\epsilon_{\alpha\beta} = \frac{(1+\nu)}{Y}a_{\alpha\vartheta}a_{\beta\varsigma}\sigma^{\vartheta\varsigma} - \frac{\nu}{Y}a_{\alpha\beta}(a_{\vartheta\varsigma}\sigma^{\vartheta\varsigma} + \sigma^{33}),\tag{5.35}$$

$$\epsilon_{\alpha 3} = \frac{(1+\nu)}{Y}a_{\alpha\vartheta}\sigma^{\vartheta 3} ,\tag{5.36}$$

$$\epsilon_{33} = \frac{h}{Y}(\sigma^{33} - \nu a_{\alpha\vartheta}\sigma^{\alpha\vartheta}) ,\tag{5.37}$$

where

$$\epsilon_{\alpha\beta} = \frac{1}{2}\left(u_{\alpha,\beta} + u_{\beta,\alpha} - 2b_{\alpha\beta}u_3\right) .\tag{5.38}$$

Moreover, using equation (5.34b), we can simplify equation (5.38) based on the nondimensionalization, and obtain

$$\epsilon_{\alpha 3} = \frac{1}{2}\left(u_{3,\alpha} + \frac{1}{h}u_{\alpha,3} + b_\alpha^\vartheta\left(u_\alpha - z^\star u_{\vartheta,3}\right)\right) ,\tag{5.39}$$

so that if $u_{\vartheta,3}$ is of the same order of magnitude as u_ϑ, we have

$$\epsilon_{\alpha 3} = \frac{1}{2}\left(u_{3,\alpha} + u_{\alpha,3}\right) .\tag{5.40}$$

Based on the same scaling argument, we can omit the right-hand side of equation (5.34c) so that

$$u_{3,3} = 0 \Rightarrow u_3 = u_3(x,y), \tag{5.41}$$

hence, u_3 is a function of x and y. Following the same reasoning, we can assume that the normal and shear stresses $\sigma^{33}, \sigma^{\alpha 3}$ may be neglected in equation (5.34), so that

$$u_{\alpha,3} = -u_{3,\alpha} \tag{5.42}$$

and

$$u_\alpha = \widetilde{v}_\alpha - z u_{3,\alpha}, \tag{5.43}$$

where $\widetilde{v}_\alpha = \widetilde{v}_\alpha(x,y)$ is a function of x and y. Moreover, following [37], equation (5.38) reduces to

$$\epsilon_{\alpha\beta} = \frac{1}{2}\left(u_{\alpha,\beta} + u_{\beta,\alpha} - 2b_{\alpha\beta}u_3\right) - z u_{3,\alpha\beta}. \tag{5.44}$$

In equation (5.44) we see that the in-plane components of the strain tensor have an affine dependence on z. In fact, equation (5.44) states that the curvature of the midsurface, given by the term $u_{3,\alpha\beta}$, introduces a variation of the strain across the thickness. This is the fundamental kinematical relation for bending [112]. We will show in the following section how this variation will give an explicit form for the stretching and the bending energies of the sheet.

5.5   Energy-based Formulation

In this section, we outline an alternative formulation of the governing equations (5.23) and (5.27). Instead of finding directly the stress components, we find the energy potentials that an elastic shell possesses when deformed. For purely elastic problems, the resultant of all conservative forces, $\sum_i \mathbf{F}_i$, acting on the shell can be derived from the associated energy potentials. In contrast, when sheets of viscous fluid are considered, the internal (non-conservative) friction force between the fluid particles is generally not derivable from an energy potential. However, in this chapter we will focus on the creeping motion of sheets, for which the dissipation of energy is considered negligible. This simplification allows an easier computation of the viscous damping force. In addition, by considering the Stokes-Rayleigh analogy presented in Section 5.4, the computational advantage is evident when re-adapting solutions obtained for linear elastic shell problems. In the Computer Graphics literature [111, 117, 118, 119], this simplification has been used especially to achieve computationally advantageous and fast simulations of viscous materials.

We outline here the forms of the energy potentials due to the deformations of thin sheets of viscous fluids in motion. The dynamics of the sheets is due to surface tension and gravity effects. We consider the total free energy of the fluid, $E = E_{st} + E_G + E_{el}$, accounting for the contribution of the surface energy density, E_{st}, the gravitational potential, E_G, and the elastic energy density, E_{el}, which in turn, is constituted by the in-plane stretching energy E_s, and the bending energy E_b. One observation we make is that the surface tension γ may be interpreted both as free energy per unit area of the interface between two media and a force per unit length, as previously included in Chapters 2 and 3 (see, e.g., [94]). The form of the surface energy potential, given the contribution of both top and bottom surfaces of the boundary of the domain, is

$$E_{st} = \iint\limits_{\partial\Omega} 2\gamma dA \,, \tag{5.45}$$

where $dA = dx\,dy$.

To derive the other energy terms, consistently with [112], we study the work done by interior forces, when an elastic solid undergoes infinitesimal deformations. The displacement vector field has a small variation, from the value $u_i(\mathbf{x})$ to the value $(u_i(\mathbf{x}) + \delta u_i(\mathbf{x}))$. By definition, the work of the surface forces is

$$\delta W = \iint\limits_{\partial\Omega} \sigma_{ij} n_j \delta u_i dA \,, \tag{5.46}$$

with $dA = dx\,dy$. Using the divergence theorem, we turn the surface integral into a volumetric one

$$\delta W = \iiint\limits_{\Omega} \frac{\partial(\sigma_{ij}\delta u_i)}{\partial x_j}\, dV = \iiint\limits_{\Omega} \frac{\partial\sigma_{ij}}{\partial x_j}\delta u_i\, dV + \iiint\limits_{\Omega} \sigma_{ij}\frac{\partial(\delta u_i)}{\partial x_j}\, dV \,, \tag{5.47}$$

with $dV = dx\,dy\,dz$. We can rewrite the second term in the integral, using the symmetry of the stress tensor and the strain rate, and equation (5.47) becomes

$$\delta W = \iiint\limits_{\Omega} \frac{\partial\sigma_{ij}}{\partial x_j}\delta u_i\, dV + \iiint\limits_{\Omega} \sigma_{ij}\left[\frac{1}{2}\left(\frac{\partial(\delta u_i)}{\partial x_j} + \frac{\partial(\delta u_j)}{\partial x_i}\right)\right]\, dV \,. \tag{5.48}$$

We can see equation (5.48) as

$$\delta W = \delta E_G + \delta E_{el} \,, \tag{5.49}$$

where on the left hand side we have the work done by internal forces; on the right hand side the sum of the potential energy E_G associated with the external forces

(such as gravity) and of the elastic energy E_{el}. The latter is defined implicitly by its variation

$$\delta E_{el} = \iiint_\Omega \sigma_{ij} \delta \epsilon_{ij} \, dV \, . \tag{5.50}$$

Following [112], if we consider the case of a simple elastic spring, the variation of the elastic energy, for small perturbations of the configuration of the material, is given by

$$\delta E_{el} = \frac{1}{2} \iiint_\Omega ((\delta \sigma_{ij}) \epsilon_{ij} + \sigma_{ij} (\delta \epsilon_{il})) \, dV \, . \tag{5.51}$$

In equation (5.51), the constant $1/2$ represents the fact that when a spring is stretched, the average spring tension is half its final value at full load, because an operator has to work against the spring tension to bring it from its natural to its deformed state [112]. Moreover, we note that by linearity of the material, and by symmetry of the stress and strain tensors, we have that $(\delta \sigma_{ij}) \delta \epsilon_{ij} = \sigma_{ij} (\delta \epsilon_{il})$, and therefore the proposed energy density has the correct variation, given by equation (5.50). Hence, in the case of a linearly elastic material, we can write

$$E_{el} = \frac{1}{2} \iiint_\Omega \sigma_{ij} \epsilon_{ij} \, dV \, . \tag{5.52}$$

To derive the explicit form of E_{el}, we use the definitions of the stress tensor and the strains given for thin shells. In the previous section, due to scaling arguments, we neglected the components $\sigma^{33}, \sigma^{\alpha 3}$, that is, we imposed $\sigma^{33} = \sigma^{\alpha 3} = 0$. When we use this information in equation (5.32), we obtain the following conditions that the strain tensor must satisfy

$$\epsilon_{13} = 0, \quad \epsilon_{23} = 0, \tag{5.53a}$$

$$\epsilon_{33} = -\frac{\nu}{1-\nu}(\epsilon_{11} + \epsilon_{22}). \tag{5.53b}$$

When we plug equation (5.53) into the remaining components of equation (5.32), we find the constitutive relations for a plate, where the in-plane stress is related to the in-plane strain by

$$\sigma_{11} = \frac{Y}{1-\nu^2}(\epsilon_{11} + \nu\epsilon_{22}), \tag{5.54a}$$

$$\sigma_{22} = \frac{Y}{1-\nu^2}(\epsilon_{22} + \nu\epsilon_{11}), \tag{5.54b}$$

$$\sigma_{33} = \frac{Y}{1+\nu}\epsilon_{12}. \tag{5.54c}$$

We can now explicitly express the density of the elastic energy in equation (5.52) by expanding the sum in the integrand, and omitting the normal shear stress $\sigma_{\alpha3}$ and the transverse stress σ_{33}, as

$$e_{el} := \frac{\sigma_{\alpha\beta}\epsilon_{\alpha\beta}}{2} = \frac{\sigma_{11}\epsilon_{11} + \sigma_{22}\epsilon_{22} + 2\sigma_{12}\epsilon_{12}}{2}. \tag{5.55}$$

Using equation (5.54) into equation (5.55), we obtain

$$e_{el} = \frac{Y}{2(1-\nu^2)}\left[(\epsilon_{11} + \epsilon_{22})^2 - 2(1-\nu)(\epsilon_{11}\epsilon_{22} - \epsilon_{12}^2)\right]. \tag{5.56}$$

We note that, consistently with [111], equation (5.56) can be rearranged in a more compact form as

$$e_{el} = \frac{Y}{2(1-\nu^2)}\left[(1-\nu)Tr(\epsilon^2) + \nu(Tr\epsilon)^2\right]. \tag{5.57}$$

By using the inverse strain-stress relation (5.33) one could rewrite the elastic energy density as

$$e_{el} = \frac{1}{2Y} \left[(\sigma_{11} + \sigma_{22})^2 - 2(1 + \nu)(\sigma_{11}\sigma_{22} - \sigma_{12}^2) \right] . \tag{5.58}$$

To account for the energy throughout the whole thickness of the sheet, we integrate equation (5.57) with respect to z, from H^- to H^+, by using equation (5.44), and we find

$$\int_{H^-}^{H^+} e_{el}\, dz = \frac{Yh}{2(1 - \nu^2)} \left[(1 - \nu)Tr(\epsilon^2) + \nu(Tr\epsilon)^2 \right] +$$
$$\frac{Yh^3}{24(1 - \nu^2)} \left[(u_{3,xx} + u_{3,yy})^2 - 2(1 - \nu) \left(u_{3,xx} u_{3,yy} - (u_{3,xy})^2 \right) \right] . \tag{5.59}$$

Finally, by integrating equation (5.59) along the in-plane directions x and y, we finally find the elastic energy

$$E_{el} = E_s + E_b , \tag{5.60}$$

where we have defined the stretching and the bending energy terms as the ones that depend only on the in-plane or transversal deformations, respectively, given by

$$E_s = \frac{Yh}{2(1 - \nu^2)} \iint_{\partial\Omega} \left[(1 - \nu)Tr(\epsilon^2) + \nu(Tr\epsilon)^2 \right] dA , \tag{5.61}$$

$$E_b = \frac{Yh^3}{24(1 - \nu^2)} \iint_{\partial\Omega} \left[(u_{3,xx} + u_{3,yy})^2 - 2(1 - \nu) \left(u_{3,xx} u_{3,yy} - (u_{3,xy})^2 \right) \right] dA . \tag{5.62}$$

A discretization of the energy terms, given by equations (5.45), (5.61) and (5.62), can be found in Appendix C.

5.6 Extension of the Stokes-Rayleigh Analogy

Here, we propose a natural extension of the numerical simulations of thin viscous sheets presented in [111]. In the latter study, by the use of the Stokes-Rayleigh analogy (see Section 5.4), the energy terms (5.45), (5.61) and (5.62), were considered with strain rates, $\dot{\epsilon}$, in place of strains, ϵ, and used to find the dissipative forces in the equations of equilibrium for thin sheets of fluids. The model of elasticity was derived in [111] as a linear elastic (Hookean) solid, and viscosity was accounted for via the use of the Stokes-Rayleigh analogy, imposing the material parameter $Y = 3\eta$ (see equation (5.31)). We propose here to include viscoelastic effects by considering a different constitutive model, the Jeffreys model, that allows to capture different, interesting physical phenomena.

The differences between the constitutive model we aim to implement, and the one presented in [111], based on linear elasticity only, are remarkable. A linear Hookean model, oppositely to Maxwell and Jeffreys models, does not lead to the stress relaxation, and exhibits a reversible strain creep (this feature is typical for elastic solids, but it is not realistic for fluids). For completeness, we report here the constitutive model for viscoelastic fluids of Jeffreys type, equation (2.9), whose implementation we believe can constitute a useful expansion of the numerical study presented in [111]

$$\sigma + \lambda_1 \partial_t \sigma = 2\eta(\dot{\epsilon} + \lambda_2 \partial_t \dot{\epsilon}). \tag{5.63}$$

As stated in Chapter 2, we recall here that the total viscosity of the system for Jeffreys model is defined as $\eta = \eta_s + \eta_p$, where η_s and η_p are the viscosity coefficients of the Newtonian solvent and the polymeric solute, respectively.

As introduced in Section 5.4, the Stokes-Rayleigh analogy allows to find a bijective relation between the physical parameters proper of elastic solids and viscous

fluids. Through equation (5.31), we have observed that for incompressible media $\nu = 1/2$, and for viscous fluids $Y \leftrightarrow 3\eta$. We now propose to extend this analogy to bind the material parameters of elastic solids and viscoelastic fluids. Comparing the Jeffreys model, equation (5.63), with the constitutive law for Hookean solids, given by equation (5.30), and the viscous Newtonian fluids, equation (5.20), we find that

$$Y = \frac{\eta}{\lambda_1} \equiv \frac{(\eta_s + \eta_p)}{\lambda_1} \, . \tag{5.64}$$

For the Maxwell model, that is, in particular, recovered from the Jeffreys one when $\eta_s = 0 \Leftrightarrow \lambda_2 = 0$, we obtain

$$Y = \frac{\eta_p}{\lambda_1} \, . \tag{5.65}$$

We observe here that one could be tempted to use this analogy to define a stretching viscoelastic energy density, similar to the elastic one, given by equation (5.61). But we should emphasize that equation (5.61) was derived using the strain-stress relations, defined in equation (5.33). These relations describe the direct proportionality that exists between the strain and the stress tensor (and viceversa) for linearly elastic solids. However, the linear viscoelastic materials that we analyze in this dissertation obey differential laws (see equations (2.7) and (2.11)), and do not satisfy such direct proportionality. Hence, the energy-based formulation cannot be used to extend the study carried out by Batty et al. [111] to include viscoelastic effects through a similar viscoelastic stretching energy density. One could solve directly the equations governing the stresses, equations (5.23) and (5.27), and therefore obtain a formulation similar to the displacement-based formulation used in Chapter 4. Future work shall consider this different approach.
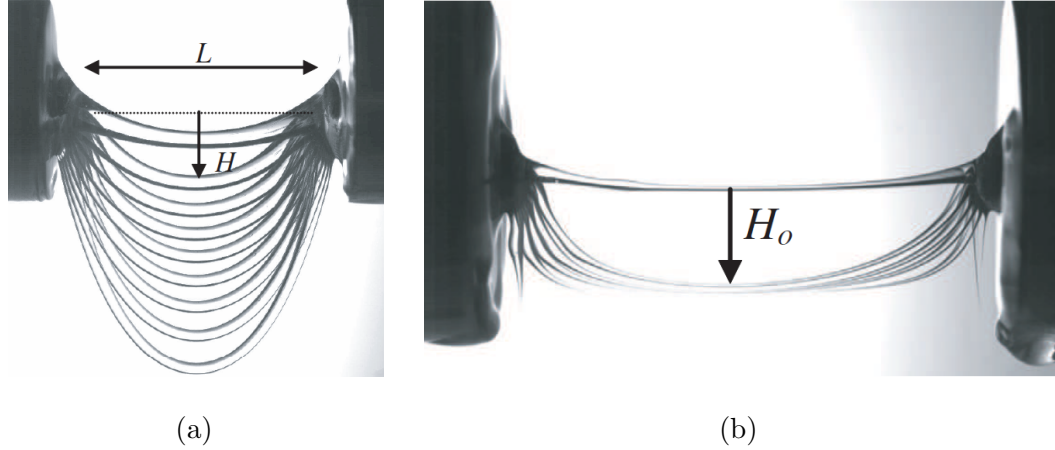
Figure 5.2 Experiments on a *viscous catenary*. In (a), the initial silicon thread of length equal to 25 mm and diameter equal to 1.75 mm. The filament collapses under its own weight and it is shown in snapshots taken every 0.08 s. In (b), the thinnest thread has reached a U-shape, with diameter of 0.33 mm.
Source: [121].

5.7 Applications and Future Work

The range of applications for the formalism presented is vast. In fact, three-dimensional simulations of thin viscoelastic sheets of fluids are used in several contexts: for instance, in biomedical sciences, there are many investigations in which body fluids (such as saliva, mucus, blood), cell migration, or stretched (muscular or tendinous) tissues are modeled as viscoelastic materials; also, in the food industry, numerical simulations of the motion of viscoelastic liquids such as custard, ice cream, starch suspensions, are considered for food processing and production. In this section, we show some applications that are not only interesting to study from the physical point of view, but also visually interesting for the Computer Graphics community. We present, in particular, two cases that have been implemented by Batty et al. [111], and that we consider as future work to be extended to include viscoelastic effects.

The first application we introduce is the *viscous catenary* problem [120, 121]. This physical phenomenon arises when a thin filament of viscous fluid is horizontally suspended, with its extremities attached to two rigid walls (see Figure 5.2). The

110
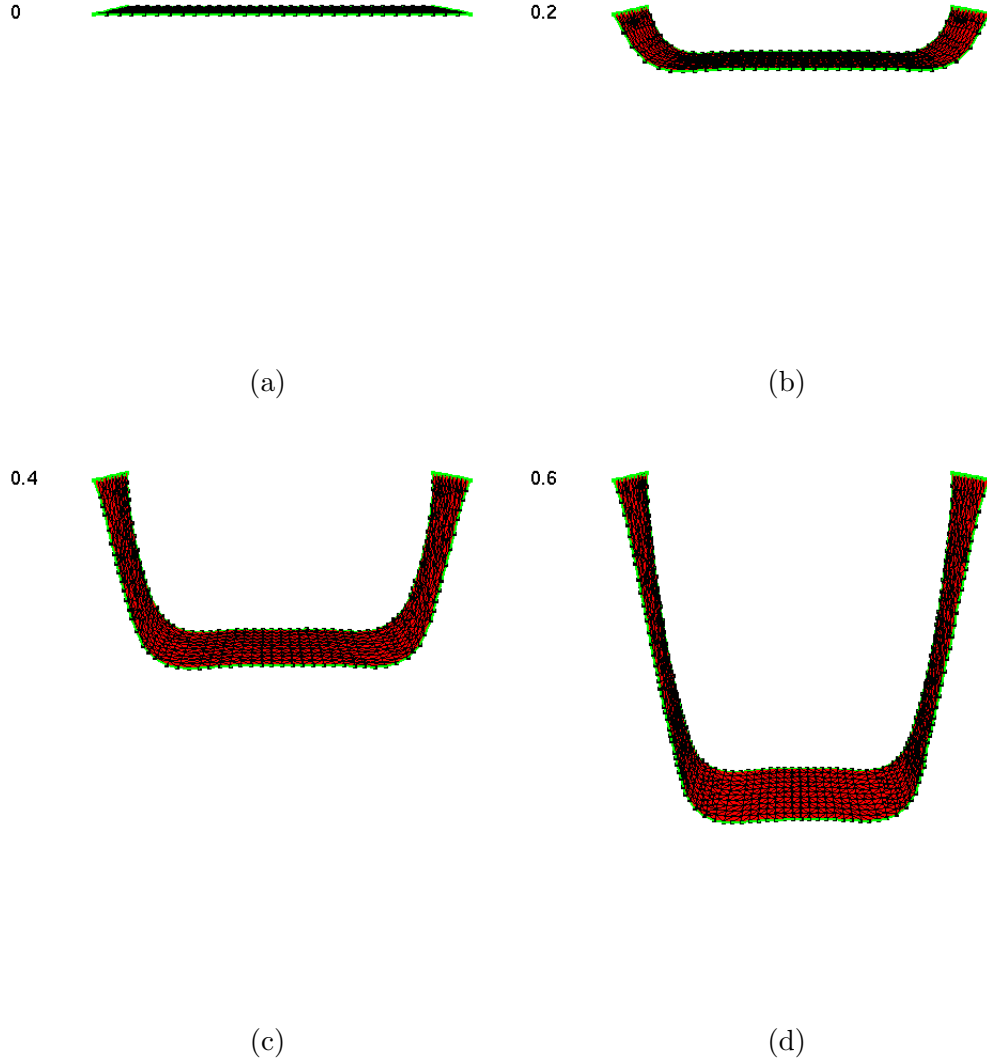
Figure 5.3 In (a) we show the initially flat configuration of a thin viscous sheet. In (b) $t = 0.2\,$s, (c) $t = 0.4\,$s, (d) $t = 0.6\,$s, we see the sheet of fluid gradually sagging, under the effects of gravity and surface tension.

filament collapses under its own weight and stretches along its longitudinal direction, gradually attaining a sagging configuration resembling a chain or a necklace (alias a *catenary*). This problem has also been analyzed, both theoretically and numerically [122, 123], in the context of viscoelastic filaments, giving rise to the phenomenon referred to as the *viscoelastic catenary*, by analogy. Future work should regard the implementation of the viscoelastic catenary problem and the comparison of the results to the ones presented in [111, 121, 122, 123]. As an illustration of the results obtained
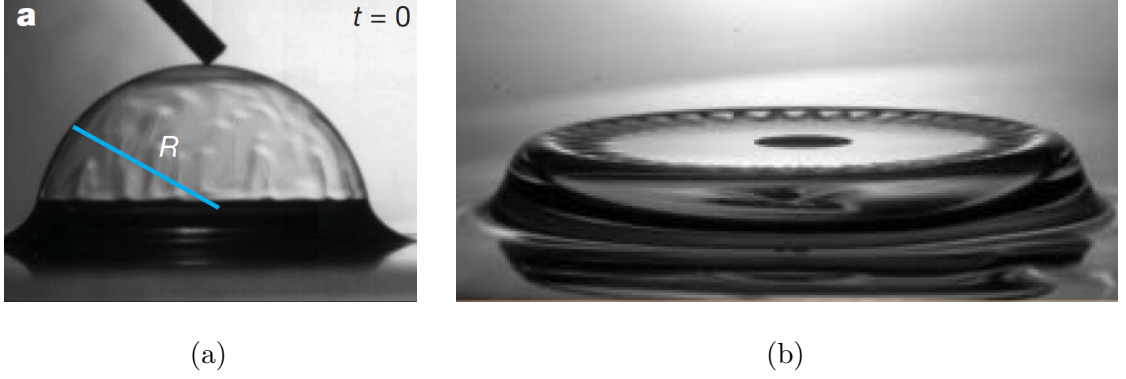
Figure 5.4 Experiments on a *viscous bubble*. In (a), the highly viscous cap before being punctured from the top. In (b), the cap, after being punctured and collapsed, shows wrinkling instabilities, known as "parachute instabilities".
Source: [127].

in [111], we plot four frames of the simulation of the viscous catenary. In Figure 5.3(a), we see the initially flat configuration of a thin sheet of viscous fluid. The material parameters employed are: horizontal and vertical lengths $L_x = 15\,\mathrm{mm}$ and $L_y = 5\,\mathrm{mm}$, respectively, initial thickness of the sheet $h = 1.75\,\mathrm{mm}$, density $\rho = 10^3\,\mathrm{kg/m^3}$, surface tension $\gamma = 20\,\mathrm{mN/m}$, and viscosity $\eta = 10\,\mathrm{Pa\ s}$. The elongational velocity is estimated by considering the depth at which the catenary has fallen over time, and for the simulation shown is $V \simeq 2.5\,\mathrm{cm/s}$. For this set of parameters the capillary number is $Ca = \eta V/\gamma = 12.5$, the Reynolds number $\rho V L_x/\eta = 0.03$, and the Bond number $B = \rho g L_x^2/\gamma = 112.5$. Thus viscosity dominates both surface tension and inertia, and the dynamics is mostly driven by gravity. In Figure 5.3(b), at time $t = 0.2\,\mathrm{s}$, we see that the sheet assumes a U-shape configuration. A similar shape has also been observed experimentally in [121], during the early times of a viscous catenary fall. In Figure 5.3(c), at time $t = 0.4\,\mathrm{s}$, and in Figure 5.3(d), at time $t = 0.6\,\mathrm{s}$, the sheet falls to a lower position preserving its general shape. As the sheet stretches along the in-plane directions, it preserves volume, hence possesses a non-uniform mass distribution (thicker at the local minimum) [121].

Another application that we consider is the collapse of a punctured *viscous bubble*, i.e., a thin cap-shaped viscous sheet enclosing an air bubble on a solid substrate. In this problem, the vapor bubble, collapses when the fluid interface is punctured (see Figure 5.4). Since the bubble interface is a very thin layer of fluid that separates the internal and the ambient gases, the study of such interfacial dynamics is suitable for thin film approximations. The cavitation dynamics for inviscid or viscous fluids has been subject of numerous analytical and experimental studies, see, e.g., [124, 125, 126]. More recently, an experimental study [127] has shown interesting interfacial features during the collapse phase of a viscous bubble, such as the wrinkle formation on the liquid-gas interface, referred to as "parachute instability". Other studies have expanded the cavitation dynamics analysis to viscoelastic bubbles, see, e.g., [128, 129, 130, 131].

Future investigations shall consider reproducing this problem in the context of discrete viscoelastic sheets, and comparing the results with the ones in [111, 127, 131]. As an example of the results obtained with the numerical framework developed by Batty et al. [111], we show the simulation of a punctured viscous bubble in Figure 5.5. The bubble is modeled as a hemispherical sheet laying on a solid substrate. The material parameters used for this numerical experiment are: horizontal length $L_x = 33\,\text{mm}$, and vertical length $L_y = 28\,\text{mm}$, initial thickness of the sheet $h = 1\,\mu\text{m}$, density $\rho = 10^3\,\text{kg/m}^3$, surface tension $\gamma = 50\,\text{mN/m}$, and viscosity $\eta = 10\,\text{Pa s}$. When inertial effects are negligible, i.e., for $Re \ll 1$, surface tension drives the collapse of the viscous film. For this regime of Reynolds number, the characteristic velocity of retraction is $V = R\gamma/h\eta$, where R is the radius of the cap [127]. Hence, the capillary number is $Ca = R/h = 5.25 \times 10^3$, and the Bond number is $B = \rho g R^2/\gamma = 5.5$. In Figure 5.5(a), we plot the initial configuration at time $t = 0\,\text{ms}$. The bubble is punctured, and in Figure 5.5(b), at time $t = 10\,\text{ms}$, we see that the collapse has started. In Figure 5.5(c), at time $t = 50\,\text{ms}$, we observe the hole expanding, and in Figure 5.5(d), at $t = 100\,\text{ms}$, the bubble interface has retracted significantly. As the

cap of fluid collapses, for this regime of capillary and Reynolds numbers, no daughter bubbles are formed, but radial and circular wrinkling appear [127]. The latter is due to the fluid interface retracting in rims, forming torii of air trapped between the fluid and the substrate, consistently with findings in [127]. The former one is less visible in our un-rendered images. The interested reader can refer to [111], where the radial wrinkles defining the parachute instability are more visible.

An overhauling and extension of the numerical framework by Batty et al. [111], will allow to analyze the physical behavior together with the morphology attained by the viscoelastic sheets and make direct comparisons with the experimental observations. For instance, falling viscoelastic catenaries have been observed to exhibit a viscous behavior in the early times, and an elastic behavior that slows down the sagging velocity for later times [122]. One could then analyze the elongational velocity to see if the numerical investigations can capture this behavior. For the case of the viscoelastic bubbles instead, one could simulate and analyze the viscoelastic effects that can also affect the parachute instability, that has been observed experimentally [127] and numerically [111] for viscous bubbles.

5.8   Conclusions

In summary, in this chapter, we provide a detailed derivation of the governing equations for thin viscous sheets. We present the implementation proposed by Batty et al. [111] that uses a discrete Lagrangian description, in which the finite element mesh deforms with the body. In this formulation, the stretching and bending energies are obtained through the shear stress and the bending moment that are present when linearly elastic shells are deformed, and the effects due to the surface tension are accounted for through the surface energy density. We then describe the Stokes-Rayleigh analogy that relates linear elastic and viscus constitutive models,

114
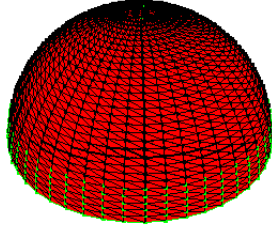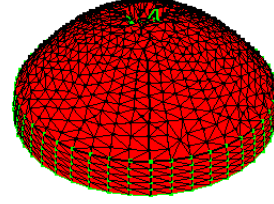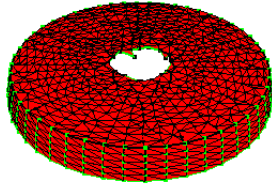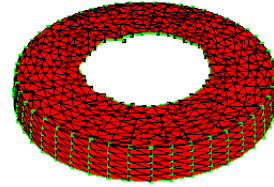
Figure 5.5 In (a), we show the initial hemispherical configuration of a thin viscous bubble laying on a solid substrate. The bubble is punctured at the azimuth and in (b), at time $t = 10$ ms, we see that it starts collapsing. In (c), at time $t = 50$ ms, the hole grows and in (d), at time $t = 100$ ms, the bubble interface retracts further.

and explain how this correspondence was employed in [111] to extend the energy formulations to represent stretching and bending deformations of thin viscous sheets.

We then propose our contribution to extend the formulation the Stokes-Rayleigh analogy to include linear viscoelastic constitutive models. However, we observe how this cannot be used to express an analogous form for the in-plane stretching energy, based on linear viscoelastic stresses of Maxwell or Jeffreys type (analyzed in this dissertation). Finally, we show two applications presented in [111]: the *viscous catenary* and the *viscous bubble*, leaving the implementation of their viscoelastic counterparts as future work.

CHAPTER 6

CONCLUSIONS AND FUTURE WORK

We have presented a novel numerical investigation of the dynamics of thin viscoelastic films in different settings. In the first part of this dissertation, we have analyzed the spontaneous dewetting/wetting processes of thin, incompressible viscoelastic films and drops, under the influence of the van der Waals interaction force and in the regime of weak slip with the substrate, in two spatial dimensions. For the case in which the gravitational body force is neglected, the equation that governs the interfacial dynamics of the thin films and drops was obtained within the lubrication theory, as a long-wave approximation of the Navier-Stokes equations, similar to the one reported in [13].

We have investigated the effects of viscoelasticity and the substrate slippage on the dynamics of thin viscoelastic films and the resulting length scales of instabilities. In the linear regime, our results are in agreement with the theoretical predictions given by the linear stability analysis. In the nonlinear regime, our simulations have revealed novel complex morphologies, in the form of satellite droplets, that depend on the viscoelasticity. We have investigated how the viscoelastic parameters and the slippage with the substrate affect the migration and coalescence of these secondary droplets. Moreover, we have analyzed the dynamic contact angle of viscoelastic drops that spontaneously spread or recede on a solid, prewetted substrate. Our simulations have suggested that viscoelasticity enhances the spreading and slows down the retraction of drops, by varying the smoothness of the interface in the contact line region, consistent with recent experimental [46] and computational [50] results. The analysis of the dynamic contact angle has also allowed us to verify the Cox-Voinov law for the viscous Newtonian case; while we show small deviations from this law for viscoelastic drops.

Furthermore, we have expanded our analysis of the interfacial flow of thin viscoelastic films, by adding the effects due to the gravitational force. We have derived a novel long-wave formulation of the governing equation for thin viscoelastic films of Jeffreys type, flowing down an inclined plane, and reported novel numerical simulations in the case of an inverted plane. The linear stability analysis, as in the case with absence of gravity, has showed that the viscoelastic parameters and the slippage coefficient do not influence either the wavenumber corresponding to the maximum growth rate or the critical one, but only influence the maximum growth rate. However, we have found that the length scales of instabilities are affected by the gravitational contribution. In the nonlinear regime, our results have showed that, at parity of viscoelastic and slippage parameters, gravity suppresses the satellite droplets that were found in absence of gravity, and reduces the width of the hole in the dewetted interface.

In the second part of this dissertation, we have investigated free-boundary flows of sheets of viscoelastic fluids, not necessarily deposited on a substrate, in three spatial dimensions. We have started by modeling the viscoelastic sheets as membranes, in which the in-plane stretching deformations are dominant with respect to transversal deflections, and in which bending stiffness is neglected. Subsequently, we have proposed the expansion of this formulation by modeling the viscoelastic sheets as shells, in which any application of loading or external forces causes both bending and stretching.

For the analysis of the dynamics of viscoelastic membranes, we have employed a displacement-based finite element formulation for nearly incompressible media. To describe the near incompressibility condition, we have introduced a penalty function, in which the penalty constant is proportional to the viscosity of the fluid. We have validated our implementation with several numerical experiments, demonstrating mesh-independence of our results, and validity of the formulation of

the near incompressibility. We have focused on two main applications of our general numerical framework for membranes: shear flow and extensional flow in drawing processes. Comparing the behavior of sheared Newtonian and Maxwellian membranes, we have observed the effects of viscoelasticity on the nature of the dynamics, as well as on their final configuration. We have found that Maxwellian membranes attain a deformation that is more pronounced, relative to their Newtonian counterpart, when they are continuously sheared. While they exhibit an elastic response, that is constitutively damped by viscosity, in the case of loading/unloading forcing. For the drawing process of Newtonian and Maxwellian membranes, with a constant or thermally-dependent viscosity, we have investigated how viscoelasticity affects the necking of the membranes in extensional flows. We have found that higher values of the relaxation time enhance the necking of the stretched membranes. For this reason, higher values of the relaxation time facilitate the onset of buckling and therefore the emergence of the wrinkling instabilities.

To further analyze the buckling behavior, the modeling of viscoelastic sheets as shells is considered. The analysis of the dynamics of viscoelastic shells has been proposed as an expansion of the formulation provided by Batty et al. for thin viscous sheets [111]. As the same formulation utilized by Batty et al., based on the variations of energy potentials, cannot be applied to the case of viscoelastic fluids that follow a differential constitutive model, future research directions shall consider the suggested formulation in which viscoelastic stresses are directly accounted for in the equations that govern the dynamics of thin viscoelastic shells.

APPENDIX A

FINITE ELEMENT DISCRETIZATION OF MEMBRANES

We outline here the details of the spatial discretization introduced in Chapter 4. We will describe here how each term in equation (4.2) is derived. By linear interpolation, we can specify a position in the triangular element by $\mathbf{X} = \xi_\alpha \widetilde{\mathbf{X}}^\alpha$ in the reference configuration, and $\mathbf{x} = \xi_\alpha \widetilde{\mathbf{x}}^\alpha$ in the current one. Where ξ_α represents the natural area coordinates, or barycentric coordinates [92], such that

$$\xi_1 + \xi_2 + \xi_3 = 1 \,. \tag{A.1}$$

Following [38], to describe the in-plane deformation and stresses of the membrane, it is convenient to introduce a surface coordinate system that lays on the plane of the triangle, denoted by Y_1 and Y_2, with normal direction N in the reference configuration, and y_1, y_2 with normal direction n in the current state (see Figure A.1, repeated here for the reader's convenience).

In the surface coordinate system, the origin of the coordinates, $(Y_1 O Y_2)$ and $(y_1 o y_2)$ are placed at the nodal locations, $\widetilde{X}^1$ and $\widetilde{x}^1$, respectively. The unit base vectors then may be constructed from the linear displacement triangle, constituted by the three vertices labeled by $(1, 2, 3)$, by aligning the first base vector along the 1-2 side. For simplicity, we denote the edge vectors of the reference configuration by $\mathbf{E}_{12} = \widetilde{\mathbf{X}}^2 - \widetilde{\mathbf{X}}^1$, $\mathbf{E}_{13} = \widetilde{\mathbf{X}}^3 - \widetilde{\mathbf{X}}^1$, $\mathbf{E}_{23} = \widetilde{\mathbf{X}}^3 - \widetilde{\mathbf{X}}^2$, and $\mathbf{e}_{12} = \widetilde{\mathbf{x}}^2 - \widetilde{\mathbf{x}}^1$, $\mathbf{e}_{13} = \widetilde{\mathbf{x}}^3 - \widetilde{\mathbf{x}}^1$, and $\mathbf{e}_{23} = \widetilde{\mathbf{x}}^3 - \widetilde{\mathbf{x}}^2$ for the current configuration. Hence, we define the first unit base vector as

$$\hat{\mathbf{e}}_1 = \frac{\mathbf{e}_{12}}{\|\mathbf{e}_{12}\|} \,. \tag{A.2}$$

A vector normal to the plane of the triangle is found by $\mathbf{E}_3 = \mathbf{E}_{12} \times \mathbf{E}_{13}$ in the reference state, and $\mathbf{e}_3 = \mathbf{e}_{12} \times \mathbf{e}_{13}$ in the current state. The normal vector in the current state
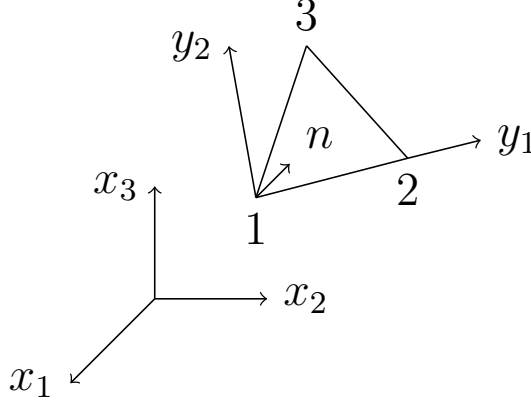
Figure A.1 The surface coordinate system on a triangular element in the deformed configuration.

is normalized by

$$\mathbf{n} := \hat{\mathbf{e}}_3 = \frac{\mathbf{e}_3}{\|\mathbf{e}_3\|}, \tag{A.3}$$

and similarly for the reference state, $\mathbf{N} := \widehat{\mathbf{E}}_3 = \mathbf{E}_3/\|\mathbf{E}_3\|$. The second base vector is found by $\mathbf{E}_2 = \mathbf{N} \times \mathbf{E}_1$, and analogously by $\mathbf{e}_2 = \mathbf{n} \times \mathbf{e}_1$ for the current configuration. Their normalized unit vectors are found, similarly, as $\widehat{\mathbf{E}}_2 = \mathbf{N} \times \widehat{\mathbf{E}}_1$, and $\hat{\mathbf{e}}_2 = \mathbf{n} \times \hat{\mathbf{e}}_1$.

With the base vectors defined above for the plane of the triangle, we can define positions directly as

$$y^i = (\mathbf{x} - \widetilde{\mathbf{x}}^1) \cdot \hat{\mathbf{e}}_i . \tag{A.4}$$

From equation (A.4), we note that for $\widetilde{\mathbf{y}}^1$, the expression is $\widetilde{y}^1 = (\widetilde{\mathbf{x}}^1 - \widetilde{\mathbf{x}}^1) \cdot \hat{\mathbf{e}}_i = 0$. Hence, any position $\mathbf{y}$, found by interpolation of the surface coordinates reduces to

$$\mathbf{y} = \xi_\alpha \widetilde{\mathbf{y}}^\alpha = \xi_2 \widetilde{\mathbf{y}}^2 + \xi_3 \widetilde{\mathbf{y}}^3 , \tag{A.5}$$

where we have used the summation convention, and equation (A.1) becomes redundant.

We define the deformation gradient tensor as

$$\mathbf{F} = \frac{\partial \mathbf{y}}{\partial \mathbf{Y}} = \mathbf{I} + \frac{\partial \mathbf{u}}{\partial \mathbf{Y}}, \tag{A.6}$$

Moreover, we can write

$$\mathbf{F}\frac{\partial \mathbf{Y}}{\partial \boldsymbol{\xi}} = \frac{\partial \mathbf{y}}{\partial \mathbf{Y}}\frac{\partial \mathbf{Y}}{\partial \boldsymbol{\xi}} = \frac{\partial \mathbf{y}}{\partial \boldsymbol{\xi}}. \tag{A.7}$$

If we denote by $\mathbf{J}$ the Jacobian transformation tensor for the reference state, and by $\mathbf{j}$ the Jacobian transformation tensor for the current state, we have

$$\mathbf{J} = \frac{\partial \mathbf{Y}}{\partial \boldsymbol{\xi}}, \qquad \mathbf{j} = \frac{\partial \mathbf{y}}{\partial \boldsymbol{\xi}}. \tag{A.8}$$

Hence, we can express the deformation gradient as

$$\mathbf{F} = \mathbf{j}\mathbf{G}, \tag{A.9}$$

where we have used $\mathbf{G} = \mathbf{J}^{-1}$. Following closely the derivation by Taylor et al. in [38], we can expand the expressions for the matrices $\mathbf{J}$ and $\mathbf{j}$, by taking into consideration that $\mathbf{E}_{12}$ is orthogonal to the unit vector $\widehat{\mathbf{E}}_1$, and analogously $\mathbf{e}_{12}$ is orthogonal to the unit vector $\hat{\mathbf{e}}_1$, they become

$$\mathbf{J} = \begin{bmatrix} \|\mathbf{E}_{12}\| & \mathbf{E}_{12}^T \mathbf{E}_{13}/\|\mathbf{E}_{12}\| \\ 0 & \widehat{\mathbf{E}}_3/\|\mathbf{E}_{12}\| \end{bmatrix}, \tag{A.10}$$

and

$$\mathbf{j} = \begin{bmatrix} \|\mathbf{e}_{12}\| & \mathbf{e}_{12}^T \mathbf{e}_{13}/\|\mathbf{e}_{12}\| \\ 0 & \widehat{\mathbf{e}}_3/\|\mathbf{e}_{12}\| \end{bmatrix}. \tag{A.11}$$

We note that the symmetric part of the displacement gradient is defined as $H_{ij} = \partial u_i/\partial x_j$, and can be recast as

$$\mathbf{H} = \mathbf{F} - \mathbf{I}. \tag{A.12}$$

Thus,

$$\boldsymbol{\epsilon} = \frac{1}{2}\left(\mathbf{H} + \mathbf{H}^T\right). \tag{A.13}$$

We can then define

$$\mathbf{C} = \mathbf{F}^T\mathbf{F} = \mathbf{J}^{-T}\mathbf{j}^T\mathbf{j}\mathbf{J}^{-1} = \mathbf{G}^T\mathbf{g}\mathbf{G}, \tag{A.14}$$

where we have used $\mathbf{g} = \mathbf{j}^T\mathbf{j}$. We rewrite equation (A.14) in component form as

$$C_{IJ} = G_{iI}g_{ij}G_{jJ}, \quad \text{with } i,j = 1,2, \text{ and } I,J = 1,2, \tag{A.15}$$

where the components of the matrix $\mathbf{G}$ are

$$G_{11} = \frac{1}{J_{11}}, G_{22} = \frac{1}{J_{22}}, G_{12} = \frac{-J_{12}}{J_{11}J_{22}}, G_{21} = 0. \tag{A.16}$$

We can now find the relations among the indices needed for the term $\delta\boldsymbol{\epsilon}^T\boldsymbol{\sigma}$ in equation (4.2), first by noting that

$$\delta C_{IJ}\sigma_{IJ} = G_{iI}\delta g_{ij}G_{jJ}\sigma_{IJ} = \delta g_{ij}s_{ij}, \tag{A.17}$$

where the variable s_{ij}, related to stress, is defined by

$$s_{ij} = G_{iI}G_{jJ}\sigma_{IJ}. \tag{A.18}$$

We can rewrite the last transformation in matrix form

$$s_{ij} = \mathbf{Q}^T\boldsymbol{\sigma}, \tag{A.19}$$

where $\mathbf{Q}$ is a matrix of the change of index, defined by

$$\mathbf{Q} = \begin{bmatrix} G_{11}^2 & 0 & 0 \\ G_{12}^2 & G_{22}^2 & G_{12}G_{22} \\ 2G_{11}G_{12} & 0 & G_{11}G_{22} \end{bmatrix}. \tag{A.20}$$

We can use equation (A.17) and write the second term on the right-hand side of equation (4.2), as

$$\int_{\Omega^{(e)}} \delta\boldsymbol{\epsilon}^T \boldsymbol{\sigma} h\, d\, A = \int_{\Omega^{(e)}} \frac{h}{2} \delta C_{IJ} \sigma_{IJ} d\, A = \frac{h}{2} \delta g_{ij} s_{ij} A^{(e)}, \qquad (A.21)$$

where the area of a triangular element in the reference configuration, $A^{(e)}$, can be calculated given any two vectors on the reference configuration triangle, e.g., $\mathbf{E}_{12}$, and $\mathbf{E}_{13}$, by $A^{(e)} = \|\mathbf{E}_{12} \times \mathbf{E}_{13}\|/2$. It is convenient to rewrite equation (A.21) in matrix form

$$\frac{1}{2}\delta C_{IJ}S_{IJ} = [\delta\epsilon_{11} \;\; \delta\epsilon_{22} \;\; 2\delta\epsilon_{12}] \begin{bmatrix} \sigma_{11} \\ \sigma_{22} \\ \sigma_{12} \end{bmatrix} = \delta\boldsymbol{\epsilon}^T \boldsymbol{\sigma}, \qquad (A.22)$$

or, in terms of the expression found in equation (A.21)

$$\frac{1}{2}\delta g_{ij}s_{ij} = [\delta g_{11} \;\; \delta g_{22} \;\; 2\delta g_{12}] \begin{bmatrix} s_{11} \\ s_{22} \\ s_{12} \end{bmatrix} = \frac{1}{2}\delta\boldsymbol{g}^T \boldsymbol{s}. \qquad (A.23)$$

We can finally write

$$\delta\boldsymbol{\epsilon} = \frac{1}{2}\delta\mathbf{C} = \mathbf{Q}\mathbf{b}\delta\tilde{\mathbf{x}}, \qquad (A.24)$$

where the vector $\tilde{\mathbf{x}}$ represents the three nodal values stacked in a (9×1) column vector, and $\mathbf{b}$ is the strain-displacement matrix, given by

$$\mathbf{b} = \begin{bmatrix} -\mathbf{e}_{12}^T & \mathbf{e}_{12}^T & \mathbf{0} \\ -\mathbf{e}_{13}^T & \mathbf{0} & \mathbf{e}_{13}^T \\ -(\mathbf{e}_{12}+\mathbf{e}_{13})^T & \mathbf{e}_{13}^T & \mathbf{e}_{12}^T \end{bmatrix}. \qquad (A.25)$$

Finally, we can form the divergence operator matrix, for each element, $\mathbf{B}^{(e)}$, in equation (4.2), in terms of variations of the displacement for each element, as

$$\mathbf{B}^{(e)} = \mathbf{Q}\mathbf{b}\,. \tag{A.26}$$

We next need to define the matrix $\mathbf{M}^{(e)}$, in equation (4.2), representing the mass matrix for each element, whose components are given by

$$\mathbf{M}^{(e)}_{\alpha\beta} = \int_{\Omega^{(e)}} \rho h \xi_\alpha \xi_\beta d\,A\,\mathbf{I}\,. \tag{A.27}$$

The last vector used in equation (4.2), $\widetilde{\mathbf{F}}_\mathbf{b}$, represents the constant nodal body force, such as gravity, that is trivially linearly interpolated at the nodes, and its description is omitted here.

APPENDIX B

GEOMETRIC MODELING OF SHELLS

We present here the classic notation used in thin shell theory [37, 39], useful for the description of the dynamics of thin liquid sheets, described in Chapter 5. We consider a system of curvilinear coordinates (not necessarily orthogonal), expressed as (x_α, x_β), that sits on the sheet midsurface. Hence, we can express any position vector as $\mathbf{x}(x, y, z, t) = \mathbf{x}_0(x, y, t) + z\widehat{\mathbf{a}}_3(x, y, t)$, where $\widehat{\mathbf{a}}_3$ is the normal unit vector defined by

$$\widehat{\mathbf{a}}_3 = \frac{\widehat{\mathbf{a}}_\alpha \times \widehat{\mathbf{a}}_\beta}{|\widehat{\mathbf{a}}_\alpha \times \widehat{\mathbf{a}}_\beta|} \,, \tag{B.1}$$

where $\widehat{\mathbf{a}}_\alpha, \widehat{\mathbf{a}}_\beta$, are the in-plane covariant basis vectors (that may not be orthogonal or unitary), defined by $\widehat{\mathbf{a}}_\alpha = \mathbf{x}_{0,\alpha}$ (where we recall that $,_\alpha$ indicates by convention $\partial/\partial_{x_\alpha}$). The contravariant basis vectors $\widehat{\mathbf{a}}^\alpha$ are the reciprocal of the covariant ones and satisfy

$$\widehat{\mathbf{a}}^\alpha \cdot \widehat{\mathbf{a}}_\beta = \delta^\alpha_\beta \,, \tag{B.2}$$

where δ^α_β is the Kronecker delta. The quantities $a_{\alpha\beta} = \widehat{\mathbf{a}}_\alpha \cdot \widehat{\mathbf{a}}_\beta$ and $a^{\alpha\beta} = \widehat{\mathbf{a}}^\alpha \cdot \widehat{\mathbf{a}}^\beta$ are the covariant and contravariant components of the (symmetric) metric tensor (whose components are also called first fundamental form) of the midsurface. The covariant components of the second fundamental tensor of the midsurface are

$$b_{\alpha\beta} = -\widehat{\mathbf{a}}_\alpha \cdot \widehat{\mathbf{a}}_{3,\beta} \equiv -\widehat{\mathbf{a}}_\beta \cdot \widehat{\mathbf{a}}_{3,\alpha} \,, \tag{B.3}$$

Equation (B.3) gives the definition of the components of the curvature tensor $\kappa_{\alpha\beta}$ as follows

$$\kappa_{\alpha\beta} = a^{\alpha\vartheta}b_{\beta\vartheta} \equiv a_{\alpha\vartheta}b^{\beta\vartheta}\,, \tag{B.4}$$

where we have used the summation convention for repeated indices. The invariant quantities defined in term of these components are: the mean curvature $\kappa_m := (1/2)b_\alpha^\alpha = (1/2)Tr\kappa$, and the Gaussian curvature $\mathcal{G} := |\kappa_{\alpha\beta}| = b_1^1 b_2^2 - b_2^1 b_1^2$. We note that in this notation, the superscript corresponds to the row index of a tensor, the subscript to the column one. The values $\kappa_1 := b_1^1$ and $\kappa_2 := b_2^2$ are the principal curvatures of the midsurface, i.e., the perpendicular directions with respect to which the midsurface is not twisted. Now we can define the rate of change of the curvature tensor $\dot{\kappa}_{\alpha\beta}$ as

$$\frac{\partial \kappa_{\alpha\beta}}{\partial t} := \dot{\kappa}_{\alpha\beta} = w_{|\alpha\beta} - \kappa_{\alpha\vartheta}\kappa_{\vartheta\beta}w + \kappa_{\alpha\vartheta}u_{\vartheta|\beta} + \kappa_{\beta\vartheta}u_{\vartheta|\alpha} + \kappa_{\beta\vartheta|\alpha}u_\vartheta\,, \tag{B.5}$$

where the notation $u_{|\alpha}$ expresses the covariant derivative of the component u of the vector $\mathbf{u}$ with respect to the midsurface coordinate x_α. This is an important concept in differential geometry: the covariant derivative of a tensor component is just the corresponding component of the partial derivative of the tensor itself, accounting for the variation of the basis vectors from one point to another, i.e., for the change in metric of a surface [39]. For a vector $\mathbf{u}$ (i.e., tensor of rank one) they are defined by

$$u_{\alpha|\beta} = u_{\alpha,\beta} - \Gamma_{\alpha\beta}^\vartheta u_\vartheta\,, \tag{B.6}$$

where $\Gamma_{ij\vartheta} = (a_{i\vartheta,j} + a_{j\vartheta,i} - a_{ij,\vartheta})/2$ and $\Gamma_{ij}^\vartheta = \Gamma_{ij\vartheta}\widehat{\mathbf{a}}^\vartheta$ are the Christoffel symbols of first and second kind, respectively. The covariant derivative of a tensor of rank greater than one can be found in [37]. Another important notion is the one of covariant base

vectors $\mathbf{g}_i$, and the contravariant base vectors $\mathbf{g}^i$ at an arbitrary point in the sheet, given by

$$\mathbf{g}_\alpha = \mathbf{x}_{0,\alpha} = \varsigma_\alpha^\lambda \widehat{\mathbf{a}}_\lambda, \quad \mathbf{g}^\alpha = \widehat{h}^{-1}(\varsigma_\vartheta^\vartheta \delta_\lambda^\alpha - \varsigma_\lambda^\alpha)\widehat{\mathbf{a}}^\lambda, \quad \mathbf{g}_3 = \mathbf{g}^3 = \widehat{\mathbf{a}}_3 , \tag{B.7}$$

where

$$\varsigma_\alpha^\beta = \delta_\alpha^\beta - z b_\alpha^\beta , \tag{B.8}$$

and

$$\widehat{h} = 1 - 2\kappa_m z + \mathcal{G} z^2 . \tag{B.9}$$

The quantity defined in (B.9) is a surface invariant that represents the ratio of an element of surface area at a distance z from the midsurface to the corresponding area on the midsurface itself [39]. The covariant and contravariant components of the metric tensor at an arbitrary point in the sheet are $g_{ij} = \mathbf{g}_i \cdot \mathbf{g}_j$ and $g^{ij} = \mathbf{g}^i \cdot \mathbf{g}^j$.

To describe the boundary conditions, we need to define a set of basis vectors that are tangential and normal to the boundary surfaces, respectively, $H^\pm$

$$t^\pm = \mathbf{x}_0 \pm \frac{h}{2}\widehat{\mathbf{a}}_3 \tag{B.10}$$

where here and in the following discussion a subscript or superscript containing $\pm$ indicates that the quantity is evaluated at $H^\pm$, respectively. The covariant and contravariant tangent vectors to the outer surfaces are $\mathbf{c}_\alpha^\pm = \pm\mathbf{x}_{,\alpha}^\pm = \pm\mathbf{g}_\alpha^\pm + (h/2)_{,\alpha}\mathbf{g}_3$, and $c_\pm^\alpha = \pm\mathbf{g}_\pm^\alpha + g^{\alpha\vartheta}h_{,\vartheta}(\mathbf{g}^3 \mp (h/2)_{,\beta}\mathbf{g}_\pm^\beta)/(2\Lambda_\pm^2)$, respectively, where

$$\Lambda_\pm = (1 + (1/4)g_\pm^{\alpha\beta}h_{,\alpha}h_{,\beta})^{1/2} \, . \tag{B.11}$$

The outward (with respect to each boundary surface $H^\pm$) unit normal vectors $\mathbf{c}_3^\pm \equiv \mathbf{c}_3^\pm := \mathbf{n}^\pm$ are

$$\mathbf{n}^\pm = \frac{\mathbf{c}_1^\pm \times \mathbf{c}_2^\pm}{|\mathbf{c}_1^\pm \times \mathbf{c}_2^\pm|} = n_i^\pm \mathbf{g}_\pm^i \, , \tag{B.12}$$

or component-wise

$$(n_\alpha^\pm, n_3^\pm) = \Lambda_\pm^{-1}(-h_{,\alpha}/2, \pm 1) \, . \tag{B.13}$$

For small deflections, the mean curvatures of the outer surfaces are $\kappa_{m_\pm} = \kappa_m \pm ((b_\beta^\alpha b_\alpha^\beta)h + a^{\alpha\beta}h|_{\alpha\beta})/4$.

APPENDIX C

FINITE ELEMENT DISCRETIZATION OF SHELLS

In this appendix, we report the numerical discretization of the energy terms presented in Section 5.5, closely following the framework provided in [111]. We approximate the domain Ω with a mesh constituted by a set of finite triangular elements. The sheet thickness $h(x, y, t)$ is approximated by a piecewise constant function over each triangle, and a triangle's volume is assumed to be constant, given by $V_T = hA_T$, where A_T is the area of the triangle T. Hence, the total surface area is given by the sum of all triangles areas $A = \sum_T A_T$. The discrete version of (5.45) is then

$$E_{st} = \sum_T 2\gamma A_T = 2\gamma A \,. \tag{C.1}$$

The force due to surface tension is then given by $\mathbf{F}_{st} = -\nabla E_{st}$. Since γ is assumed to be constant, this reduces to $\mathbf{F}_{st} = -2\gamma \nabla A$. To calculate ∇A, let us first define the area A of a triangle given the vectors of its three vertices $\mathbf{a}, \mathbf{b}, \mathbf{c}$ as

$$A = \frac{1}{2} \left\| (\mathbf{b} - \mathbf{a}) \times (\mathbf{c} - \mathbf{a}) \right\| \,. \tag{C.2}$$

Following the supplemental material of [111], this can be recast using the Levi-Civita symbol

$$\widehat{\varepsilon_{ijk}} = \begin{cases} 1 & , \text{ if } (i, j, k) \text{ is a cyclic permutation of } (1, 2, 3) \\ -1 & , \text{ if } (i, j, k) \text{ is an acyclic permutation of } (1, 2, 3) \\ 0 & , \text{ otherwise }, \end{cases} \tag{C.3}$$

$$A = \frac{1}{2}\sqrt{\widehat{\varepsilon_{ijk}}(b_j - a_j)(c_k - a_k)\widehat{\varepsilon_{imn}}(b_m - a_m)(c_n - a_n)}$$

$$= \frac{1}{2}\sqrt{(b_j - a_j)(c_k - a_k)(b_j - a_j)(c_k - a_k) - (b_j - a_j)(c_k - a_k)(b_k - a_k)(c_j - a_j)}$$

$$= \frac{1}{2}\sqrt{K}, \tag{C.4}$$

where

$$K = (b_j - a_j)(c_k - a_k)(b_j - a_j)(c_k - a_k) - (b_j - a_j)(c_k - a_k)(b_k - a_k)(c_j - a_j) \tag{C.5}$$

We then need to compute ∇A with directional derivatives with respect to the triangle vertex positions. Considering a generic vertex $\mathbf{X}$, by chain rule we have

$$\frac{\partial A}{\partial X_i} = \frac{1}{4\sqrt{K}}\frac{\partial K}{\partial X_i} \tag{C.6}$$

Let us show each component of the directional derivatives

$$\frac{\partial K}{\partial c_i} = 2(c_i - a_i)(b_j - a_j)(b_j - a_j) - 2(b_i - a_i)(b_j - a_j)(b_j - a_j), \tag{C.7}$$

or in vector form

$$\frac{\partial K}{\partial \mathbf{c}} = 2(||\mathbf{b} - \mathbf{a}||(\mathbf{c} - \mathbf{a}) - ((\mathbf{c} - \mathbf{a}) \cdot (\mathbf{b} - \mathbf{a}))(\mathbf{b} - \mathbf{a})), \tag{C.8}$$

analogously,

$$\frac{\partial K}{\partial \mathbf{b}} = 2(||\mathbf{c} - \mathbf{a}||(\mathbf{b} - \mathbf{a}) - ((\mathbf{b} - \mathbf{a}) \cdot (\mathbf{c} - \mathbf{a}))(\mathbf{c} - \mathbf{a})), \tag{C.9}$$
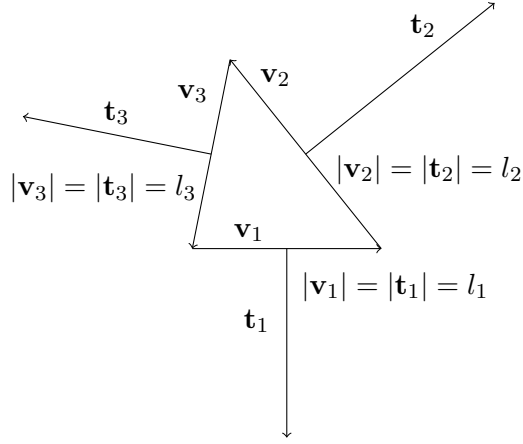
Figure C.1 A reference triangle with vertices vectors $\mathbf{v}_i$, labeled in clockwise order.

while

$$\frac{\partial K}{\partial \mathbf{a_i}} = -\left(\frac{\partial K}{\partial b_i} + \frac{\partial K}{\partial c_i}\right). \tag{C.10}$$

Next we define the strain, following the description in [132], where a relation between the strain and the deformation of the edges of a triangle is given. In the context of a finite element discretization, it is in fact useful to describe the strain in terms of the deformation that each element undergoes. We make use of the notation in Figure (C.1) where we show a reference triangle with edge vectors $\mathbf{v}_i$, whose lengths are l_i in undeformed state and $\tilde{l}_i$ in deformed configuration. The vectors denoted by $\mathbf{t}_i$ are perpendicular to the corresponding edge vectors $\mathbf{v}_i$, and have the same lengths $|\mathbf{v}_i| = |\mathbf{t}_i| = l_i$. By definition, the strain for a single triangle, ϵ_T, satisfies

$$s_i = \frac{1}{2}(\tilde{l}_i^2 - l_i^2) = \mathbf{v}_i^T \epsilon_T \mathbf{v}_i. \tag{C.11}$$

Since ϵ_T is a symmetric tensor, we can express it as a linear combination of a tensor basis $\epsilon_T = \sum_i \zeta_i \mathbf{t}_i \otimes \mathbf{t}_i$, where the coefficients of the linear combination are given by $\zeta_i = (s_j + s_k - s_i)/8A_T^2$. So that

132

$$\epsilon_T = -\frac{1}{8A_T^2}\sum_i (s_j + s_k - s_i)(\mathbf{t}_i \otimes \mathbf{t}_i). \qquad (C.12)$$

Since the vertices vectors $\mathbf{v}_i$ constitute a closed triangle, so do the vectors $\mathbf{t}_i$. This translates to the expressions $\mathbf{v}_i + \mathbf{v}_j + \mathbf{v}_k = 0$ and $\mathbf{t}_i + \mathbf{t}_j + \mathbf{t}_k = 0$. Taking this information into account, we can expand equation (C.12) into

$$\epsilon_T = -\frac{1}{16A_T^2}\sum_{i=1}^{3}(\tilde{l}_i^2 - l_i^2)(\mathbf{t}_j \otimes \mathbf{t}_k + \mathbf{t}_k \otimes \mathbf{t}_j). \qquad (C.13)$$

We can now write the discrete version of equation (5.61)

$$E_s = \frac{1}{2}\sum_T A_T \frac{Yh_T}{(1-\nu^2)}\left((1-\nu)Tr((\epsilon_T)^2) + \nu(Tr\epsilon_T)^2\right), \qquad (C.14)$$

where the terms $(Tr\epsilon_T)^2$ and $Tr((\epsilon_T)^2)$ are discretized as follows

$$(Tr\epsilon_T)^2 = \frac{1}{16A_T^4}\sum_{i,l} s_i s_l(\mathbf{t}_j \cdot \mathbf{t}_k)(\mathbf{t}_m \cdot \mathbf{t}_n), \qquad (C.15)$$

$$Tr((\epsilon_T)^2) = \frac{1}{32A_T^4}\sum_{i,l} s_i s_l\left((\mathbf{t}_k \cdot \mathbf{t}_m)(\mathbf{t}_j \cdot \mathbf{t}_n) + (\mathbf{t}_k \cdot \mathbf{t}_n)(\mathbf{t}_j \cdot \mathbf{t}_m)\right). \qquad (C.16)$$

Finally, the discrete version of the bending energy term (5.62) is, summed over all edges e, given by

$$E_b = \sum_e \frac{Yh_e^3}{12(1-\nu^2)}(\phi_e - \widetilde{\phi}_e)\widetilde{l}_e/\widetilde{l}_e^*, \qquad (C.17)$$

where ϕ_e is the angle between two adjacent triangles, and h_e is the mean thickness of the two adjacent triangles. If we denote with A_a the total area of two incident triangles, then $\widetilde{l}_e^* = A_a/(3\widetilde{l}_e)$ is the length of the barycentric dual edge [111].

To calculate the effects due to the viscous dissipative force over each triangle T by considering the Stokes-Rayleigh analogy, we need to consider the time derivative of the strain tensor, in place of the strain tensor. We numerically discretize the time domain $[0, t]$ as $[t_0, n\Delta t]$, where $n = 0, 1, \dots$ indicates the number of time steps, and Δt is the temporal step size. Hence, we denote with ϵ^n, the strain at the time step n, and with ϵ^{n+1}, the strain at the time step $n + 1$.

Once we have discretized all energy terms, we can find the corresponding discrete forces at the time step $n+1$ (using an implicit formulation), i.e., $\sum_i \mathbf{F}_i^{n+1} = -\nabla(E_{st} + E_s + E_b)^{n+1}$. Next, we discretize Newton's law of motion, with a backward Euler approximation, i.e., $\sum_i \mathbf{F}_i^{n+1} = \rho(\mathbf{u}^{n+1} - \mathbf{u}^n)/\Delta t$ (for the case in which the inertial term is retained for transient analyses). Hence, we can solve for the unknown simplicial velocity $\mathbf{u}^{n+1}$, with which each vertex of the mesh moves to the next position. We then update the reference configuration with the new (deformed) configuration found, and repeat the iteration for the time integration. We outline here the algorithm described in the reference work [111]:

1. At each time step, the reference configuration of finite elements is initialized to the current configuration state (an initial condition of which is provided according to the physical problem investigated).

2. All discrete forces are calculated with respect to this reference configuration.

3. Backward Euler integration is performed to find the velocity of each vertex of the discrete mesh.

4. New position of vertices are found using the old position in the reference configuration and their velocity.

5. *El Topo* library [133] is used to perform collision-processing calculations and find a safe end-of-step configuration.

6. Each triangle's thickness is adjusted to reflect conservation of mass.

7. Proximity checks are performed, and in case topology changes are needed, remeshing is performed to improve triangles aspect ratios.

REFERENCES

[1] A. Oron, S. Davis, and G. Bankoff. Long-scale evolution of thin liquid films. *Rev. Mod. Phys.*, 69:931–980, 1997.

[2] T. G. Myers. Thin films with high surface tension. *SIAM Rev.*, 3:441–462, 1998.

[3] A. Sharma. Many paths to dewetting of thin films: anatomy and physiology of surface instability. *Eur. Phys. J. E*, 12:397–408, 2004.

[4] P.-G. de Gennes. Wetting: statics and dynamics. *Rev. Mod. Phys.*, 57:827–863, 1985.

[5] R. Scardovelli and S. Zaleski. Direct numerical simulation of free-surface and interfacial flow. *Annu. Rev. Fluid Mech.*, 31:567–603, 1999.

[6] G. Tryggvason, R. Scardovelli, and S. Zaleski. *Direct numerical simulations of gas-liquid multiphase flows.* Cambridge, U. K., Cambridge University Press, 2011.

[7] S. A. Chester. A constitutive model for coupled fluid permeation and large viscoelastic deformation in polymeric gels. *Soft Matter*, 8:8223–8233, 2012.

[8] P. Yue, J. J. Feng, C. Liu, and J. Shen. A diffuse-interface method for simulating two-phase flows of complex fluids. *J. Fluid Mech.*, 515:293–317, 2004.

[9] J. C. Maxwell. On the dynamical theory of gases. *Phil. Trans. R. Soc. Lond.*, 157:49–88, 1867.

[10] H. Jeffreys. *The Earth: its origin, history, and physical constitution.* Cambridge, U. K., Cambridge University Press, 1952.

[11] R. A. Bird, R. C. Armstrong, and O. Hassager. *Dynamics of polymeric liquids: volume 1 fluid mechanics.* Toronto, Canada, Wiley-Interscience, 1987.

[12] O. Reynolds. On the theory of lubrication and its application to Mr. Beauchamp tower's experiments, including an experimental determination of the viscosity of olive oil. *Philos. Trans. R. Soc. London*, 177:157–234, 1886.

[13] M. Rauscher, A. Münch, B. Wagner, and R. Blossey. A thin-film equation for viscoelastic liquids of Jeffreys type. *Eur. Phys. J. E*, 17:373–379, 2005.

[14] F. Brochard-Wyart, G. Debregeas, R. Fondecave, and P. Martin. Dewetting of supported viscoelastic polymer films: birth of rims. *Macromolecules*, 30:1211–1213, 1997.

[15] M. Renardy. *Mathematical analysis of viscoelastic flows.* Society for Industrial and Applied Mathematics, 2000.

[16] S. A. Safran and J. Klein. Surface instability of viscoelastic thin films. *J. Phys. II*, 3:749–757, 1993.

[17] G. Reiter. Dewetting of thin polymer films. *Phys. Rev. Lett.*, 68:75–80, 1992.

[18] J. Sarkar and A. Sharma. A unified theory of instabilities in viscoelastic thin films: from wetting to confined films, from viscous to elastic films, and from short to long waves. *Langmuir*, 26:8464–8473, 2010.

[19] P. F. Green and V. Ganesan. Dewetting of polymeric films: unresolved issues. *Eur. Phys. J. E*, 12:449–454, 2003.

[20] S. Gabriele, P. Damman, S. Sclavons, S. Desperez, S. Coppée, G. Reiter, M. Hamieh, S. Al Akhrass, T. Vilmin, and E. Raphael. Viscoelastic dewetting of constrained polymer thin film. *J. Polymer Sci.: Part B: Polymer Phys.*, 44:3022–3030, 2006.

[21] A. Sharma and G. Reiter. Instability of thin polymer films on coated substrates: rupture, dewetting, and drop formation. *J. Colloid Interface Sci.*, 178:383–399, 1995.

[22] S. Herminghaus, R. Seemann, and K. Jacobs. Generic morphologies of viscoelastic dewetting fronts. *Phys. Rev. Lett.*, 89:056101, 2002.

[23] S. Herminghaus, K. Jacobs, and R. Seemann. Viscoelastic dynamics of polymer thin films and surfaces. *Eur. Phys. J. E*, 12:101–110, 2003.

[24] P.-G. de Gennes. *Scaling concepts in polymer physics*. New York, New York, U. S. A., Cornell University Press, 1979.

[25] R. M. Christensen. *Theory of viscoelasticity. An introduction*. New York, New York, U. S. A., Academic Press, 1982.

[26] S. Gabriele, S. Sclavons, G. Reiter, and P. Damman. Disentanglement time of polymers determines the onset of rim instabilities in dewetting. *Phys. Rev. Lett.*, 96:156105, 2006.

[27] E. S. Shaqfeh. Purely elastic instabilities in viscometric flows. *Annu. Rev. Fluid Mech.*, 28:129–185, 1996.

[28] L. Wu and S. Y. Chou. Electrohydrodynamic instability of a thin film of viscoelastic polymer underneath a lithographically manufactured mask. *J. Non-Newton. Fluid Mech.*, 125:91–99, 2005.

[29] D. Izbassarov and M. Muradoglu. A front-tracking method for computational modeling of viscoelastic two-phase flow systems. *J. Non-Newton. Fluid Mech.*, 223:122–140, 2015.

[30] V. Barra, S. Afkhami, and L. Kondic. Interfacial dynamics of thin viscoelastic films and drops. *J. Non-Newton. Fluid Mech.*, 237:26–38, 2016.

136

[31] T. Vilmin and E. Raphaël. Dewetting of thin polymer films. *Eur. Phys. J. E*, 21:161–174, 2006.

[32] G. Tomar, V. Shankar, S. K. Shukla, A. Sharma, and G. Biswas. Instability and dynamics of thin viscoelastic liquid films. *Eur. Phys. J. E*, 20:185–199, 2006.

[33] A. J. Levine and F. C. MacKintosh. Dynamics of viscoelastic membranes. *Phys. Rev. E*, 66:061606, 2002.

[34] E. A. Evans and M. Hochmuth. Membrane viscoleasticity. *Biophys. J.*, 16:1–11, 1976.

[35] V. A. Lubarda and A. Marzani. Viscoelastic response of thin membranes with application to red blood cells. *Acta Mech.*, 202:1–16, 2009.

[36] W. D. Jr. Callister. *Materials science and engineering.* New York, New York, U. S. A., John Wiley & Sons, Inc., 2007.

[37] A. E. Green and W. Zerna. *Theoretical elasticity.* New York, New York, U. S. A., Dover Publications Inc., 1968.

[38] R. L. Taylor, E. Oñate, and P.-A. Ubach. *Finite element analysis of membrane structures*, pages 47–68. Springer Netherlands, Dordrecht, 2005.

[39] N. M. Ribe. A general theory for the dynamics of thin viscous sheets. *J. Fluid Mech.*, 457:255–283, 2002.

[40] P. D. Howell. Models for thin viscous sheets. *Eur. J. Appl. Math.*, 7:321–343, 1996.

[41] R. Blossey, A. Münch, M. Rauscher, and B. Wagner. Slip vs. viscoelasticity in dewetting thin films. *Eur. Phys. J. E*, 20:267–271, 2006.

[42] P.-G. de Gennes, F. Brochard-Wyart, and D. Quéré. *Capillarity and wetting phenomena — drops, bubbles, pearls, waves.* New York, New York, U. S. A., Springer-Verlag, 2004.

[43] K. Mahady, S. Afkhami, J. Diez, and L. Kondic. Comparison of Navier-Stokes simulations with long-wave theory: Study of wetting and dewetting. *Phys. Fluids*, 25:112103, 2013.

[44] J.-H. Kim, H. P. Kavehpour, and J. P. Rothstein. Dynamic contact angle measurements on superhydrophobic surfaces. *Phys. Fluids*, 27:032107, 2015.

[45] J.-H. Kim and J. P. Rothstein. Dynamic contact angle measurements of viscoelastic fluids. *J. Non-Newton. Fluid Mech.*, 225:54–61, 2015.

[46] Y. Wei, E. Rame, L. M. Walker, and S. Garoff. Dynamic wetting with viscous Newtonian and non-Newtonian fluids. *J. Phys.: Condens. Matter*, 21:464126, 2009.

[47] Y. Wei, G. K. Seevaratnam, S. Garoff, E. Ramé, and L. M. Walker. Dynamic wetting of Boger fluids. *J. Colloid Interface Sci.*, 313:274–280, 2007.

[48] D. Bartolo, A. Boudaoud, G. Narcy, and D. Bonn. Dynamics of non-Newtonian droplets. *Phys. Rev. Lett.*, 99:174502, 2007.

[49] P. Yue and J. J. Feng. Phase-field simulations of dynamic wetting of viscoelastic fluids. *J. Non-Newton. Fluid Mech.*, 189-190:8–13, 2012.

[50] Y. Wang, D. Q. Minh, and G. Amberg. Dynamic wetting of viscoelastic droplets. *Phys. Rev. E*, 92:043002, 2015.

[51] D. Izbassarov and M. Muradoglu. Effects of viscoelasticity on drop impact and spreading on a solid surface. *Phys. Rev. Fluids*, 1:023302, 2016.

[52] R. G. Cox. The dynamics of the spreading of liquids on a solid surface. Part 1. Viscous flow. *J. Fluid Mech.*, 168:169–194, 1986.

[53] O. V. Voinov. Hydrodynamics of wetting. *Fluid Dyn.*, 11:714–721, 1976.

[54] J. Israelachvili. *Intermolecular & surface forces.* London, U. K., Academic Press, 1985.

[55] F. Mainardi and G. Spada. Creep, relaxation and viscosity properties for basic fractional models in rheology. *Eur. Phys. J. Spec. Topics*, 193:133–160, 2011.

[56] D. A. Siginer. *Stability of non-linear constitutive formulations for viscoelastic fluids.* New York, New Yok, U. S. A., Springer, 2014.

[57] R. Fetzer, K. Jacobs, A. Münch, B. Wagner, and T. P. Witelski. New slip regimes and the shape of dewetting thin liquid films. *Phys. Rev. Lett.*, 95:127801, 2005.

[58] A. Münch, B. Wagner, and T. P. Witelski. Lubrication models with small to large slip lengths. *J. Eng. Math.*, 53:359–383, 2005.

[59] J. Hao and T.-W. Pan. Simulation for high Weissenberg number: Viscoelastic flow by a finite element method. *Appl. Math. Lett.*, 20:988–993, 2007.

[60] G. Teletzke, H. T. Davis, and L. E. Scriven. How liquids spread on solids. *Chem. Eng. Commun.*, 55:41–82, 1987.

[61] J. A. Diez and L. Kondic. On the breakup of fluid films of finite and infinite extent. *Phys. Fluids*, 19:072107, 2007.

[62] I. Seric, S. Afkhami, and L. Kondic. Interfacial instability of thin ferrofluid films under a magnetic field. *J. Fluid Mech.*, 755:1–12, 2014.

[63] K. Mahady, S. Afkhami, and L. Kondic. A volume of fluid method for simulating fluid/fluid interfaces in contact with solid boundaries. *J. Comput. Phys.*, 294:243–257, 2015.

[64] J. W. Thomas. *Numerical partial differential equations.* New York, New York, U. S. A., Springer, 1995.

[65] L. Kondic. Instabilities in gravity driven flow of thin fluid films. *SIAM Rev.*, 45:95–115, 2003.

[66] J. A. Diez and L. Kondic. Computing three-dimensional thin film flows including contact lines. *J. Comput. Phys.*, 183:274–306, 2002.

[67] A. L. Bertozzi. The mathematics of moving contact lines in thin liquid films. *Not. Amer. Math. Soc.*, 45:689–697, 1998.

[68] T.-S. Lin and L. Kondic. Thin films flowing down inverted substrates: Two dimensional flow. *Phys. Fluids*, 22:052105, 2010.

[69] R. G. Larson. *The structure and rheology of complex fluids*. Oxford, U. K., Oxford University Press, 1999.

[70] H.-C. Chang, E. A. Demekhin, and E. Kalaidin. Iterated stretching of viscoelastic jets. *Phys. Fluids*, 11:1717–1737, 1999.

[71] J. Li and M. A. Fontelos. Drop dynamics on the beads-on-string structure for viscoelastic jets: A numerical study. *Phys. Fluids*, 15:922–937, 2003.

[72] M. A. Spaid and G. M. Homsy. Viscoelastic free surface flows: spin coating and dynamic contact lines. *J. Non-Newton. Fluid Mech.*, 55:249–281, 1994.

[73] M. A. Spaid and G. M. Homsy. Stability of Newtonian and viscoelastic dynamic contact lines. *Phys. Fluids*, 8:460–478, 1996.

[74] R. Seemann, S. Herminghaus, and K. Jacobs. Shape of a liquid front upon dewetting. *Phys. Rev. Lett.*, 87:196101, 2001.

[75] D.-Y. Hsieh. Stability of a conducting fluid flowing down an inclined plane in a magnetic field. *Phys. Fluids*, 8:1785–1791, 1965.

[76] L. W. Schwartz. Viscous flows down an inclined plane: Instability and finger formation. *Phys. Fluids A: Fluid*, 1:443–445, 1989.

[77] R. E. Kelly, D. A. Goussis, S. P. Lin, and F. K. Hsu. The mechanism for surface wave instability in film flow down an inclined plane. *Phys. Fluids A: Fluid*, 1:819–828, 1989.

[78] D.-Y. Hsieh. Mechanism for instability of fluid flow down an inclined plane. *Phys. Fluids A: Fluid*, 2:1145–1148, 1990.

[79] M. A. Lam, L. J. Cummings, T.-S. Lin, and L. Kondic. Modeling flow of nematic liquid crystal down an incline. *J. Eng. Math.*, 94:97–113, 2015.

[80] M. S. Tshehla. The flow of a variable viscosity fluid down an inclined plane with a free surface. *Math. Probl. Eng.*, 2013:1–8, 2013.

[81] D. Picchi, P. Poesio, A. Ullmann, and N. Brauner. Characteristics of stratified flows of newtonian/non-Newtonian shear-thinning fluids. *Int. J. Multiphas. Flow*, 97:109–133, 2017.

[82] J. R. De Bruyn. Growth of fingers at a driven three-phase contact line. *Phys. Review A*, 46:R4500–4503, 1992.

[83] A. E. H. Love. *A treatise on the mathematical theory of elasticity.* New York, New York, U. S. A., Dover Publications, 1944.

[84] L. D. Landau and E. M. Lifshitz. *Theory of elasticity.* Oxford, U. K., Pergamon Press, 1970.

[85] E. Ventsel and T. Krauthammer. *Thin plates and shells.* New York, New York, U. S. A., Marcel Dekker, 2001.

[86] J. Bonet, R. D. Wood, J. Mahaney, and P. Heywood. Finite element analysis of air supported membrane structures. *Comput. Methods Appl. M. E.*, 190:579–595, 2000.

[87] W. K. Chua and M. L. Oyen. Viscoelastic properties of membranes measured by spherical indentation. *Cel. Mol. Bioeng.*, 2:4956, 2009.

[88] C. W. Harland, M. J. Bradley, and R. Parthasarathy. Phospholipid bilayers are viscoelastic. *P. Natl. Acad. Sci. USA*, 107:1914619150, 2010.

[89] G. E. Crawford and J. C. Earnshaw. Viscoelastic relaxation of bilayer lipid membranes. frequency-dependent tension and membrane viscosity. *Biophys. J.*, 52:87–94, 1987.

[90] D. O'Kiely, C. J. W. Breward, I. M. Griffiths, P. D. Howell, and U. Lange. Edge behaviour in the glass sheet redraw process. *J. Fluid Mech.*, 785:248–269, 2015.

[91] M. Taroni, C. J. W. Breward, L. J. Cummings, and I. M. Griffiths. Asymptotic solutions of glass temperature profiles during steady optical fibre drawing. *J. Eng. Math.*, 80:1–20, 2013.

[92] O. C. Zienkiewicz, R. L. Taylor, and J. Z. Zhu. *The finite element method: its basis and fundamentals.* Oxford, U. K., Elsevier, 2013.

[93] D. Palaniappan. On some general solutions of transient stokes and brinkman equations. *J. Theor. Appl. Mech.*, 52:405–415, 2014.

[94] G. K. Batchelor. *An introduction to fluid dynamics.* Cambridge, U. K., Cambridge University Press, 1967.

[95] T. J. R. Hughes. *The finite element method: linear static and dynamic finite element analysis.* New York, New York, U. S. A., Dover Publications Inc., 2000.

[96] J. Van der Zanden, G. D. C. Kuiken, A. Segal, W. J. Lindhout, and M. A. Hulsen. Numerical experiments and theoretical analysis of the flow of an elastic liquid of the upper-convected maxwell type in the presence of geometrical discontinuities. *Appl. Sci. Res.*, 42:303–318, 1985.

[97] R. Courant. Variational methods for the solution of problems of equilibrium and vibrations. *Bull. Amer. Math. Soc.*, 49:1–23, 1943.

[98] J. Shen. On error estimates of the penalty method for unsteady Navier-Stokes equations. *SIAM J. Numer. Anal.*, 32:386403, 1995.

[99] O. C. Zienkiewicz and R. L. Taylor. *The finite element method*, volume 2. Oxford, U. K., Butterworth-heinemann, 2000.

[100] P. Hansbo, M. G. Larson, and F. Larsson. Tangential differential calculus and the finite element modeling of a large deformation elastic membrane problem. *Comp. Mech.*, 56:87–95, 2015.

[101] P. Howell, G. Kozyreff, and J. Ockendon. *Applied Solid Mechanics*. Cambridge, U. K., Cambridge University Press, 2008.

[102] H. M. Hilber, T. J. R. Hughes, and R. L. Taylor. Improved numerical dissipation for time integration algorithms in structural dynamics. *Earthq. Eng. Struct. D.*, 5:283–292, 1977.

[103] U. Brink and E. Stein. On some mixed finite element methods for incompressible and nearly incompressible finite elasticity. *Comp. Mech.*, 19:105–119, 1996.

[104] J. C. Simo and F. Armero. Geometrically non-linear enhanced strain mixed methods and the method of incompatible modes. *Int. J. Numer. Meth. Eng.*, 33:1413–1449, 1992.

[105] X. Lu, P. Lin, and J.-G. Liu. Analysis of a sequential regularization method for the unsteady navier-stokes equations. *Math. Comput.*, 77:1467–1494, 2008.

[106] S. Srinivasan, Z. Wei, and L. Mahadevan. Wrinkling instability of an inhomogeneously stretched viscous sheet. *Phys. Rev. Fluids*, 2:074103, 2017.

[107] G. Pfingstag, B. Audoly, and A. Boudaoud. Thin viscous sheets with inhomogeneous viscosity. *Phys. Fluids*, 23:063103, 2011.

[108] E. Cerda and L. Mahadevan. Geometry and physics of wrinkling. *Phys. Rev. Lett.*, 90:074302, 2003.

[109] J. D. Buckmaster, A. Nachman, and L. Ting. The buckling and stretching of a viscida. *J. Fluid Mech.*, 69:1–20, 1975.

[110] L. Euler. *Methodus inveniendi lineas curvas maximi minimive proprietate gaudentes, sive solutio problematis isoperimetrici lattissimo sensu accepti. Caput additamentum 1*, volume E065. eulerarchive.maa.org (accessed on April 24, 2018), 1744.

[111] C. Batty, A. Uribe, B. Audoly, and E. Grinspun. Discrete viscous sheets. *ACM Trans. Graph.*, 31:113:1–7, 2012.

[112] B. Audoly and Y. Pomeau. *Elasticity and geometry: From hair curls to the nonlinear response of shells.* Oxford, U. K., Oxford University Press, 2010.

[113] G. G. Stokes. On the theories of the internal friction of fluids in motion and of the equilibrium and motion of elastic solids. *Trans. Camb. Phil. Soc.*, 8:287–347, 1845.

[114] J. W. S. Rayleigh. *The theory of sound.* London, U. K., Macmillan, 1894.

[115] D. Bercovici. *Mantle Dynamics.* Amsterdam, Netherlands, Elsevier, 2009.

[116] N. M. Ribe. Bending and stretching of thin viscous sheets. *J. Fluid Mech.*, 433:135–160, 2001.

[117] D. Baraff and A. Witkin. Large steps in cloth simulation. In *Proc. 25th Ann. Conf. Comput. Graph. Inter. Tech.*, SIGGRAPH '98, pages 43–54, 1998.

[118] L. Kharevych, Weiwei Yang, Y. Tong, E. Kanso, J. E. Marsden, P. Schröder, and M. Desbrun. Geometric, variational integrators for computer animation. In *Proc. 2006 ACM SIGGRAPH/Eurograph. Symp. Comput. Animat.*, SCA '06, pages 43–51, 2006.

[119] M. Bergou, B. Audoly, E. Vouga, M. Wardetzky, and E. Grinspun. Discrete viscous threads. *ACM Trans. Graph.*, 29:116:1–10, 2010.

[120] J. Teichman and L. Mahadevan. The viscous catenary. *J. Fluid Mech.*, 478:71–80, 2003.

[121] M. Le Merrer, J. Seiwert, D. Quéré, and C. Clanet. Shapes of hanging viscous filaments. *EPL (Europhys. Lett.)*, 84:56004, 2008.

[122] A. Roy, L. Mahadevan, and J.-L. Thiffeault. Fall and rise of a viscoelastic filament. *J. Fluid Mech.*, 563:283–292, 2006.

[123] K. Kamrin and L. Mahadevan. Soft catenaries. *J. Fluid Mech.*, 691:165–177, 2012.

[124] D. V. Georgievskii. Cavitation bubble collapse in nonlinear viscous and viscoplastic media. *Fluid Dyn.*, 29:299–302, 1994.

[125] L. Trilling. The collapse and rebound of a gas bubble. *J. Appl. Phys.*, 23:14–17, 1952.

[126] V. A. Bogoyavlenskiy. Differential criterion of a bubble collapse in viscous liquids. *Phys. Rev. E*, 60:504–508, 1999.

[127] J. C. Bird, R. de Ruiter, L. Courbin, and H. A. Stone. Daughter bubble cascades produced by folding of ruptured thin films. *Nature*, 465:759–762, 2010.

[128] A. C. Papanastasiou, L. E. Scriven, and C. W. Macosko. Bubble growth and collapse in viscoelastic liquids analyzed. *J. Non-Newton. Fluid Mech.*, 16:53–75, 1984.

[129] I. Tanasawa and W. J. Yang. Dynamic behavior of a gas bubble in viscoelastic liquids. *J. Appl. Phys.*, 41:4526–4531, 1970.

[130] S. J. Lind and T. N. Phillips. Spherical bubble collapse in viscoelastic fluids. *J. Non-Newton. Fluid Mech.*, 165:56–64, 2010.

[131] H. S. Fogler and J. D. Goddard. Collapse of spherical cavities in viscoelastic fluids. *Phys. Fluids*, 13:1135–1141, 1970.

[132] Y. Gingold, A. Secord, J. Han, Y. Grinspun, and D. Zorin. A discrete model for inelastic deformation of thin shells. In *Tech. rep.*, pages 1–12, 2004.

[133] T. Brochu and R. Bridson. Robust topological operations for dynamic explicit surfaces. *SIAM J. Sci. Comput.*, 31:2472–2493, 2009.